Performance Evaluation of High-Strength Steel Pipelines for High-Pressure Gaseous Hydrogen Transportation

CRES Project No. CRES-2009-J02-01

Final Report Prepared for

U.S. Department of Transportation
Pipeline and Hazardous Materials Safety Administration
Office of Pipeline Safety
DOT Project BAA DTHP56-07-0001

Prepared by

Yaoshan Chen, Ming Liu and Yong-Yi Wang
Center for Reliable Energy Systems

CRES

Andrew J. Slifka, Elizabeth Drexler, Robert Amaro, and David McColskey
National Institute of Standards and Technology

NIST

Louis Hayden
American Society of Mechanical Engineers

Performance Evaluation of High-Strength Steel Pipelines for High-Pressure Gaseous Hydrogen Transportation

Executive Summary

Pipeline steels suffer significant degradation of their mechanical properties in high-pressure gaseous hydrogen, including their fatigue cracking resistances to cyclic loading. The current project work was conducted to produce fatigue crack growth rate (FCGR) data of pipeline steels in a gaseous hydrogen environment, to understand the process of hydrogen-enhanced FCG and the influence of major process variables such as material strength, hydrogen pressure, and loading conditions, and to provide a basic data set for recommendation of code update and modification. Complementary work on a new fracture toughness testing method, on characterization and fatigue testing of welds, and on new welding procedures and materials is being conducted by a team from Oak Ridge National Laboratories, the University of Tennessee, and the Ohio State University. That work was done on a separate DOT project. The two projects were coordinated by Mr. Louis Hayden.

In order to produce the FCGR data efficiently, an innovative multi-specimen link system was successfully designed and used for the tests. This system allows simultaneous testing of up to ten specimens in a high-pressure hydrogen environment.   Particularly at low loading frequency, this greatly improves the productivity of the testing.

Fatigue crack growth experiments were performed on X52 and X70 steels in both air and hydrogen gas pressurized to 5.5 MPa and 34 MPa. Experimental results indicate that the presence of gaseous hydrogen increases the FCGR of all materials tested. At lower values of ΔK (ΔK values between 7 MPa·m$^{1/2}$ and 9 MPa·m$^{1/2}$), the increase in FCGR may be modest over that of air; whereas the FCGR is vastly increased over that of air for higher values of ΔK. The rate of FCG approaches that of air for ΔK values below about 7 MPa·m$^{1/2}$ and above about 15 MPa·m$^{1/2}$. Hydrogen-assisted FCGR appears to increase with increasing hydrogen pressures at ΔK values below approximately 15 MPa·m$^{1/2}$. However, the FCGR response for all materials in all hydrogen pressures tested appears to fall within a relatively narrow band. Furthermore, decreasing the test frequency has an effect similar to increasing the hydrogen test pressure. FCGR does not appear to be affected by the strength of the steel, as it is in monotonic tensile testing. FCGRs of X70 were not significantly different, meaning that results did not fall outside of the experimental uncertainty, than those for X52.

A hydrogen diffusion model was developed under a moving-source framework. It provides a new view point toward the hydrogen-enhanced fatigue crack growth (HA-FCGR), and its solution is able to explain the rate-limited, transient process in HA-FCGR. Given the fundamental material properties such as hydrogen diffusivity and yield strength, the model is

able to predict the upper bound of the HA-FCGR and the influences of major process variables such as hydrogen pressure, load ratio, and load frequency.

A phenomenological model was also proposed which separates the overall FCGR into three dominant mechanisms. First, the model assumes that the FCGR is comprised of a superposition of "pure fatigue" and a hydrogen-assisted component. Second, the hydrogen-assisted component is further separated into a hydrogen accumulation-dominated component and a ΔK-dominated component. The model performs well in predicting the FCGR of the materials tested as a function of ΔK, cyclic loading frequency, and hydrogen pressure.

The test results with the correlation by the diffusion model and the phenomenological model will be presented to industries and relevant codes and standards committee for potential code update and modification.

Table of Contents

1   Introduction

As a key part of the hydrogen infrastructure, a safe and efficient method for hydrogen transportation in large volume must be developed. Pipelines are the most cost-effective and safe means of long-distance transportation for natural gas and liquid fuel products. The U.S. has over 2.3 million miles of pipelines carrying natural gas and hazardous liquids. Of this total mileage, approximately 300,000 miles are natural gas transmission lines and 1.8 million miles are natural gas distribution lines.

Purpose-built hydrogen pipelines have been in service for more than 50 years and approximately 700 miles are currently under U.S. DOT regulation. However, the existing hydrogen pipelines are operated at relatively low pressure and are not meant for long-distance and high-volume hydrogen transportation. As the initial capital cost of hydrogen pipeline construction is high, one possibility for rapidly expanding the hydrogen delivery infrastructure is to adapt part of the existing natural gas transportation infrastructure to accommodate hydrogen.

The conversion of natural gas pipelines to hydrogen service poses many technical challenges. With extended exposure to hydrogen, especially under high pressure, the mechanical properties of linepipe steels and their welds can deteriorate. These mechanical properties can include tensile and yield strengths, fracture toughness, and fatigue resistance. It has been well documented that hydrogen can greatly reduce the fracture toughness of some steels and their welds by promoting brittle failure in otherwise ductile materials (hydrogen embrittlement). Another serious issue is that the exposure to hydrogen can greatly increase fatigue crack-growth rates in pipeline flaws. The combination of fracture toughness reduction and crack-growth rate increase could significantly reduce the service life of pipelines.

1.1   Industrial Needs for Fatigue Data of High-strength Pipeline Steels

Existing data on the effects of pressurized gaseous hydrogen on linepipe steels is limited. The amount of data available today is generally limited to lower strength pipeline steels that are less susceptible to hydrogen embrittlement, rather than higher strength steels which would be preferable for high-pressure large-volume transportation. In addition, there is no known data available on welds and their heat affected zones. The currently available data has also indicated that the presence of hydrogen can increase the fatigue crack growth rate by several orders of magnitude. The fatigue crack growth acceleration depends on the materials' chemical compositions, microstructure, mechanical properties, testing frequencies and wave shapes, etc. The most detrimental effects can be observed at lower frequencies, on the order of 0.1 to 1 Hz [1,2]. There is a critical need for fatigue testing data on high-strength linepipe steels and their welds under high-pressure hydrogen environments. The U.S. Department of Energy (Office of Energy Efficiency and Renewable Energy Hydrogen, Fuel Cells, and Infrastructure Technologies Program) recognized these issues and made them a top priority in their R&D program [3].

ASME B31.12 hydrogen codes committee has identified the need for the testing of commonly used linepipe materials to evaluate the impact of hydrogen on fatigue and fracture resistance. In addition, a hydrogen workshop held at NIST in Boulder, CO in August, 2007 noted that material properties, in hydrogen, of current and proposed higher strength pipeline construction materials and their welds were of utmost importance.

Existing natural gas pipelines were constructed from carbon-manganese steels (nominal yield strength 25 to 60 ksi) while newer pipelines (nominal yield strength 60 to 80 ksi) are being constructed of micro-alloyed steels that have a lower carbon content and small additions of niobium, molybdenum, vanadium or titanium added for strengthening. The C-Mn steels are generally considered to be immune to hydrogen embrittlement by gaseous hydrogen because of their low strength levels. However, cyclic loading conditions, in a hydrogen environment, can accelerate fatigue crack growth in steels of almost any strength level. Cyclic loading in a pipeline can occur from daily pressure fluctuations during normal operation and from upset conditions where the pipeline experiences shutdowns resulting in a near-zero pressure condition back up to full operating pressure. In most situations, a pipeline would operate in the former cycling mode, where pressure fluctuations up to 10 % of the nominal operating range may occur. While this level of pressure fluctuation may sound insignificant, a pre-existing flaw in a re-purposed hydrogen pipeline could be catastrophic under such operating conditions with hydrogen gas. Cialone and Holbrook [4] demonstrated that hydrogen can lower the J_{Ic} (fracture toughness) of pipeline steel and, even at conditions representative of the 10 % pressure fluctuation, result in premature stage III fatigue crack growth, leading to the onset of failure. The problem is exacerbated if the pipeline experiences repeated shutdowns which results in stage II crack growth and may proceed at a rate 100 times faster than that which would occur in a nonaggressive gas environment.

Somerday [5] presented the latest known data on the effects of hydrogen on the fatigue crack growth rates (FCGR) in carbon steels. This work clearly showed that FCGR in carbon steels can increase by a factor of 10 at the higher range of ΔK (range of fracture intensity factor) due to the effect of hydrogen gas. Also shown are the effects of load ratio, gas pressure, cyclic frequency, and gas composition. Figure 1-1 illustrates the effect of hydrogen gas on FCGR in various carbon steels.
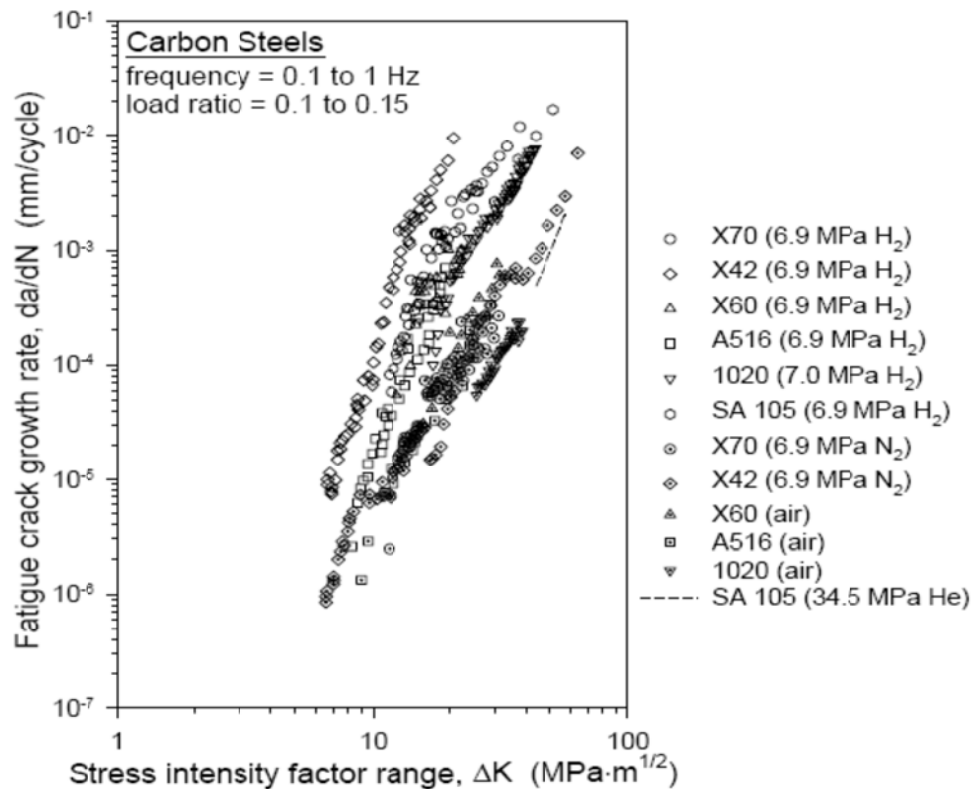
Figure 1-1 Fatigue crack growth rate vs. stress intensity factor range relationships for carbon steels in hydrogen gas. FCGR data in air, nitrogen or helium are included for comparison.

Welds in lower strength steels as well as higher strength steels are expected to compound the hydrogen damage and more research is needed to optimize welding procedures and parameters for improved fatigue performance. Most importantly, more fatigue data is needed for pipeline designers and codes and standards bodies to design a safe and efficient hydrogen transportation pipeline system. High strength steels are desired for economic reasons and are expected to pose new challenges to the hydrogen community. Until these material property issues can be resolved, hydrogen pipelines will operate at conservatively low pressures, resulting in inefficient transfer and a reduced economy scale.

1.2   Need for Update of Industrial Codes and Standards

Hydrogen pipeline systems have been in place and providing reliable transport of hydrogen gas to industrial customers for years. The reliability of these systems has been good and most failures have occurred as a result of third party damage and external corrosion much the same as natural gas pipeline systems have failed.

Current pipeline materials in the U.S. are often regulated according to the American Petroleum Institute's (API) standard 5L. The main design considerations outlined in API-5L are based on alloy chemistry, tensile strength, and toughness requirements. Pipeline steel grades are designated by their yield strength (σ_y) in ksi (kilo psi, 1 ksi = 6.9 MPa). The chemical compositions of these steels are fairly simple, with maximum limits on C, Mn, S, P, and dispersoid-forming elements such as niobium and vanadium. The variations in strength (e.g., between X42 and X70) do not result primarily from variations in alloy composition, but from variations in the processing route of the steel. Thermo-mechanical processing allows the yield strengths of pipe steels to be tailored through combinations of grain refinement, precipitation hardening (micro-alloying), and phase transformations. The prospect of widespread use of hydrogen pipelines has prompted the American Society of Mechanical Engineers (ASME) to form a committee to investigate and develop a standard specifically for gaseous hydrogen pipelines, ASME B31.12, in addition to a code on hydrogen pressure vessels, ASME Article KD-10 in Division 3 of Sec. VIII. Since defect-tolerant design principles are typically used in pipeline and pressure vessel systems, specifications on FCG are sure to be incorporated in these new codes.

In 2003, The American Society of Mechanical Engineers (ASME) formed a task group to study the need for development of an ASME B31 Hydrogen Piping and Pipeline Design Code. This task group was comprised of members from industrial gas companies, ASME B31 pipeline code committee members, metallurgists, hydrogen pipeline design engineers and ASME volunteers with significant background and knowledge in writing in design codes.

The results of the deliberations of this task group were a recommendation to ASME that a design code was needed to help standardize the design of hydrogen piping and pipelines. This decision was based on observations that current design processes varied widely between companies, extreme conservatism was being used that resulted in high installed cost of piping and pipelines and the realization that the lack of R&D to support less conservative and more technically advanced designs was needed. The result of this recommendation was ASME's decision to proceed with development of the B31.12 Hydrogen Piping and Pipeline Code. The first edition of this design code was issued in 2008 and has been revised and republished as the 2012 edition. Currently ASME B31.12 is on a three year publication cycle.

The research data and modeling contained in the report will serve as a basis for revisions to existing language and possibly cause new sections of the B31.12 Code to be written. The B31.12 Code was originally written using what R&D data that was available, which was small in volume and dated in its approach and documentation with poor conclusions as to how the work applied to engineering design of actual systems. The 2012 edition of B31.12 still contains performance factors that reduce the design stress allowables used for piping and pipelines by significant

amounts based on service pressure and temperature. These were used in the code to assure safe conservative designs that were less conservative (by 30%) that what designers were using at the time of its writing. These factors were based on hydrogen systems operating at nearly constant pressure and temperature for most of their service life. When a shift to an operating environment of industry and commercial customers for hydrogen was considered these factors may be too conservative and no design guidance of value was given for cyclic service in a hydrogen environment. The R&D information from this project was designed to provide engineers with data to assist in the revision of the ASME B31.12 Code to account for cyclic service and reanalysis of the design factors currently in the code.

The efforts outlined above will allow hydrogen piping and pipeline systems to be safely designed in a less conservative manner while maintaining system integrity. This will allow industrial gas producers and others to design install, test and place in service piping and pipeline systems that will cost less and provide long service and possibly lowering the cost of hydrogen and making it a more competitive source of energy.

1.3   Need for Efficient Material Test Systems

A limited number of laboratories in the U.S. have the capability of testing in high-pressure hydrogen gas and an even more limited number of labs have the capability of conducting fatigue tests in a gaseous hydrogen environment. The requirement of testing at a relatively low cyclic frequency of 0.1 Hz can occupy an expensive test chamber and load frame for months during the fatigue test of a single specimen, yielding only data from a single test. It was imperative that a high-throughput, high-pressure hydrogen fatigue system be developed in order to rapidly generate the amount of data necessary for the design of a safe and efficient pipeline proposed for the hydrogen economy. The development of this test system provided a ten-fold increase in data compared to a conventional fatigue test system.

The apparatus shown in Figure1-2 for this study was designed to allowing simultaneous fatigue testing of ten specimens, according to ASTM E647-11[6]. Compact-tension specimens were tested in series under load control with a crack mouth opening displacement (CMOD) gage for each specimen. Most usefully, the test may continue running until all specimens have reached the crack length (a) specified in the standard, equal to $0.7*W$, where W is the width of the specimen. For example, in one run at hydrogen pressure of 5.5 MPa and a frequency of 1 Hz:

- ◦ **Cost for multi-specimen test: ~$390 for gases, 3 person days, 17 days machine time**

- ◦ **Cost for running the specimens 1 at a time: ~$3500 for gases, 21.25 person days** (less time needed for loading each specimen than a multi-specimen string)**, over 150 days machine time.**

As demonstrated, considerable time and resources were saved through the use of this multi-specimen apparatus.
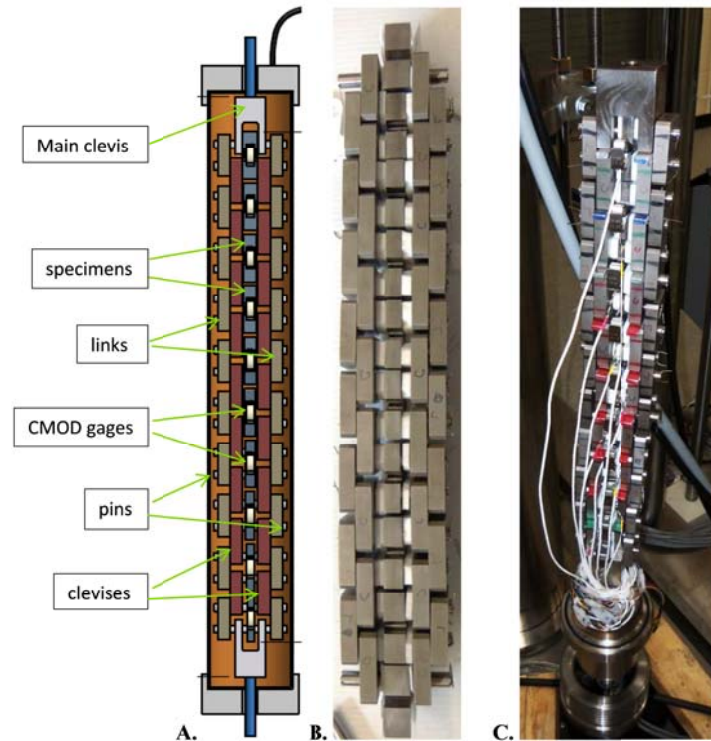
Figure1-2 Conceptual drawing (A) showing the elements of the linked chain of specimens, (B) photograph showing the assembled chain with PTFE spacers, and (C) a photograph showing the assembled chain, complete with CMOD gages and aluminum spacers, ready for installation in the pressure chamber.

1.4   Need for Understanding of Degradation Mechanism

Another issue that hinders the progress of hydrogen pipeline integration is the lack of understanding of the physical mechanisms responsible for hydrogen damage in steels. As reviewed in detail later in the report, a number of mechanisms have been proposed and built into analytical models, but none of them can provide convincing evidences and a scientific and engineering formulation to consistently explain the embrittlement process. Over the past decades, many theoretical and numerical models have been developed to study the physical mechanisms responsible for hydrogen damage. For most of the models, the embrittlement process was modeled through a stress-driven hydrogen diffusion approach. Multiple factors were identified and considered in modeling the hydrogen embrittlement process, such as hydrogen absorption, bulk diffusion and hydrogen trapping, hydrogen induced plasticity localization, etc. The modeling results correspond reasonably well to the experimental

observations from fracture and fatigue tests. Further development and validation of those models should lead to a better understanding of valuable tools for the correlation of the hydrogen environment to the degradation of mechanical properties.

1.5   Impacts on Public Safety and Scientific and Technical Merit

Under certain conditions, gaseous hydrogen could pose serious public safety hazards that are not adequately addressed by the current codes. Often times, non-hydrogen and industrial codes are referenced because of the lack of technical data. Most current hydrogen pipelines are small diameter and operate at low pressures with low operating stresses. For safety reasons, these pipelines are often constructed with heavy wall thickness and excess valves. The lack of reliable data for the design of a safe and economical pipeline transmission system forces pipeline operators to be overly conservative with their current designs. Carbon steels, the most likely candidates for a hydrogen transport system, are susceptible to hydrogen cracking and embrittlement. This work provides reliable data for the codes organizations that will help select the steels least susceptible to hydrogen damage, providing a foundation for a safe and cost-effective hydrogen pipeline design.

This work has produced three major outcomes from which the hydrogen pipeline industry and government regulators will benefit. First, the development of test equipment has demonstrated a new capability that can efficiently produce large amount of fatigue data; second, the fatigue results will provide valuable experimental data for hydrogen pipeline design and regulatory use as the tests have been designed and conducted according to the needs of industry with regards to material selection and pipeline operation conditions; and third, the experimental data has provided a much-needed basis for the modeling effort to help better understand the physical mechanisms related to hydrogen embrittlement. The predictive models have been thoroughly validated against the test data and presented in a format that is easy for codes committees and industries to use.

With its innovative design and efficiency in producing large amount of low-cycle fatigue data, the test equipment developed under the proposed work has the potential to be adapted for use by other labs and industrial R&D organizations. In fact, the equipment is being patented to aid such adaptation and protect it for use in the U.S.

1.6   Structure of the Report

The present report starts with the overall objectives of the research work and its approach in Section 2. Section 3 provides a review of the past work in the relevant areas of fatigue testing in gaseous hydrogen environment, HE and hydrogen diffusion modeling, and the current status of industrial codes and standards. It is followed by the description of the test materials and test equipment in Section 4. The test results and discussions are presented in Section 5. Section 6 and Section 7 cover the hydrogen diffusion model and the predictive model for FCGR,

respectively. The procedures of the two models and their correlations with the test data are presented in their corresponding sections. Section 8 includes a discussion on the recommendation to industrial codes and standards based on the results of the research work, including the test data and model correlation. In the final part of the report, the major conclusions are summarized and future research needs are identified.

2   Project Objectives and Approach

The project addresses the most critical issues related to the safe and efficient transportation of hydrogen using pipelines. The impact of high pressure hydrogen on the fatigue behavior of commonly used linepipe steels was studied systematically by conducting fatigue tests and developing a mechanistic-based analysis model/procedure to correlate and predict the test results. The proposed testing system can greatly accelerate the time-consuming fatigue tests and the analysis model can provide critical inputs to the test matrix design and data interpretation. The combination of the test data and analytical procedure enable a better understanding of the effects of hydrogen on the materials proposed for hydrogen transportation.

2.1   Project Objectives and Deliverables

The project objectives are to:

1.   Develop a multi-specimen, high-pressure fatigue system that can test multiple specimens at the same time;

2.   Conduct fatigue tests on well-selected practical pipeline materials;

3.   Review and identify the physical mechanisms responsible for hydrogen damage to linepipe steel from available test data;

4.   Develop mechanistic-based model and use the model to correlate test data; and

5.   Provide recommendations for code revisions for hydrogen pipelines.

In order to achieve the aforementioned objectives, the proposed work focuses on two areas: generation of fatigue crack growth data for materials proposed for use in high pressure hydrogen pipelines; and development of analysis models to understand the hydrogen embrittlement process. The main deliverables include:

1.   A high-throughput fatigue testing system capable of generating large amounts of fatigue data on materials exposed to high-pressure gaseous hydrogen at temperatures, pressures, and purities desired by the pipeline community;

2.   Fatigue data of pipeline materials;

3.   Predictive analysis models enabling in-depth understanding of the effects of hydrogen embrittlement;

4.   Recommendation for relevant code revisions; and

5.   Reports and published research papers.

2.2   Research Approach

The technical work was performed in a sequence that was designed to optimize the work efficiency and complete the deliverables on time given that designing and installing the multi-

specimen fatigue test system in a high pressure gaseous hydrogen environment is most challenging and time-consuming.

The work flow of the research work is illustrated in Figure 2-1. All the testing work was conducted at NIST's Boulder, Colorado, facility. The project team first conducted a comprehensive literature review to collect information on fatigue test data of pipeline steels. By considering the needs of hydrogen transportation industries and relevant codes and standards committees, 4 types of pipe materials for the test were selected and acquired from contributing companies. Tensile tests and microstructure characterization of these materials were performed in as-received condition. In the meantime, the design, fabrication, and installation of the multi-specimen test systems were carried out. After successful testing trials, fatigues tests on the pipe materials were performed according to the test matrix designed by the research team. The tests results were processed and eventually used by team members for modeling and correlation.
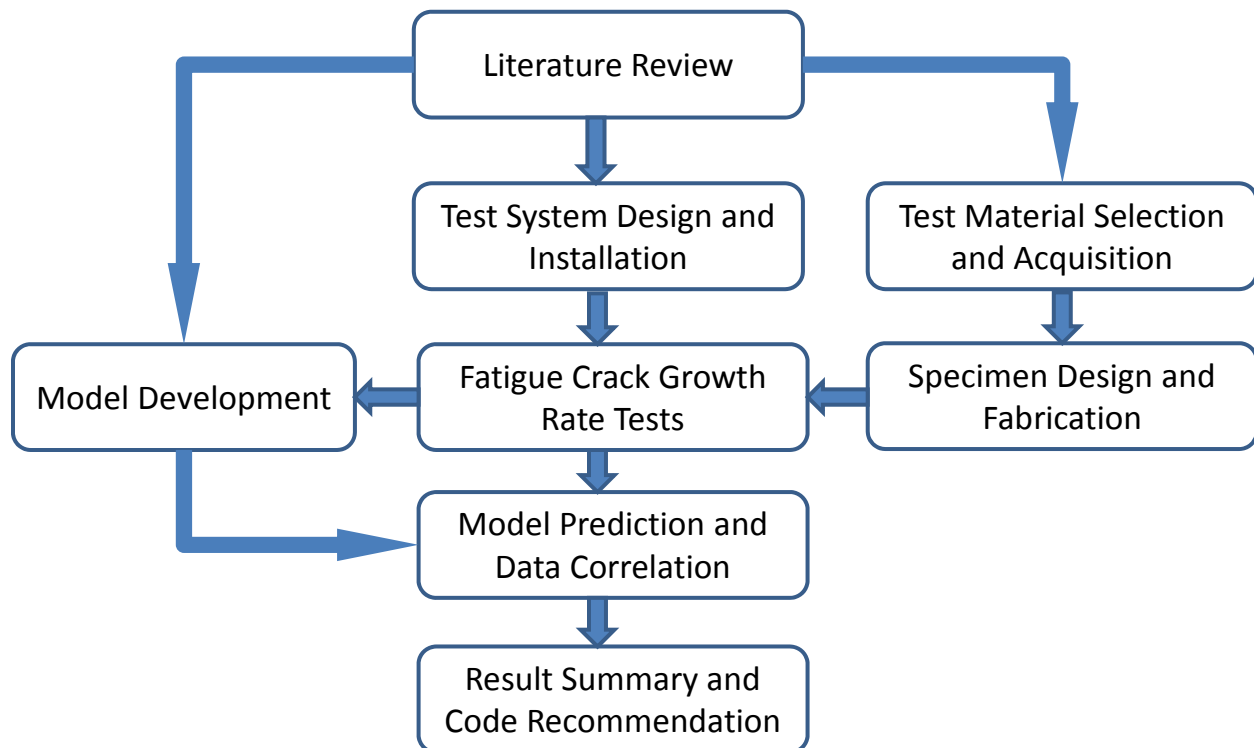
Figure 2-1 Work flow for project research

In parallel to the fatigue tests, the modeling work started with reviewing the relevant research work on hydrogen embrittlement modeling. An approach for the solving of the stress-driven hydrogen diffusion process was selected. The researchers at CRES, along with the project team, decided to focus on the correlation between hydrogen enhanced fatigue crack growth with localized hydrogen concentration instead of going into the controversial area of mechanistic

modeling based on a specific hydrogen embrittlement mechanism. NIST also developed a quantitative model for hydrogen enhanced fatigue crack growth. Both models were developed and validated with pre-existing data first. As the fatigue tests went into production mode, test data were processed and made available to the models for correlation.

Finally, the fatigue crack growth data along with their correlation with the analytical models, have been communicated to relevant industrial community and codes and standards committees. Recommendations will be made for code updates and modification.

3   Literature Review

This section reviews the status of past research work in three areas: 1) the availability of fatigue crack growth data of high-strength pipeline steels in a gaseous hydrogen environment; 2) the proposed hydrogen embrittlement mechanisms and general modeling based on these mechanisms; and 3) the modeling work relevant to fatigue crack growth in gaseous hydrogen.

3.1   Review of the Availability of Fatigue Data for High-strength Pipeline Steels in Gaseous Hydrogen Environment

The deleterious effects of hydrogen upon pipeline steels have been studied for some time. General experimental observations are compiled in Table 3-1.

Table 3-1 Degradation of Material Properties in the Presence of Hydrogen

Material Property	Effect of Hydrogen Exposure
Reduction in area (RA)	Smooth specimens: 50% less RA [7,8,9]
	Notched specimens: 80% less RA [7]
Ultimate tensile strength	Not greatly affected [2,7,8,9]
Yield strength	Not greatly affected [2,7,8,9]
Facture toughness	Reduced with increasing hydrogen pressure [4,7,8,9,10,11]
Fatigue crack growth rate	Highly affected by pressure, load ratio, frequency and gas purity [4,9,12,13,14]

By far the majority of the research performed on pipeline steels in gaseous hydrogen has been done so via monotonic or fracture testing. Fatigue testing of pipeline steels in gaseous hydrogen has been limited due to the barrier imposed by the required testing equipment. Several papers provide a general survey of the effect that gaseous hydrogen has upon the fatigue crack growth of pipeline steels [15,16,17]. Based upon the available information in the literature, one can definitively conclude the following with respect to the effect that gaseous hydrogen has upon the fatigue crack growth response of pipeline steels:

1.   The presence of hydrogen increases the fatigue crack growth rate of these steel within the Paris (Stage II) crack growth regime; and

2.   The fatigue crack growth response of pipeline steels in gaseous hydrogen exhibits a bi-linear trend.

There is either no consensus or not a sufficient amount of data in the literature to conclude other important aspects of hydrogen-assisted fatigue of pipeline steels definitively, including:

1.   The effect of load-ratio;

2.   Critical minimum and maximum hydrogen pressures;

3.   The effect of increasing hydrogen pressure; and

4. The coupling effect of frequency and hydrogen pressure.

3.2   Modeling of Fatigue Crack Growth in Gaseous Hydrogen Environment

3.2.1   Hydrogen Embrittlement Mechanisms

Degradation of mechanical properties or premature failure due to hydrogen embrittlement (HE) has been a subject of extensive research in the past several decades. The fundamental understanding of HE, however, is still not clear and controversial among researchers. In general, the proposed mechanisms of HE fall into three types: Hydrogen Enhanced Decohesion (HEDE), Hydrogen Enhanced Localized Plasticity (HELP), and Adsorption Induced Dislocation Emission (AIDE). Each of the mechanisms was proposed for both Internal Hydrogen Assisted Cracking (IHAC) and Hydrogen Environment Assisted Cracking (HEAC). These candidate mechanisms have been reviewed extensively [18,19,20,21,22]. The essences of these three major mechanisms are briefly summarized below.

Hydrogen-Enhanced Decohesion (HEDE)

HEDE is based on the weakening of metal-metal bonds at or near crack tips by localized concentrations of hydrogen so that tensile separation of atoms (decohesion) occurs in preference to a slip system. Very high hydrogen concentrations might occur in front of the crack tip if very high elastic stresses are present. The weakening of bonds is caused by decreases in electron-charge density between metal-metal atoms due to the presence of interstitial hydrogen atoms. In a typical HEDE analysis, predictions are derived from the knowledge of crack tip stress, hydrogen concentration at damage sites, and its relationship with the interatomic bonding force vs. atom displacement law. While the theory suggests effects of hydrogen on metal bonding, results are limited by the capabilities of modeling and necessary assumptions.

Hydrogen Enhanced Localized Plasticity (HELP)

HELP is based on localized softening by solute hydrogen in the form of hydrogen atmospheres around both moving dislocations and obstacles to dislocations in a volume of material ahead of cracks. Since hydrogen diffusion is rapid in the temperature and strain-rate ranges where HE generally occurs, these atmospheres can adjust themselves readily in response to changing elastic stress fields, such that the total elastic energy is minimized when dislocations approach obstacles. Consequently, the resistance to dislocation motion due to obstacles is therefore decreased, and dislocation movements are enhanced. Since hydrogen concentrations are localized near crack tips due to hydrostatic stresses or entry of hydrogen at crack tips, deformation and plasticity are facilitated locally near crack tips and crack growth takes place by a more-localized process of microvoid-coalescence than that in an inert environment.

Like HEDE, HELP is limited by lack of supporting experimental evidence and its application in practical modeling analysis.

Adsorption Induced Dislocation Emission (AIDE)

Lynch proposed AIDE by arguing that hydrogen-induced weakening of metal-atom bond strength results in enhanced emission of dislocations from crack tip surfaces where H is adsorbed [19]. The high stresses required for dislocation emission and dislocation activity in the plastic zone ahead of cracks lead to the formation of small voids at particles or at slip-band intersections. Consequently, crack growth occurs primarily by dislocation emission. AIDE has been debated, similarly, due to its lack of supporting experimental data and is limited in modeling applications and analysis.

Regardless of the controversial hydrogen embrittlement mechanisms, it is widely accepted that the excessive hydrogen concentration in the region where high hydrostatic stresses exist is the primary condition for mechanical property degradation to take place. In fact, experimental data consistently supported the conclusion that the kinetics of the hydrogen reaction at the crack tip surface and hydrogen transport from the crack tip to the internal fracture damage location dominates crack growth. Consequently, a large number of models have been developed to understand the hydrogen permeation and diffusion processes and their interactions with the stress-strain field around the crack tip. Gangloff provided a comprehensive review on these models [22].

3.2.2 Mechanistic and Kinetics Models for Hydrogen-Assisted Subcritical Crack Growth

Hydrogen embrittlement can happen in many forms, depending on conditions such as materials, loading situation, and the way hydrogen is introduced into the materials. Hydrogen degradation of the crack propagation resistance of high strength alloys, for example, can be categorized as either Internal Hydrogen Assisted Cracking (IHAC) or Hydrogen Environment Assisted Cracking (HEAC), respectively. These two types are distinguished by the source of offending hydrogen atoms supplied to the fracture process region, but otherwise share the same or similar aspects of the fracture process. In IHAC, hydrogen is introduced or "charged" into the bulk material; subsequent loading causes redistribution of the hydrogen from the surrounding to the crack tip to promote crack growth. The HEAC, on the other hand, is characterized by localized hydrogen production at the crack tip, the diffusion of hydrogen into the fracture process zone, and the subsequent embrittlement.

In general, modeling of HE can be divided into two types. The first type is a mechanistic model where crack tip mechanics, hydrogen diffusion, and the interactions between stress, plastic strain, and hydrogen concentration around the crack tip are treated in a framework based on a particular HE mechanism such as HEDE or HELP [23,24]. The second type of models focus on the kinetics of the HE process based on the premise that the hydrogen-assisted cracking process is controlled by the rate limit of the surface reaction and hydrogen diffusion [25,26,27]. The basic objectives of HE modeling include the prediction of the dependence of threshold stress

intensity and subcritical crack growth on environmental, material, and loading conditions. The major components of the model often include

1. Crack tip stress and plastic strain distributions;

2. Crack tip hydrogen concentration; and

3. Interaction between stress, plastic strain, and hydrogen diffusion and trapping around the crack tip.

While a large amount of modeling work on HE has been accumulated over the past decades, hydrogen-assisted fatigue crack growth (HA-FCG) has received relatively less attention for modeling. For HA-FCG modeling, most of the effort has been made primarily on enhanced crack growth in aqueous solutions such as those by Thompson and Wei; and Wei and Simmons [28,29,30]. Nevertheless, similar modeling approach or principles can be applied to situations where fatigue crack growth is exacerbated by the presence of gaseous hydrogen. Kotake [31], for example, following the approach by Sofronis [32,33], developed a two-dimensional model to investigate the effects of cyclic loading on hydrogen concentration near the crack tip. Under the framework of the HELP mechanism, the model formulated the interaction of hydrostatic stress, the plastic strain, and the hydrogen concentration around the crack tip by considering hydrogen diffusion and hydrogen trapping. As sophisticated as these types of models are, uncertainties of the micromechanical and thermodynamic parameters in their formulations often render them ineffective for practical purposes such as data correlation or structure integrity assessment.

A large number of kinetics models have been developed for modeling the subcritical crack growth of HEAC under quasi-static load (as opposed to cyclic load) [34,35,36,37,38,39]. These models focused on the rate-limiting nature of each step in hydrogen-assisted cracking, from the surface reaction, to the hydrogen uptake at the crack tip, and to the fracture process zone. Temperature effects on crack growth were analyzed since both hydrogen production at crack surface and hydrogen diffusion (with hydrogen trapping) are strongly temperature dependent.

When hydrogen production at the crack surface is time independent, as in the case of gaseous hydrogen environment, stress-driven hydrogen diffusion models around the crack tip are often used to calculate the hydrogen-assisted subcritical crack growth. Leeuwen [40] introduced a stress dependent term to the diffusion equation and made the postulation that a critical combination of hydrogen concentration and stress would develop at the edge of the plastic zone, and that this would produce an incremental crack extension. Johnson [41] used a moving line source solution similar to that in heat conduction problem to determine the hydrogen concentration profile in front of the crack tip. Later diffusion models included the effect of hydrogen trapping by using effective hydrogen diffusivity [42,43,44,45]. A common feature in these diffusion models was the identification of a critical distance of hydrogen damage χ_{CRIT} and a critical hydrogen concentration C_{CRIT}. The subcritical crack growth was determined by

equaling the ratio of χ_{CRIT} to the time required for hydrogen to diffuse from C_S and over this distance to $C_{CRIT,}$ where C_S is the crack surface concentration in equilibrium with the environment. These diffusion models are of the general form:

$$\frac{da}{dt_{II}} = \frac{D_{eff}}{\chi_{CRIT}} \left[\xi \left(\frac{C_S}{C_{CRIT}}, D_{Heff}, \chi_{CRIT}, \sigma_{YS}, t \right) \right]$$

where D_{Heff} is the effective diffusivity, σ_{YS} the yield strength, and ξ a function of indicated variables and takes different values depending upon the different authors of the models. As this equation indicates, the diffusion models were able to relate the subcritical crack growth to key process variables such as diffusivity, yield strength, and hydrogen environment (via C_S).
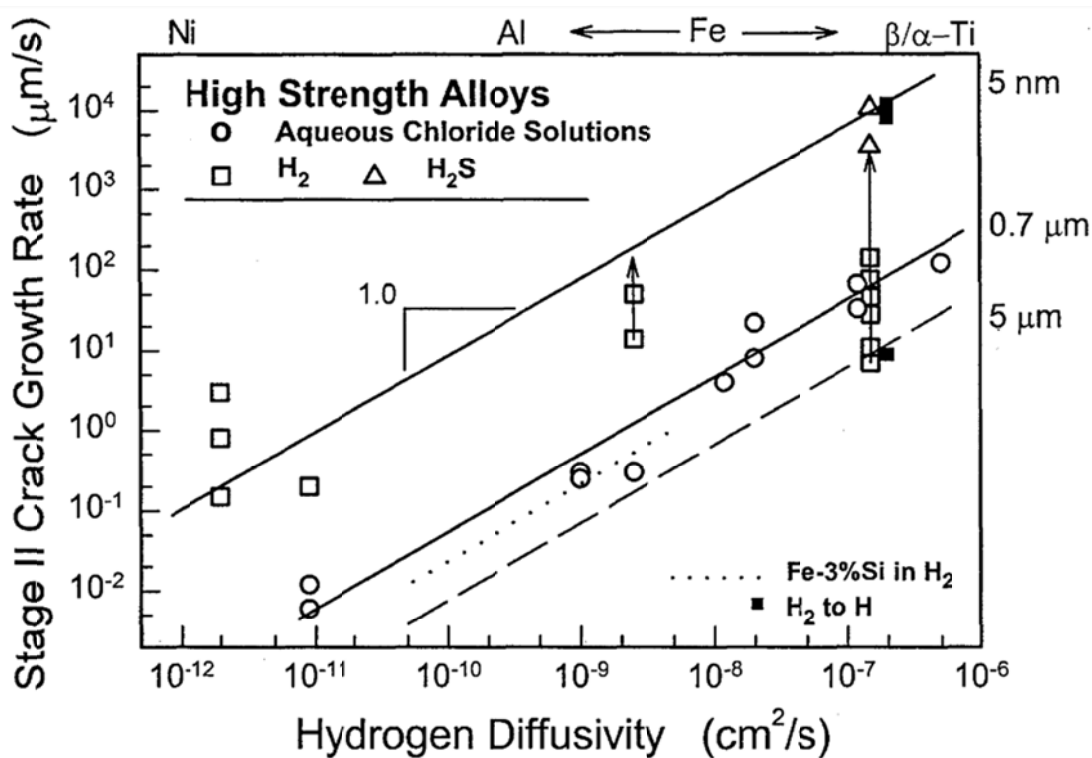
Figure 3-1 The dependence of da/dt$_{II}$ on D$_{Heff}$ for high strength alloys that exhibit HEAC in gases and electrolytes at 250°C. High strength austenitic stainless steel and nickel superalloys were cracked in high pressure (100-200 MPa) H$_2$, while maraging and tempered-martensitic steels were cracked in low pressure (~100 kPa) H$_2$. The dotted line represents TG cracking of e-3%Si single crystal in 100 kPa H$_2$ at 0°C to 125°C. Filled symbols (o) represent the transition from molecular to atomic hydrogen gas [25].

Figure 3-1 demonstrates the correlation of calculated dependency of subcritical crack growth on effective diffusivity by the above equation with measured data for different materials [25].

3.2.3   Modeling of Fatigue Crack Growth Rate (FCGR) in Gaseous Hydrogen

As mentioned earlier, the kinetics models' applications to HA-FCG have been considerably limited in the published work, and most of the modeling effort has been on enhanced crack growth in aqueous solutions. Considering the kinetics similarity between FCG in aqueous solution and in hydrogen gas, these models still can provide useful behavior information of FCG in gaseous hydrogen. For instance, model results in the works by Thomas and Wei [46,47] and Wei and Simmons [48] indicated that subcritical crack growth rate was a function of load frequency, gas pressure, load ratio, and load waveform as well as the stress intensity factor range. HA-FCG test results on high-strength alloys and pipeline steels confirmed these findings.

Gangloff and others have examined FCG models for corrosion-assisted fatigue cracking of steels due to hydrogen [49]. He examined the models of Wei as well as Austen's diffusion-limited crack growth model [50]. In addition, he examined models of both strain and stress controlled failure. Aspects of each of these models fit the data to some extent, but none of them was definitively superior. The diffusion-limited model of Austen was nonphysical and not consistent with major aspects of the data sets.

Gangloff also presented the HA-FCG modeling work for steels and aluminum alloys stressed cyclically in environments that produce hydrogen electrochemically [51,52]. These hydrogen diffusion models were successful in predicting the frequency dependency of subcritical crack growth.

To the project team's best knowledge, modeling work specific to FCG in pipeline steels under high-pressure gaseous hydrogen has not been previously reported. However, work has been reported on FCG modeling in steels, including hydrogen charging via aqueous solutions and gas charging. On the other hand, valuable experimental data recently produced by NIST and Sandia National Laboratory on pipeline steels [53,65] were made available during the model development of the current project.

Perhaps one of the valuable results from HA-FCG test for the model development was the schematic presentation in Figure 3-2 by Suresh and Richie [54]. The general trends of HA-FCG in comparison to the fatigue crack growth in an inert environment were depicted. Dependencies of HA-FCG on process variables such as load ratio and load frequency are also indicated in the figure.
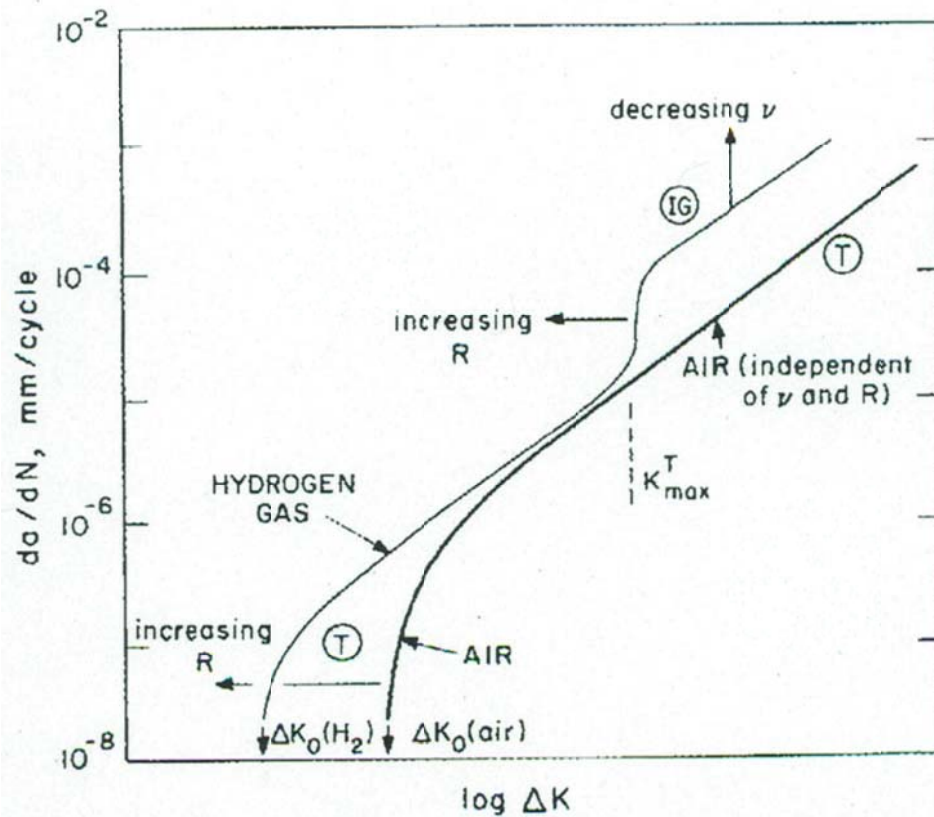
Figure 3-2 Schematic diagram of effects of gaseous hydrogen on fatigue crack growth rate. *R* denotes load ratio, ν load frequency, T for predominantly transgranular fracture, and IG for predominantly intergranular fracture [54].

3.2.4   Summary of HA-FCG Modeling Review and Current Modeling Approach

Several conclusions can be drawn from the above review of HE modeling research:

1. The mechanisms of hydrogen embrittlement, though bearing huge importance, are still not clear and controversial;

2. The mechanistic model for HELP and kinetics models for subcritical crack growth in HEAC proved to be quite successful, but significant unsolved gaps still exist;

3. Most of the modeling work of HA-FCG considered the scenario in which hydrogen was introduced electrochemically; and

4. There is no modeling work on HA-FCG of pipeline steels in a gaseous hydrogen environment.

Based on the review and the conclusions drawn above, the project team decided that a kinetics model that focused on stress-driven hydrogen diffusion would be the most feasible approach. The model should include the fundamental components of a hydrogen-assisted fatigue

crack growth process such as crack tip stress evaluation, and hydrogen diffusion that is driven by cyclic load so that the essential variables that impact the HA-FCG process can be captured and evaluated. On the other hand, the model should be kept as simple as possible for two reasons:

1. The solution of the model should be simple so that the essential variables responsible for HA-FCG can be readily evaluated. Avoiding sophisticated models would minimize the uncertainties in the model through reduced number of modeling parameters; and

2. A simple but effective model would make its development and production less expensive.

Even though the project team decided to pursue a relatively simple modeling approach, it is still a challenging task because it is a new model in the sense that no prior model has been produced to apply to a gaseous hydrogen environment for HA-FCG.

The model itself, including its components, formulation, solving process, and the result, is presented in Section 6.

In addition to the kinetics model described above, NIST also developed a phenomenological fatigue crack propagation (FCP) model based on their prior work on API-5L X100 pipeline steel exposed to high-pressure gaseous hydrogen. The semi-empirical model was predicated upon the hypothesis that one of two mechanisms dominates the fatigue crack growth (FCG) response depending upon the applied load and the material hydrogen concentration. The proposed model predicts fatigue crack propagation as a function of applied driving force (ΔK) and hydrogen pressure. The model correlates well with test results and elucidates how the deformation mechanisms contribute to fatigue crack propagation in pipeline steel in environments similar to those found in service. This model along with its correlation with the test data is presented in Section 7.

3.3   Review of Fatigue Testing in High-pressure Gaseous Hydrogen and its Challenges

Minimal work has been done to date on fatigue testing of pipeline steels in gaseous hydrogen, particularly with respect to changing load-ratios and frequencies. However, the work that has been done on pressure vessel steels may provide a basis for what one would expect in pipeline steels. Whereas some studies found a frequency dependence upon the fatigue crack growth [13,55], other studies have shown no dependence [56]. The results indicating that fatigue crack growth of steels in hydrogen is frequency dependent suggest that the fatigue crack growth rate is inversely related to the testing frequency [12, 13]. Furthermore, research indicates that load ratios less than about R=0.5 do not affect fatigue crack growth rates of steels in gaseous hydrogen [4, 9]. At load ratios above about R=0.5, the fatigue crack growth rate of steels increases as the load ratio increases. The primary reason for the lack of published data on the effect of load ratio and frequency on the fatigue crack growth of steels in gaseous hydrogen is the difficulty in performing even simple experiments in this environment.

4 Testing Materials and Testing Equipment Design

4.1   Testing Materials

4.1.1   Materials and Characterization

The materials used for FCGR testing in this study were X52 and X70 pipeline steels of varying microstructures. One of the X52 steels was a modern design intended specifically for hydrogen gas transportation, produced in 2011, and acquired from Air Liquide. The other X52 was a vintage steel from Pacific Gas & Electric (PG&E) that was placed into service in 1964. The X70 materials were both modern steels from the early 2000s. One was a steel intended for natural gas service from CRC Evans (alloy A), and the other was an experimental alloy from El Paso (alloy B) made for ease of welding. Table 4-1 shows the tensile properties of all 4 steels in the transverse orientation. Note that the vintage X52 steel does not qualify as X52, since the yield strength is too low (52 ksi = 360 MPa). The old X52 pipe was 914 mm (36 in) in diameter and had a wall thickness of 10.6 mm. The new X52 pipe had a 508 mm (20 in) diameter and had a wall thickness of 10.6 mm. The X70 pipes were both 914 mm (36 in) in diameter, with alloy A having a wall thickness of 18 mm, and alloy B having a wall thickness of 22 mm. Throughout this report X52 vintage will be used interchangeably with X52P (for PG&E), X52 new will be used interchangeably with X52AL (for Air Liquide), X70A will be used interchangeably with X70A (For CRC Evans), and X70B will be used interchangeably with X70EP (for El Paso).

Table 4-1 Tensile properties of the 4 steels

Steel	σ_y [MPa ± std. dev.]	σ_{UTS} [MPa ± std. dev.]
X52_vintage	325±4	526±4
X52_new	487±5	588±5
X70A	509±19	609±4
X70B	553±18	640±9

The chemistries of the steels are given in Table 4-2. Note that the old X52 steel has much higher carbon content than the other steels, and both X70 steels have lower carbon content than even the new X52 steel. Low carbon content enhances weldability and toughness, and low carbon content represents the general trend in pipeline steelmaking today. The X70 steels are higher in solute elements such as chromium and copper, for strengthening. The three modern steels are microalloyed with titanium and niobium to make fine precipitates and refine the overall grain size developed during thermo-mechanical-control processing. Note that the titanium content in the new X52 steel is very high, which could lead to carbide formation, which is detrimental to fatigue resistance. Preferred titanium levels in pipeline steels should be stoichiometric with N2 at a ratio of 3.4:1. A maximum of 0.025 % titanium is usually desirable. The modern X52 pipe had an ERW (electric resistance welding) seam and the vintage X52

material had a SAW (submerged arc weld) seam and both materials had SMAW (shielded gas metal arc welding) girth welds.

Table 4-2 Chemistries of two X52 steels and two X70 steels

Element	Al	B	C	Co	Cr	Cu
X52_old	0.002	< 1e-4	0.238	0.004	0.014	0.085
X52_new	0.017	< 1e-4	0.071	0.002	0.033	0.016
X70A	0.015	< 1e-4	0.048	0.002	0.240	0.220
X70B	0.012	< 1e-4	0.053	0.002	0.230	0.250
Element	Fe	H	Mn	Mo	N	Nb
X52_old	98.48	0.0001	0.96	0.004	0.003	0.001
X52_new	98.37	0.0006	1.06	0.003	0.004	0.026
X70A	97.51	0.0003	1.43	0.005	0.005	0.054
X70B	97.41	0.0009	1.53	0.003	0.005	0.054
Element	Ni	P	S	Si	Ti	V
X52_old	0.05	0.011	0.021	0.064	0.002	0.002
X52_new	0.016	0.012	0.004	0.24	0.038	0.004
X70A	0.014	0.009	0.001	0.17	0.027	0.004
X70B	0.014	0.01	0.001	0.16	0.024	0.004

Low-magnification images taken across the thickness of each pipe, shown in Figure 4-1, do not show any large-scale microstructural banding related to chemical segregation at the centerline for any of these steels. Figure 4-2 shows higher magnification images, 500X, of the X52 steels. The old steel, shown in Figure 4-2 (a), contains approximately 70 % volume fraction of polygonal ferrite (light color) and approximately 30 % volume fraction of pearlite (dark color), with a large average grain size, about 30 μm or ASTM 8, based on qualitative estimates. This grain size is typical of what would have been expected for steel processing during the 1960s

for pipeline steels. The new X52 steel, shown in Figure 4-1 (b), is a mixture of predominantly polygonal ferrite, acicular ferrite, and dispersed carbides with a fine, homogeneous grain structure of size ASTM 10, based on qualitative estimates. Enhancements in steel processing today result in a more homogeneous, finer grain structure than in the past. This finer grain structure results in improved ductility and toughness. Neither of these X52 materials shows evidence of microstructural banding related to casting through the thickness of the pipes. Figure 4-3 shows 500X images of the X70 materials. The X70A material, shown in Figure 4-3 (a), is approximately 93–94 % polygonal ferrite, about 5 % acicular ferrite, and 1–2 % pearlite, based on qualitative estimates. The X70B material, Figure 4-3 (b), is approximately 95–96 % polygonal ferrite (light color) and 4–5 % upper bainite (dark color), based on qualitative estimates. Both X70 materials are very fine grained, in the ASTM 10 to 12 range.

Microstructural characterization is very important, as different microstructures may correlate more strongly with the effects of hydrogen than does the strength of a material. The microstructures of the new X52 and both X70s have similar amounts of polygonal ferrite, but the remaining microstructural balance is different, due to the alloy/process design. Microstructural phase differences plus alloy design (solute strengthening from the additional Mn and Cr), along with process design (strain) results in the difference in strength between X52 and X70.

(a)
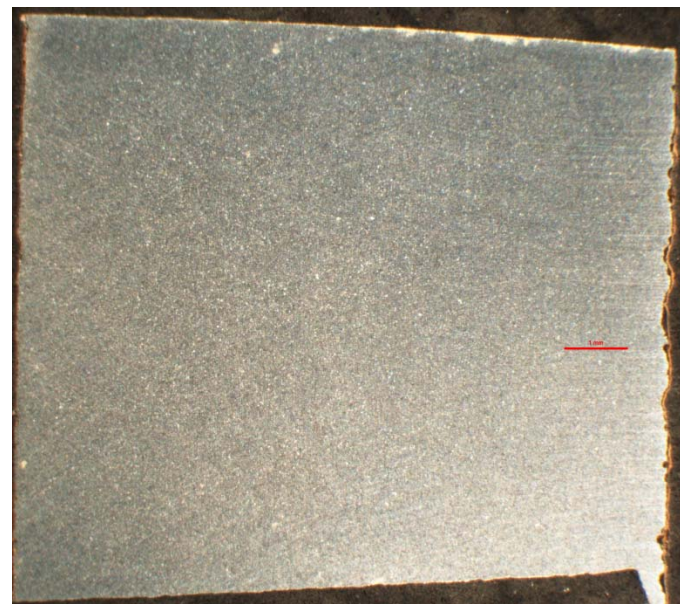
(b)

Figure 4-1 Low-magnification images of (a) X52AL and (b) X52P materials. Scale bars are 1 mm.
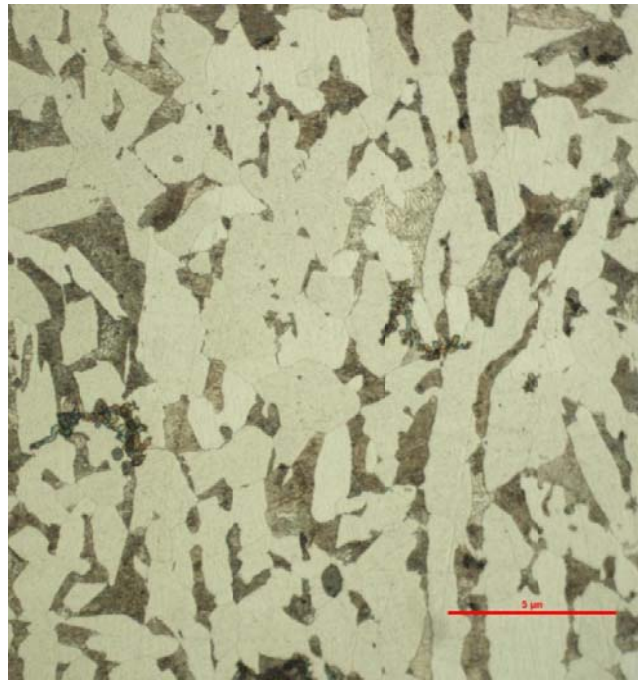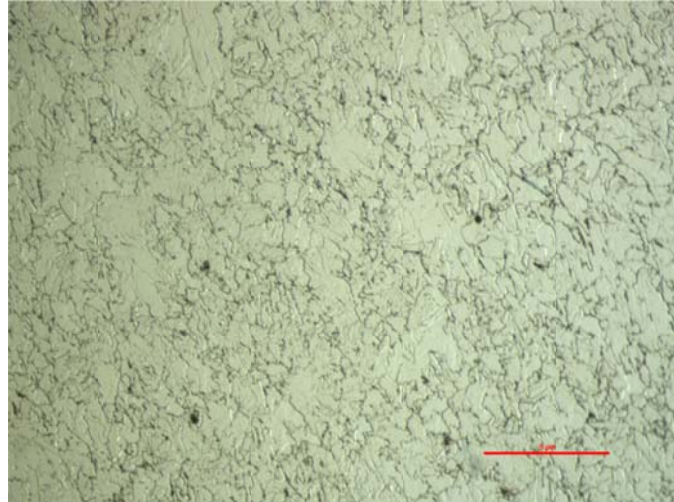
(a)

(b)

Figure 4-2 (a) Ferrite-pearlite microstructure of the vintage alloy, where the rolling direction is horizontal. (b) Microstructure of the new X52 alloy. The scale bars are 50 μm.
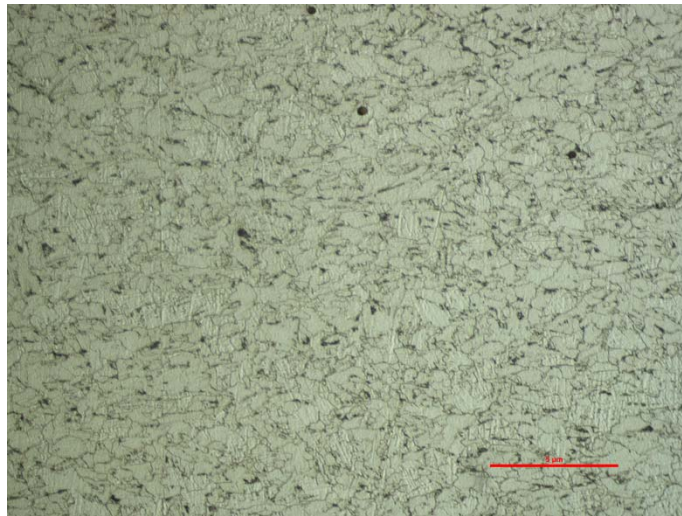
(a)
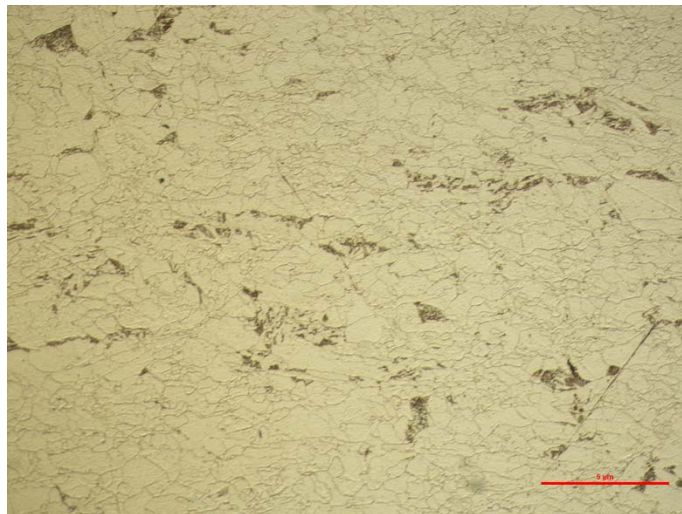
(b)

Figure 4-3 Microstructures of the two X70 steels, where (a) is X70A and (b) is X70B. Rolling direction is horizontal, and scale bars are 50 µm.

4.1.2   Testing and Purging Gases

Hydrogen gas 5.5-9s pure and helium gas 6-9s pure was supplied to us by local gas suppliers General Air and Air Products. For hydrogen gas, water should be less than 1 ppm, oxygen less than 1 ppm, nitrogen less than 3 ppm, and argon less than 2 ppm. For helium gas, water should be less than 0.2 ppm, oxygen less than 0.11 ppm, nitrogen less than 0.4 ppm, and argon less than 0.5 ppm. Each lot of hydrogen gas was tested for purity at Atlantic Analytical Laboratory. Sample bottles were filled simultaneously while the test chamber was being pressurized after the purging process.

After installation of specimens into the test vessel, three purges with ultra-pure helium (99.9999 %) and three purges with ultra-pure hydrogen (99.9995 %) were used to clean the chamber. The fourth fill with ultra-pure hydrogen was used as the test gas. Cleaning is done to primarily minimize water and oxygen contamination, as it has been shown that oxygen decreases fatigue crack growth rates [15,57], while water vapor increases fatigue crack growth rates [22,54,58]. The first two helium purges were done at 14 MPa, followed by a purge at the test gas pressure, or 14 MPa, whichever was greater. The three hydrogen purges were done at 14 MPa, followed by the final hydrogen fill at the test pressure. Sample bottles were filled during this final pressurization. An automated system, that used a program written in-house at NIST, performed these purges and kept the test vessel within 3 % of the target test pressure for the duration of the test. The automation allowed these tests to continue 24 hours a day, 7 days a week until the specimens ran their respective cracks out to a length of 0.75*w*.

Problems with the gas purity were encountered with one lot of gas and resulted in limited usable results for the X52 steels tested at a hydrogen gas pressure of 34 MPa and a frequency of 0.1 Hz, and the X70 steels tested at a hydrogen gas pressure of 34 MPa and a frequency of 1 Hz. The gas was contaminated with N, Ar, and water vapor.

4.1.3 Specimen Design, Machining, and Preparation

Pieces from each pipe were cut approximately from the 2 o'clock position of the pipe. Each piece was drawn into sections 50 mm X 65 mm, marked with the notch direction for T-L specimens, the final thickness (if other than full thickness), and sequentially numbered. See Figure 4-4 (a) as an example. The piece of pipeline material was then cut up into blanks, as shown in Figure 4-4 (b). These blanks were then sent out for machining, according to the mechanical drawing shown in Figure 4-5 (a), by one of three machinists. The thickness of the final specimen was marked on the specimen blank, rather than in the drawing. The maximum allowed surface roughness (*R*a) was specified to be 0.25 μm, according to ASTM G142 [6]. Figure 4-6 (b) shows a machined specimen.

At NIST the final dimensions were measured and recorded, and the surface finish measured with a profilometer. If the *R*a > 0.25 μm, the specimen was polished in the test section to achieve the desired surface finish. The specimens were pre-fatigued in air at a frequency of 15 or 20 Hz, a load ratio $R = 0.1$, and the final stress intensity, *K*, was less than 15 MPa·m$^{0.5}$. The typical fatigue pre-crack (FPC) was 3.25 mm. The specimens were FPCed with the use of a proprietary software that automatically calculates crack length from the compliance, based on specimen geometry and the material's strength and modulus. (This proprietary software could not be used for the actual test as it is not equipped to take input from multiple CMOD gages.)

<div style="text-align:center">(a)   (b)</div>
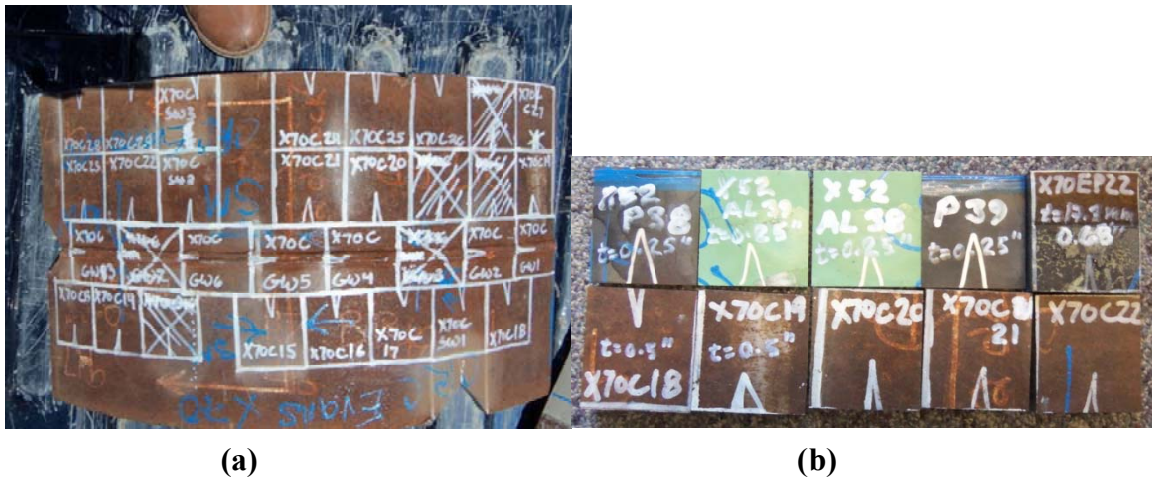
Figure 4-4 Images showing (a) a section of a pipe prepared for sectioning into specimen blanks, and (b) specimen blanks ready to be sent for machining.

<div style="text-align:center">(a)   (b)</div>
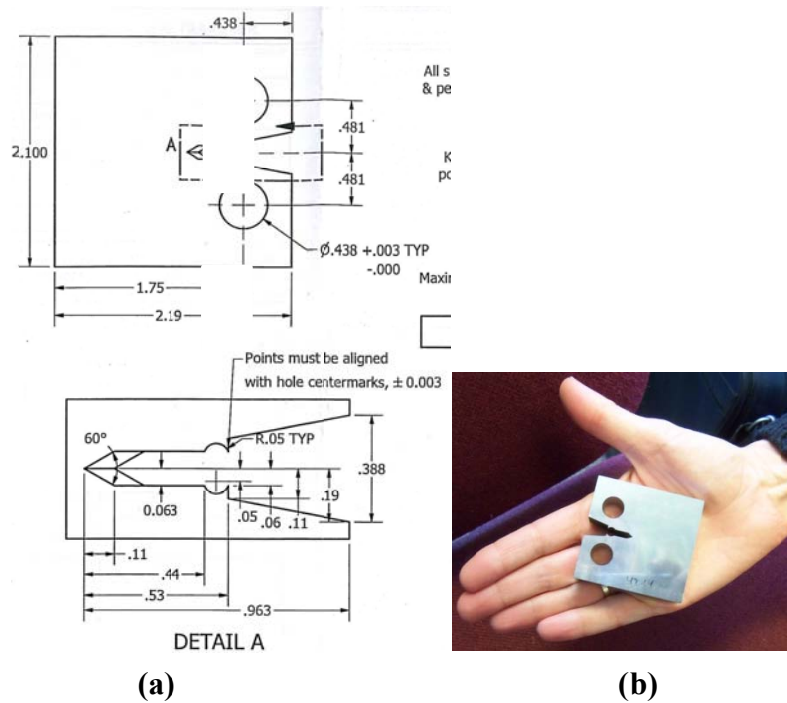
Figure 4-5 (a) Mechanical drawing for machining the specimen, and (b) an example of a machined specimen

4.2   Testing Equipment Design and Fabrication

4.2.1   Multi-Link System Design

An innovative new apparatus for measuring the FCGR of metal CT specimens has been developed at NIST in Boulder, CO. Multiple specimens can be tested simultaneously, under the same conditions, according to ASTM E647, and the results show excellent repeatability,

considering the probable inhomogeneity of these materials. The design of the fixture permits the entire set of specimens to continue fatiguing, even after some have achieved the desired crack length. This saves considerable time and resources when testing under pressurized hydrogen gas, since there is no need to vent and re-pressurize test gases when a given sample reaches maximum crack length. All specimens within the chain are exposed to the exact test conditions, eliminating possible variability in gas concentrations or impurities between tests.

4.2.2   Design of the Apparatus

As many as ten CT specimens are linked in series to one another via a set of clevises. Figure1-2 (A) is a schematic of the chain of specimens, Figure1-2 (B) is a photograph of actual specimens as assembled on a table, and Figure1-2 (C) shows the chain of specimens vertically mounted into the load frame with the CMOD gages in place. The clevises (marked with a "C" in the photographs) join one specimen to the next. These coupling clevises are designed similarly to the clevises specified in ASTM E647, which requires flattened pin holes to allow free rotation of the pins [6]. Figure 4-6 shows the mechanical drawing along with a photograph of the clevises used for this study; untreated maraging C250* was used for its strength and resistance to hydrogen embrittlement [59]. This apparatus is designed for slightly sub-sized specimens (W=44.5 mm, Figure 4-7), necessary to fit into the pressure vessel. If only the clevises are used to link the specimens together, the test would end when the first specimen in the set failed. This is shown schematically in the video in Figure 4-8.

The next element of the assembly is the links, a pair of which is connected to the sides of each specimen. As shown in Figure 4-9, the links are a similar size and shape to the clevises. The clevises span from on specimen to the next, whereas the links span across the crack of each specimen. The links have slightly elongated holes with round, rather than flattened bottoms. As the crack grows, the CMOD increases. Knowing the elastic modulus of the material being tested, one can calculate the $CMOD_f$ for $0.7*W = a_f$, the final (f) crack length. Each hole is elongated by $0.5*\Delta CMOD_{(f-i)}$, where i represents the initial condition, to allow the crack to grow only that pre-determined distance before the links are engaged, bearing the load and preventing further loading of the fully cracked specimen. The full load, however, continues to be transmitted to other specimens further down the chain via the clevises and links. Round pins are used to connect the specimens, clevises, and links, as shown in Figure1-2. An animation that schematically demonstrates the links is shown in Figure 4-10.

In order to accommodate specimens of different thicknesses, spacers made of polytetrafluoroethylene (PTFE) are inserted between the specimens and the clevises (Figure1-2 (B) and Figure1-2 (C)). This keeps the clevises straight so that the loading is aligned throughout the specimen chain. Also visible in Figure1-2 (C) are aluminum spacers placed between the clevises. These keep the chain of specimens erect and centered so that the pressure chamber can

be placed over it, enabling the end cap of the chamber and pull-rod assembly to be blindly attached. These aluminum spacers can move freely and do not interfere with the load train once the specimens are loaded in tension. Fatigue tests must be conducted in tension-tension, as the "chain" of specimens cannot support any compression.

CMOD gages with a sensitivity of 0.001 mm are attached to each specimen via knife edges that are integrally machined into the specimen at the load line (see Figure 4-7). These gages provide continuous data on the progress of the crack propagation.

Proof that the load was transmitted along the chain of specimens was obtained by attaching a calibrated proving ring (Figure 4-11) to the bottom of a chain of specimens. The top of the specimen chain was attached to the calibrated load cell of the servo-hydraulic load frame. The specimen chain was fatigue loaded at a frequency of 1 Hz, and a load ratio $R = 0.5$, while monitoring the maximum and minimum loads in the proving ring. The load values of the proving ring agreed with those of the load cell to within <2 % when the weight of the chain was ignored.

Data were acquired through the use of a procedure written in the proprietary software that can be purchased as part of the control software for the servo-hydraulic load frame. Data including time, segment, force, displacement, and output for each CMOD gage, were acquired every 200 cycles, for the duration of 5 cycles, yielding approximately 1000 data points per set. A linear regression was fit to the 1000 data points for the CMOD and the internal force. Data outside two standard deviations were excluded as electrical noise. The slope of force (P) versus $CMOD_{i=1-10}$ for the five cycles was used for the compliance when calculating a/W to solve for K and crack length, rather than the maximum values of P and ν (CMOD), as called for in Figure A1.4 in the standard, ASTM E647-11 [6].This is because variables such as temperature, humidity, and drift may, over time, affect the absolute value of the CMOD, but the change in CMOD (ΔCMOD) over a given cycle should not be influenced by anything other than the crack length.

Figure 4-6 Image and drawing with detail of a connecting clevis. Units are in millimeters and dimensions are specific to a CT specimen where W=44.5 mm.

Figure 4-7 Drawing of the CT specimen used, showing the integral knife edges

Clevis.wmv

Figure 4-8 Animation of a set of specimens connected only by clevises

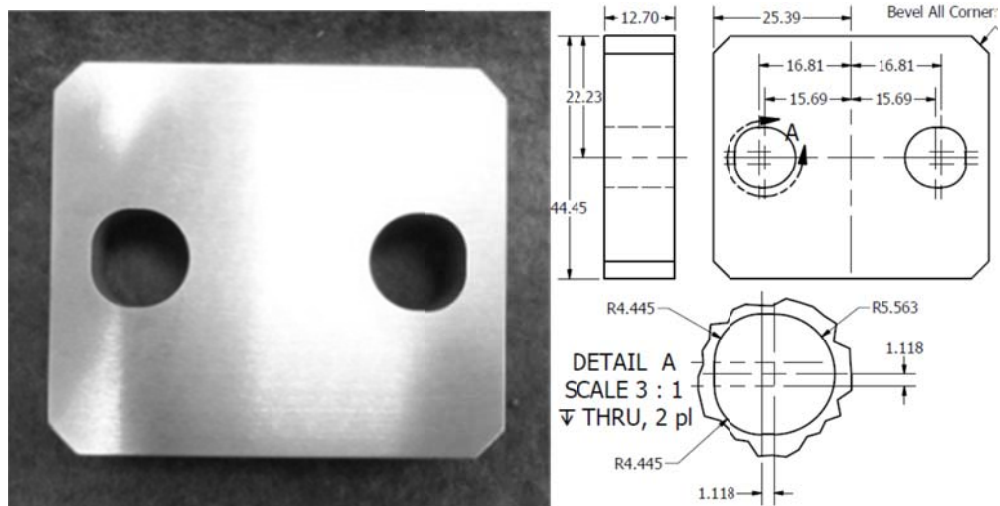Figure 4-9 Conceptual and mechanical drawings with detail of a link. Units are in millimeters and dimensions are specific to a CT specimen where W=44.5 mm.

Link showing controlled crack length.wmv
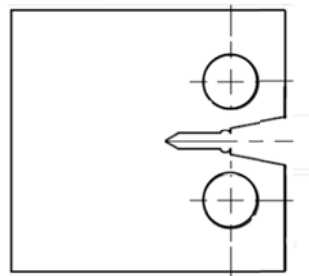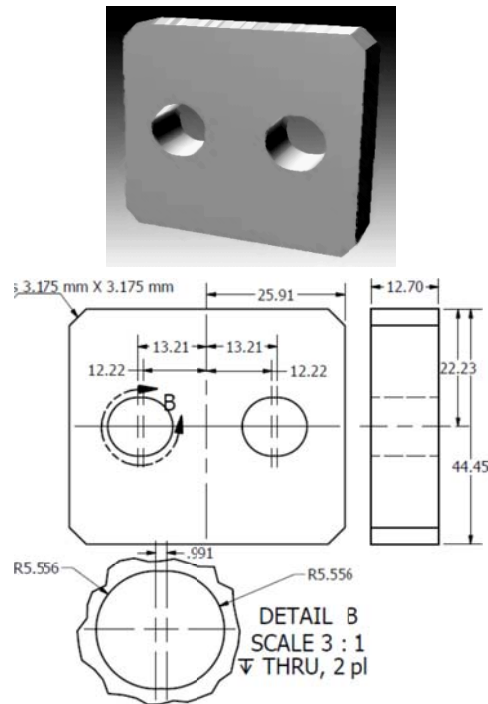
Figure 4-10 Animation demonstrating the working of the links

Figure 4-11 Proving ring with 44.5 kN capacity that was used to validate the loading of the chain of specimens

4.2.2. **The Pressure Vessel**

These tests are conducted in a stainless steel (SS316) pressure vessel that was designed and manufactured specifically for this purpose (Figure 4-12). The pressure vessel is rated to 34 MPa, has an inner diameter of 127 mm, and an inner length of 813 mm. The end caps have electrical feed-throughs that permit acquiring the signal from the gages of crack mouth opening displacement (CMOD) from each specimen and an internal load cell that more accurately measures the force *P* experienced by the specimens. In order to maintain the gas pressure within the vessel, polymeric seals are necessary, but they also create drag on the pull rod, which in turn affects the load measured outside of the vessel. Figure 4-13 shows a comparison of the forces measured inside and outside of the vessel. The applied forces for the tests are controlled by the internal load cell. The forces are applied via a pull rod connected to the actuator of a servo-hydraulic load frame. The pull rod can be seen protruding from the pressure vessel in Figure 4-12. The specimens used are a standard CT design, *W*= 44.5 mm, with integrated knife edges for attaching the CMOD gage. Tests are conducted and the data analyzed according to ASTM E647-11 for a CT specimen design.

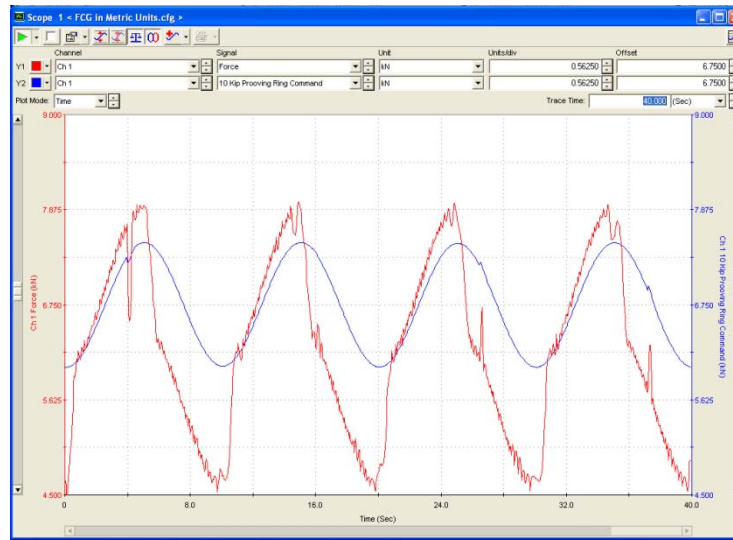Figure 4-12 The test vessel rated for a pressure of 34 MPa

Figure 4-13 Comparison of the load experienced by the external load cell (red) and the internal load cell (blue) during a fatigue test in pressurized hydrogen gas.

4.2.3 The Load Frame

The tests are conducted according to ASTM E647-11 [6], "Standard Method for Measurement of Fatigue Crack Growth Rates". A servo-hydraulic load frame is used to apply a cyclic tensile load with R=0.5. The load cell in series with the actuator has a load capacity of 240 kN. From Figure 4.2.7, it can be seen that this machine was designed to have a very long span between the crosshead, when raised to its full height, and the base of the machine. This allows us to keep the pressure testing vessel attached to and raised with the crosshead while assembling the chain of specimens, starting with attachment to the bottom end cap.

The string of ten specimens is assembled on the floor, next to the load frame. We select PTFE spacers according to the thickness of each specimen, to keep the string of specimens straight so that the load is transferred evenly along the string. Each specimen is attached to the next specimen with clevises (Figure 4-6). The top specimen uses a top clevis that is of ordinary design; the rest of the string of specimens is built using the clevises and links shown in Figure 4-6 and Figure 4-9. Aluminum spacers are inserted between clevises to allow the string to stand on its own. Links are placed over the end of each specimen, outside of the clevises, and maraging 250C pins are run through from link to clevis to PTFE spacer to specimen to PTFE spacer to clevis to the link on the far end. An end-clevis is attached to the internal load cell, which in turn is attached to the inside face of the bottom end cap. The entire string of specimens is attached to the end-clevis with a maraging 250C pin. The chamber is then lowered over the string of specimens, and the pull-rod that runs through the top end cap is blindly attached to the string of specimens by way of threads on the end of the pull-rod that mate with threads on the top end-clevis.

The chamber is purged according to the procedure detailed in Section 4.1.2. Before the last pressurization with hydrogen, the internal load cell and the CMOD gauges are electronically zeroed. The test is begun after the final hydrogen gas pressurization.

The tests are conducted in load control, based on the signal from the internal load cell, with a triangular waveform for ease of modeling the data. Every 200 cycles, data on the time, cycle, crosshead displacement, external load cell, internal load cell, and every CMOD gage are collected for five cycles at an approximate rate of 200 data points/cycle. Meters on the computer interface monitor the running minimum and maximum values of the CMOD gages. With this aid, we are able to assess the progress of each specimen while the test is running.

4.3   Test Matrix

The test matrix was designed to compare the fatigue response of materials with different strengths and microstructures to a pressurized hydrogen environment at different cyclic loading rates. Two X70 steels and two X52 steels from formed pipes were included in the test matrix (Table 4-1). Tests were conducted in air and at two different hydrogen pressures (5.5 MPa and 34 MPa), and at three cyclic loading rates: 1 Hz, 0.1 Hz, and 0.01 Hz. As the project progressed, some of the original goals were adjusted, deemed unnecessary, or incompatible with the two main objectives: 1. to determine if higher strength materials perform better, worse, or the same as lower strength materials, and 2. to determine if it is necessary to conduct fatigue tests at 0.01 Hz or if the behavior can be modeled to account for the additional time for hydrogen to migrate. For example, tests were conducted on the weld material from the X52 steels, but the X70 welds were extremely resistant to crack growth at the forces necessary to grow a crack in the base material. It was decided that the time was better spent acquiring the data at all conditions on the base material, rather than extending the tests by weeks or even months to acquire data on the X70 welds, especially as it was clear that the base material was more susceptible to FCG than are the welds. Both old and new X52 materials were tested in order to assess whether existing pipelines can be re-purposed for hydrogen use. The final test matrix is shown Table 4-3.

Table 4-3 Final test matrix

Fatigue freq (Hz)	Atmosphere	X70 CRC	X52 (new)	X52 vintage	X70 El Paso	Stress Level (ksi)	ratio
1	air	1	1	1	1	A	0.5
1	air	1	1	1	1	B	0.5
1	air	1	1	1	1	C	0.5
1	1000 psi H	1	1	1	1	A	0.5
1	1000 psi H	1	1	1	1	B	0.5
1	1000 psi H	1	1	1	1	C	0.5
1 (pre-charged)	1000 psi H	1	1	1	1	A	0.5
1	5000 psi H	1	1	1	1	A	0.5
1	5000 psi H	1	1	1	1	B	0.5
1	5000 psi H	1	1	1	1	C	0.5
1 (pre-charged	5000 psi H	1	1	1	1	A	0.5
0.1	air	1	1	1	1	A	0.5
0.1	air	1	1	1	1	B	0.5
0.1	air	1	1	1	1	C	0.5
0.1	1000 psi H	1	1	1	1	A	0.5
0.1	1000 psi H	1	1	1	1	B	0.5
0.1	1000 psi H	1	1	1	1	C	0.5
0.1 (Seam weld)	1000 psi H	1	1	1	1	A	0.5
0.1 (Girth weld)	1000 psi H	1	1	1	1	A	0.5
0.1 (trapezoid)	1000 psi H	1	1	1	1	A	0.5
0.1	5000 psi H	1	1	1	1	A	0.5
0.1	5000 psi H	1	1	1	1	B	0.5
0.1	5000 psi H	1	1	1	1	C	0.5
0.1 (trapezoid)	5000 psi H	1	1	1	1	A	0.5
0.01	air	1	1	1	1	A	0.5
0.01	1000 psi H	1	1	1	1	A	0.5
0.01	5000 psi H	1	1	1	1	A	0.5
1 (inner bend)	1000 psi H	N/A	1	N/A	N/A	A	0.5
1 (inner bend)	5000 psi H	N/A	1	N/A	N/A	A	0.5
1 (outer bend)	1000 psi H	N/A	1	N/A	N/A	A	0.5
1 (outer bend)	5000 psi H	N/A	1	N/A	N/A	A	0.5

5 Fatigue Test of High-strength Pipeline Steels

5.1. Testing Procedure

Cyclic fatigue tests were conducted on compact-tension [C(T)] specimens according to the procedure outlined in ASTM standard E647-11 [6]. Specimens were machined with a w=44.5 mm, integrated knife-edges at the load line for a CMOD gauge, and a chevron notch tip to aid in growing a sharp straight crack front. A fatigue pre-crack was grown in air in each specimen individually up to a nominal distance of 3.2 mm. Ten specimens were then linked together via the innovative testing apparatus developed at NIST and subjected to pressurized hydrogen gas. The chain of specimens was cyclically loaded at a constant load, load ratio R, hydrogen pressure, and frequency until all ten specimens completed testing (usually when each had a crack grown to approximately 30 mm). Following completion of the test, the data were analyzed according to the standard. The specifics of each of these steps are described below.

5.1.1. Specimen Pre-cracking

Individual C(T) specimens were fatigue pre-cracked in air between pin-loaded clevises. Figure 5-1 shows a specimen in the process of being pre-cracked. As shown in this figure, if the specimen was narrower than the clevis opening, polytetrafluoroethylene spacers were used to keep the specimen centered on the load line. The clevises have flattened holes, per the ASTM E647-11 standard. Figure 5-2 shows the mechanical drawing of the clevis pair. A CMOD gauge with a resolution of 1 μm was inserted at the load line, as shown in Figure 5-1, and was used to calculate the compliance of the specimen, which was used to determine the crack length. The specimens were cyclically loaded at a fatigue rate of 15 Hz or 20 Hz, and R=0.1.

The fatigue pre-cracks were established through the use of a proprietary program, purchased from the manufacturer of the testing frame and its controller. The program automatically calculates the crack length from the inputs of compliance (CMOD/force) and the specimen properties (strength, elastic modulus, and Poisson's ratio) and geometry. The standard states [6] in Section 8.3.1 that, "In addition, the fatigue pre-crack shall not be less than 0.10B, h, or 1.0 mm, whichever is greater." where B is the specimen thickness and h is the width of the notch. In every case the greatest value for the specimens tested here is h. Nominally, that value is 3.2 mm, but in actuality the width of the machined notch ranged from 3.1 mm to 3.6 mm. The proprietary software requires the user to specify the desired length of the pre-crack. It also requires the user to specify the stress intensity factor K at the end of the pre-cracking procedure, as the standard requires the K at the end of pre-cracking to be less than the initial K of the actual fatigue test. The program automatically adjusts the applied force to get the crack to grow, then "load sheds" so that the final crack segment is grown with a K equal to or less than that which was stipulated. For these specimens, the final pre-crack value for K was either 14 MPa·m$^{0.5}$ or 15 MPa·m$^{0.5}$.

Figure 5-1 Image of specimen pre-fatiguing. A CMOD gage is shown inserted at the load line. The specimen is connected to the clevises via pins.
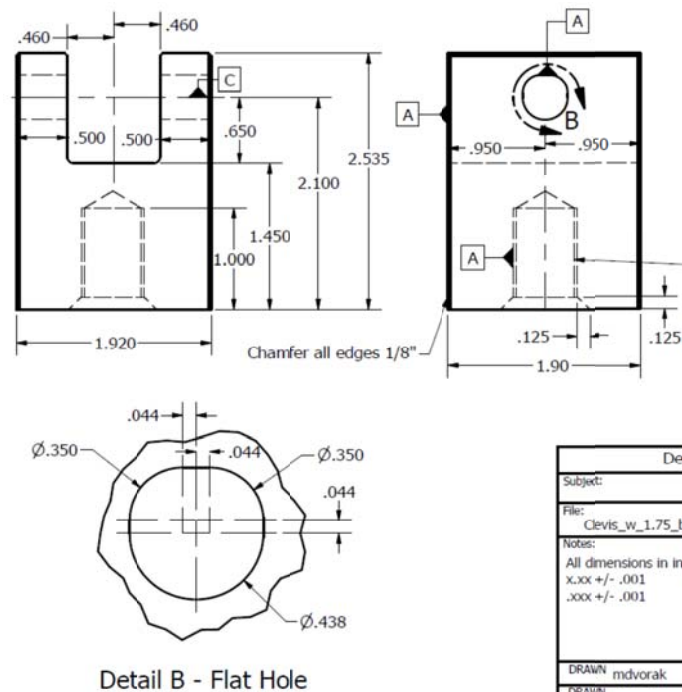

Detail B - Flat Hole

Figure 5-2 Mechanical drawing of the clevises used for pre-fatiguing

5.1.2. Specimen Pre-charging

No hydrogen pre-charging took place in the course of this testing program. Since thin specimens complete more rapidly than thick specimens, one might be able to infer that the thick specimens within a chain of specimens might behave in a manner similar to that of pre-charged specimens. The data show no difference in the fatigue crack growth rate of a specimen

completed in 4 days and one completed in 4 weeks, as illustrated in Figure 5-3. This test was conducted in hydrogen gas pressurized to 5.5 MPa at a frequency of 1 Hz.
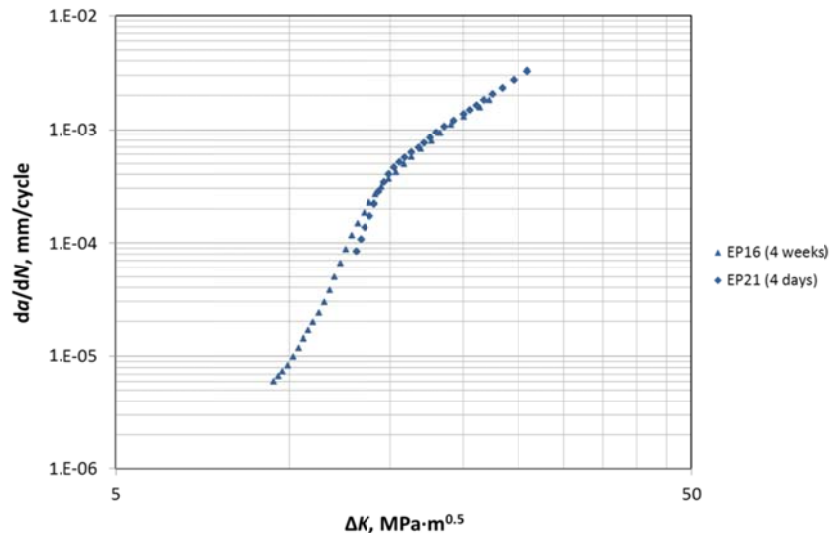

Figure 5-3 Data showing the FCGR of two X70 specimens; one completed testing in four days, the other in four weeks. The FCGR is very similar in both specimens, despite one being held at a hydrogen gas pressure of 5.5 MPa for 24 days longer than the other.

5.1.3. Testing System Instrumentation

The signal from the CMOD gages was converted from voltage to mm via strain conditioners. The CMOD signal was then fed into the controller for the test frame. About mid-way through the testing matrix, we began to recalibrate the CMOD gages after completion of a chain of specimens to ensure that the hydrogen was not degrading the bond between the strain gage and the metal of the gage, which would affect quality of the gage signal.

The signal for the internal load cell was also periodically calibrated against the external load cell, and the conditioned signal was fed to the test system controller.

5.1.4. Data Acquisition

Data was programmed to be acquired for five cycles every 200 cycles at time intervals of approximately every 0.5 s, 0.05 s, or 0.005 s, depending on the cyclic loading rate of 0.01 Hz, 0.1 Hz, or 1 Hz, respectively. This generated approximately 200 data points per cycle, or a total of 1000 data points for the five-cycle collection interval. Five cycles of data were collected to increase the signal-to-noise ratio should any transient electrical signal briefly affect the data. The data collected were:

- Time

- Cycle
- Crosshead Displacement
- External Load
- Internal Load
- CMOD Gages 1 through 10.

The data were written to a text file that was periodically saved under a new filename to protect against loss of data.

5.1.5. Data Processing

The data were processed according to the ASTM E 647 standard with a preprocessing step to eliminate RF noise that was readily identifiable and unique to our system [Ref]. The preprocessing step was added due to the presence of intermittent RF interference that was being picked up by our system and superimposed on the data. We suspect that the RF interference was caused by a nearby atmospheric radar station that continuously sweeps through a range of frequencies that intermittently coincided with the resonant frequencies of the wires connecting the test chamber to the signal conditioning module. Despite shielding and grounding the chamber and wiring, the long runs necessary to connect the testing facility to our detached control facility acted as antennas that would pick up signals at certain frequencies. The noise was easily identifiable as spikes superimposed on the plot of CMOD extension versus time (Figure 5-4).
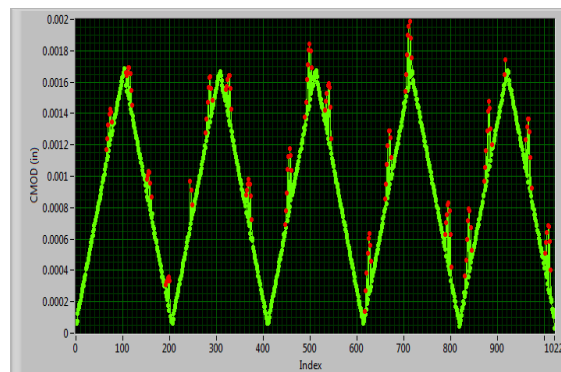

Figure 5-4 CMOD extension with respect to point index with RF noise

The preprocessing step filtered out the RF noise spikes through the use of a Bisquare linear fit whereby an initial fit was obtained and then outliers that deviated by more than a user-defined distance from the CMOD measurement (normally +/- 1.3 microns) were removed (Figure 5-5).
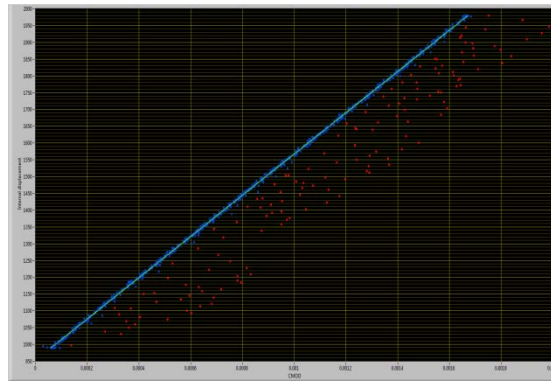
Figure 5-5 RF noise (red) being filtered from the CMOD with respect to the axial internal displacement

The resulting filtered data was then analyzed using the E 647 test method in two passes as follows: The data was saved in groups of 5 cycles out of every 200 cycles. For every group of five cycles, a compliance value, $\frac{v}{P}$, was calculated from the slope of a linear fit to the filtered CMOD opening (v) as a function of axial internal force (P). A correlation coefficient r was then calculated and r^2 was used as a pass/fail test to prevent data from being passed forward in the event of an extraneous CMOD reading. Any r^2 value higher than 0.8 was considered acceptable and that threshold was almost never crossed unless there was a physical problem, such as a CMOD gage reseating. The compliance values were then used to calculate α, a dimensionless geometric term equal to a/W, where a is the instantaneous crack length and W is the specimen width. The load range values were calculated from the average range of the axial internal force for all five peaks.

$$u_x = \left\{ \left[\frac{EvB}{P} \right]^{1/2} + 1 \right\}^{-1}$$

Eq. 5.1

$$\alpha = a/W = 1.002 - 4.0632u_x + 11.242u_x{}^2 - 106.04u_x{}^3 + 464.33u_x{}^4 - 650.68u_x{}^5$$

Eq. 5.2

where E is the elastic modulus, B is the sample thickness, and $\frac{v}{P}$ is the compliance.

During the first pass, the data were analyzed with an assumed ideal elastic modulus of 210 GPa to calculate an initial crack length. That initial crack length was calculated from a segment of data at or near the beginning of each dataset. The specimens were cooled in liquid nitrogen and broken open. The fatigue pre-crack length was measured optically from the specimen face. If the measured initial crack length deviates from the calculated initial crack length, an effective modulus is calculated from Eq. 5.1 to bring those two values into correspondence (see Figure 5-6). Normally, the first 50 compliance values were averaged to obtain the initial calculated

crack length. However, there was occasionally a settling period in which the clip gages shifted slightly at the beginning of the test. In those cases, the averaged compliance was calculated from earliest set of compliance values that could be clearly distinguished from those values that were affected by the initial settling.

Once an effective modulus was calculated, any tests that required an effective modulus greater than 240 GPa or less than 180 GPa were rejected in accordance with E647 [6]. The remaining raw data were then re-analyzed from the beginning with the new effective modulus. The data were analyzed to show crack growth intervals of 0.28 mm to reduce the data scatter. Crack lengths and cycle numbers were used to calculate the range of the stress intensity factor (ΔK) and the fatigue crack growth rate (da/dN, where N is the number of cycles) from the incremental polynomial method.

$$C_1 = 1/2\left(N_{i-n} + N_{i+n}\right),$$
Eq. 5.3

$$C_2 = 1/2\left(N_{i+n} + N_{i-n}\right),$$
Eq. 5.4

$$\hat{a}_i = b_0 + b_1\left(\frac{N_i - C_1}{C_2}\right) + b_2\left(\frac{N_i - C_1}{C_2}\right)^2, \quad \text{where:} \quad -1 \leq \left(\frac{N_i - C_1}{C_2}\right) \leq +1.$$
Eq. 5.5

$$\left(da/dN\right)_{\hat{a}_i} = \left(b_1\right)/\left(C_2\right) + 2b_2\left(N_i - C_1\right)/C_2^{\,2},$$
Eq. 5.6

where b_0, b_1, and b_2 are regression parameters obtained from a second order polynomial fit to sets of seven consecutive data points and $\hat{a}_i$ is the fitted crack length at cycle N_i.

$$\Delta K = \frac{\Delta p}{B\sqrt{W}}\frac{\left(2 + \overline{\alpha}\right)}{\left(1 - \overline{\alpha}\right)^{3/2}}\left(.886 + 4.64\overline{\alpha} - 13.32\overline{\alpha}^2 + 14.72\overline{\alpha}^3 - 5.6\overline{\alpha}^4\right),$$
Eq. 5.7

where $\quad \overline{\alpha} = b_0 + b_1 n + b_2 n^2$,
Eq. 5.8

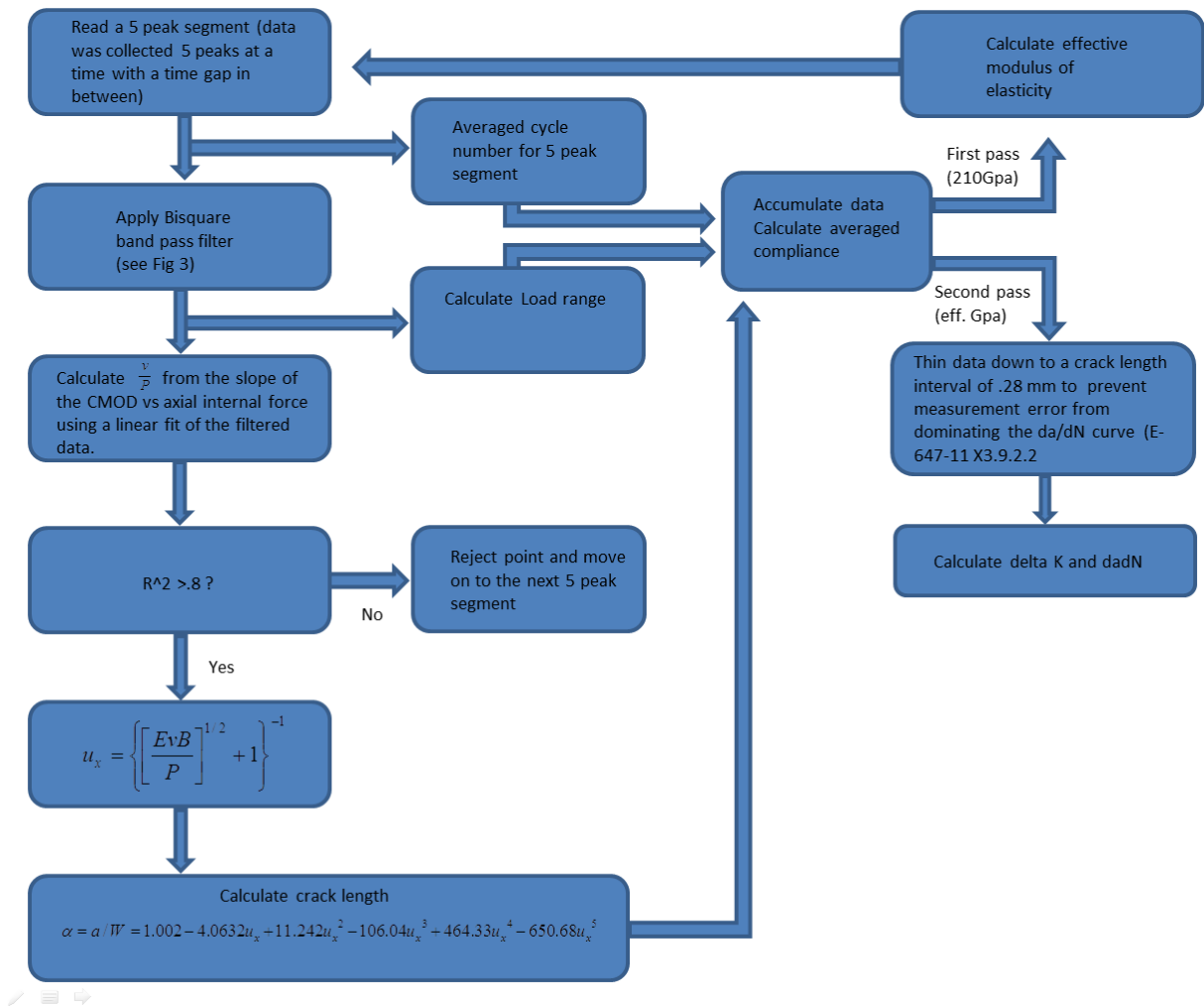and n = normalized cycle number, Δp = normalized load range (see Figure 5-7).

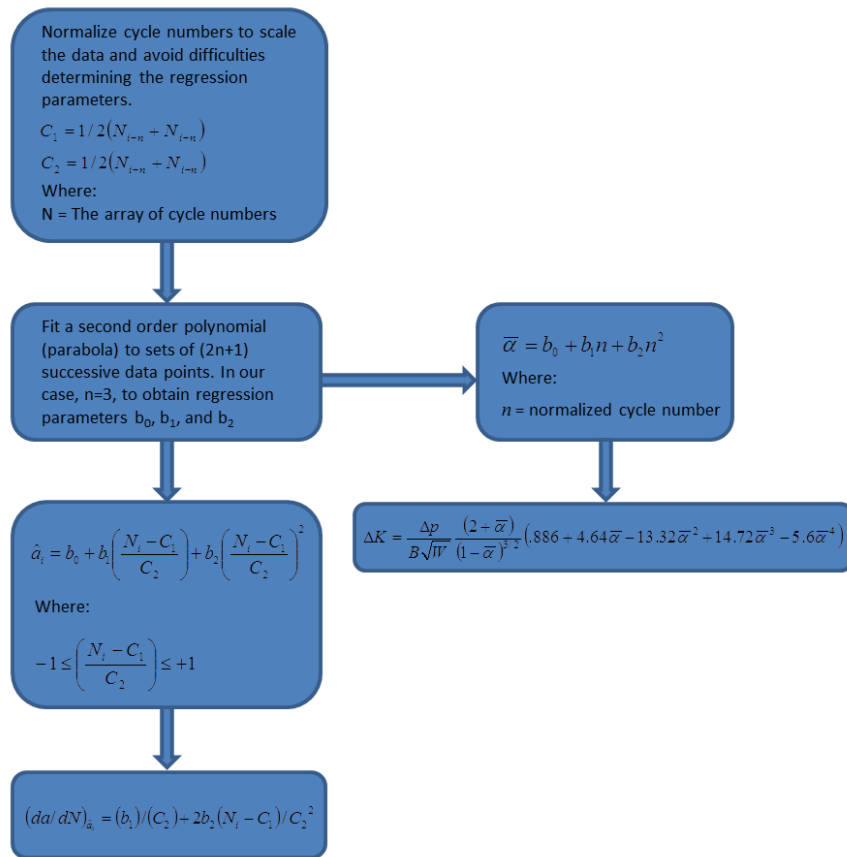Figure 5-6 Flow of steps needed to complete the data analysis

Figure 5-7 Flow of the incremental polynomial method from Appendix X1 of ASTM E647

5.2.   In-air Fatigue Test of Pipeline Steels

A chain of X52 steels and another of X70 steels were tested in air. The results are shown in Figure 5-8 and Figure 5-9, respectively. These specimens were tested with the linked system, as were those tested in pressurized hydrogen gas, but without the test vessel. Each chain of specimens was tested at a cyclic loading frequency of 1 Hz and R of 0.5. Previous work has shown that these pipeline steels are quite insensitive to loading frequency in air [4,54]. These two earliest runs were tested with a sinusoidal wave form, rather than the triangular waveform used for all the tests in pressurized hydrogen gas. Both materials behave very similarly to cyclic loading in air; the data for all four materials overlay one another in the range of ΔK from 10 MPa·m$^{0.5}$ to 25 MPa·m$^{0.5}$.
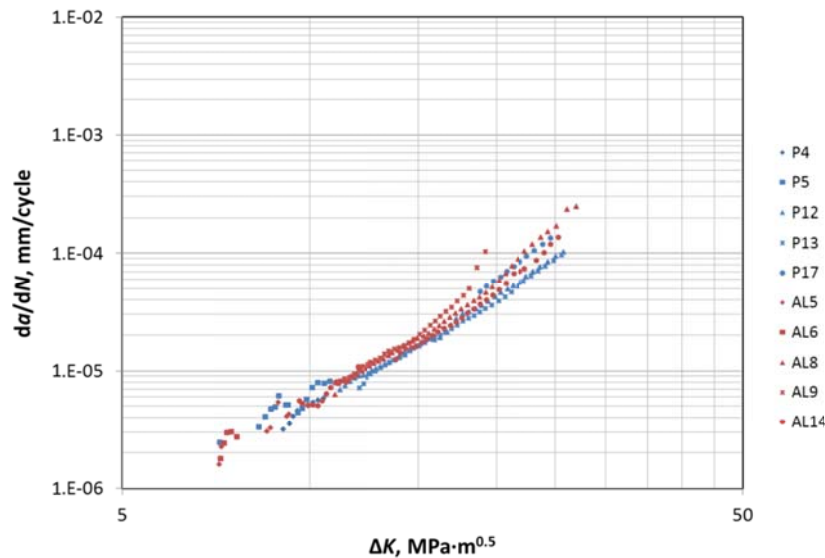
Figure 5-8 FCGR of X52 steels in air
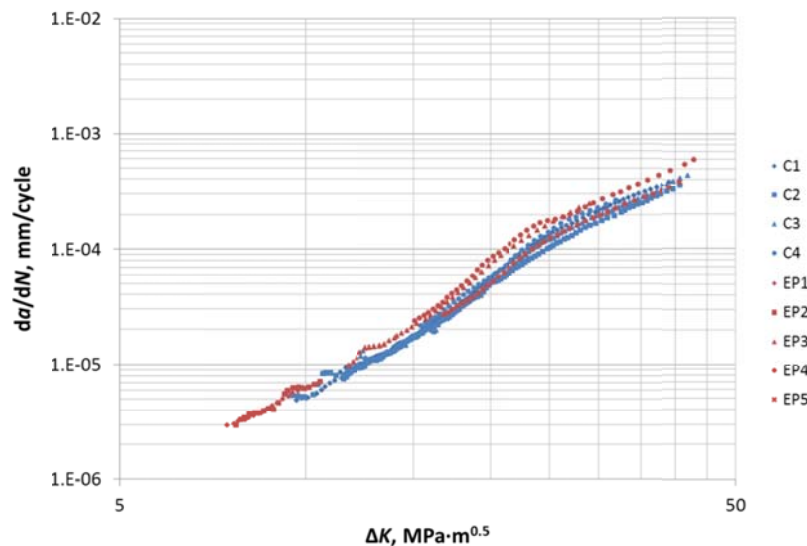
Figure 5-9 FCGR of X70 steels in air

5.3.   Fatigue Testing of Pipeline Materials in Gaseous Hydrogen

Upon loading the chain of specimens, the chamber was cleaned prior to filling with the test gas. High purity helium (99.9999 %) was used for three successive purges at gas pressures of 14 MPa, 14 MPa, and the test pressure (or 14 MPa if the test pressure was less than 14 MPa). This was followed by three purges with high-purity hydrogen (99.9995 %) at 14 MPa. The chamber was then filled with hydrogen to the test pressure. An automated system maintains the test pressure within 3 % or 170 kPa, whichever is greatest.

Gas sampling bottles were purged with helium and hydrogen at the same time that the test chamber was being purged. However, the 1 L sampling bottles were only pressurized

to 6.2 MPa because of the bottles' lower design pressure. During the last pressurization of the test chamber, one or more of the sample bottles were filled with the final hydrogen gas sample. A sample was taken for each set of ten specimens tested and sent out for chemical analysis. In particular, determination of whether oxygen or water were present in levels above 10 ppm was important, because higher levels may affect FCGRs. Presence of water has been shown to increase FCGRs, whereas oxygen can decrease FCGRs [15,57].

Prior to commencing the cyclic loading the maximum and minimum forces at which the chain would be subjected were calculated via Eq. A1.3 of ASTM Standard E647-11. Since we had a good estimate of the initial crack length from the procedure from fatigue pre-cracking and we knew the specimen geometry, we could calculate the forces for any target value of ΔK. We wanted to have data from every material and condition with an initial ΔK between 8 MPa·m$^{0.5}$ and 9 MPa·m$^{0.5}$, so the smallest value for the full thickness was used to determine our applied forces. This ensured that data was obtained in the low ΔK regime, but excessive time was not spent trying to get all of the specimens to initiate in this regime.

The chain of specimens was maintained at the test conditions (hydrogen gas pressure, cyclic loading frequency, force range, and R) until all tests were completed or the test was stopped by the operator. This time period varied from being as short as two weeks to as long as six weeks.

Upon completion of the test, the specimens were removed from the chamber, cooled in liquid nitrogen, and broken apart so that the crack lengths could be measured. The standard requires that the length of the fatigue pre-crack (FPC) be measured and the elastic modulus be adjusted to match the calculated FPC to the optically measured FPC. For consistency, the same person measured the FPC for all the specimens tested. The most accurate means to measure the FPC was determined to be with a 10× magnifying glass and a micrometer. Five to nine points, depending on the thickness of the specimen, were measured across the FPC and averaged.

5.4.   Results and Discussions

Data are shown for each set of 10 specimens that were tested in pressurized hydrogen gas in Figure 5-10 through Figure 5-16. If less than ten sets of data are displayed, it was due to one of several contributing factors:

1. The specimen hadn't begun cracking, but the other specimens were finished and we felt the necessary data was represented by another specimen.
2. The hydrogen gas was contaminated for the entire duration of the specimen's crack growth.
3. A CMOD gage fell out or failed.

4. The FPC length differed so much from the measured FPC length that the effective modulus exceeded the allowed 10 % deviation (usually due to the crack growing significantly in the first 200 cycles before the first data collection).

5. We tried to test the girth welds in the early X70 chains, but they were incredibly resistant to crack growth at the forces applied for the base metal.

The effect of contaminated hydrogen gas is clearly visible in Figure 5-14 where specimen EPSW1 (a seam weld specimen from the El Paso, X70 pipe) initially had a low FCGR, similar to that in air, followed by a sudden increase in the rate. This occurred when the hydrogen supply was switched to a purer source. The effect of contaminated gas may also have contributed to the spread in the early FCGR seen in the data in Figure 5-11. The gas analyses from both these tests showed higher than acceptable water vapor content; 1370 ppm of water vapor for the X70 steels tested at a hydrogen gas pressure of 34 MPa and a cyclic loading rate of 1 Hz (Figure 5-14), and 540 ppm of water vapor for the X52 steels tested at a hydrogen gas pressure of 34 MPa and a cyclic loading rate of 0.1 Hz (Figure 5-11).

Figure 5-17 shows a comparison of FCGRs the base metal and girth weld material from the X52 vintage pipeline for both pressures and the cyclic loading rates of 1 Hz and 0.1 Hz. There is no clear relationship between the FCGR responses of the weld material compared with the base metal for these conditions. Further tests must be conducted with sufficient specimens to obtain statistical confidence of the FCGR response.

In Figure 5-18 through Figure 5-20, representative data have been selected from each run of tests to offer a comparison of FCGR behaviors. The dataset that covered the greatest range of da/dN for a given condition was chosen. The FCGR response for a given material appears to be highly dependent on the test conditions and ΔK.

Figure 5-10 FCGR results of X52 steels tested at hydrogen pressure of 34 MPa and a cyclic loading rate of 1 Hz

Figure 5-11 FCGR results of X52 steels tested at hydrogen pressure of 34 MPa and a cyclic loading rate of 0.1 Hz

Figure 5-12 FCGR results of X52 steels tested at hydrogen pressure of 5.5 MPa and a cyclic loading rate of 1 Hz

Figure 5-13 FCGR results of X52 and X70 steels tested at hydrogen pressure of 5.5 MPa and a cyclic loading rate of 0.1 Hz
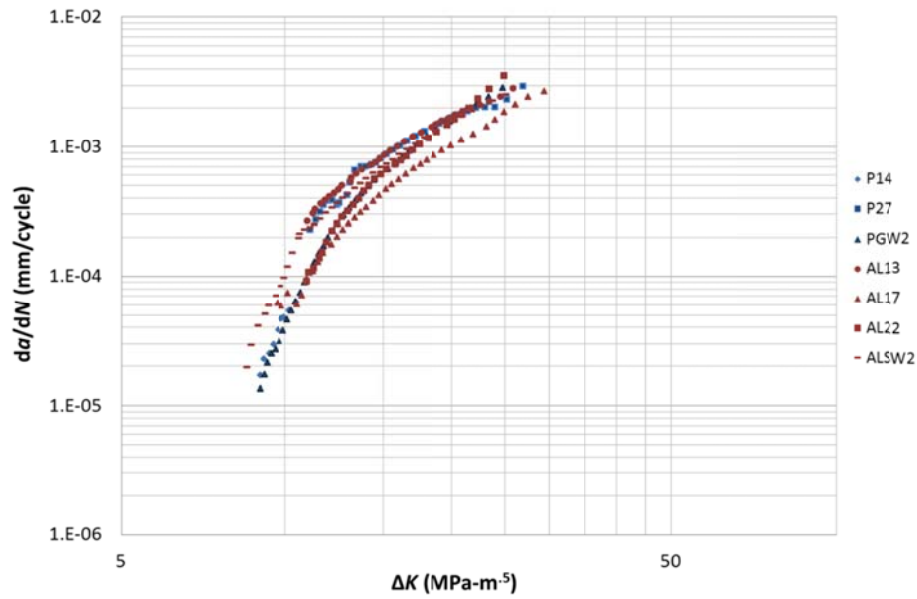
Figure 5-14 FCGR results of X70 steels tested at hydrogen pressure of 34 MPa and a cyclic loading rate of 1 Hz
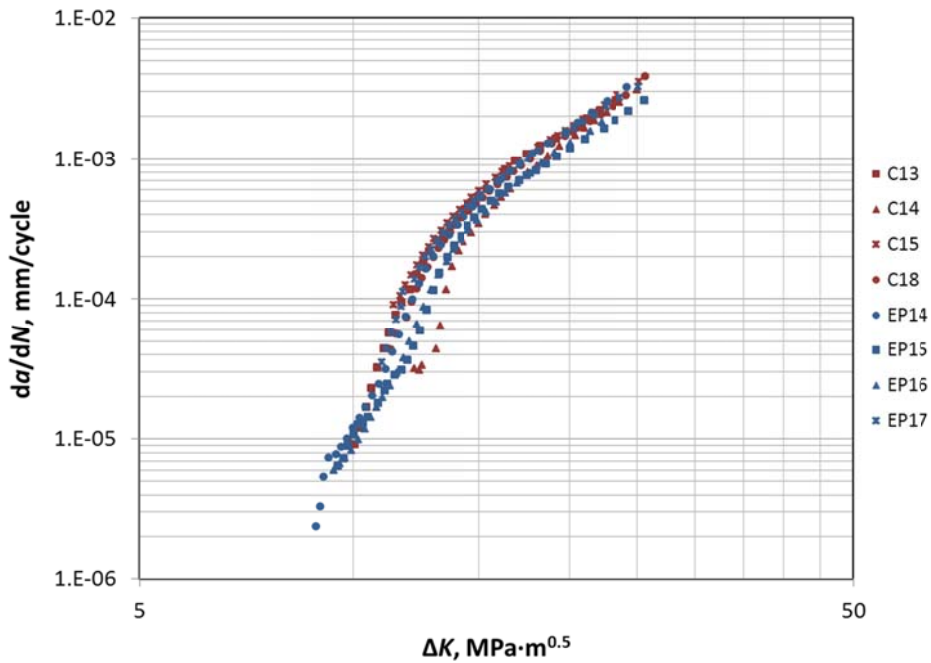
Figure 5-15 FCGR results of X70 steels tested at hydrogen pressure of 5.5 MPa and a cyclic loading rate of 1 Hz

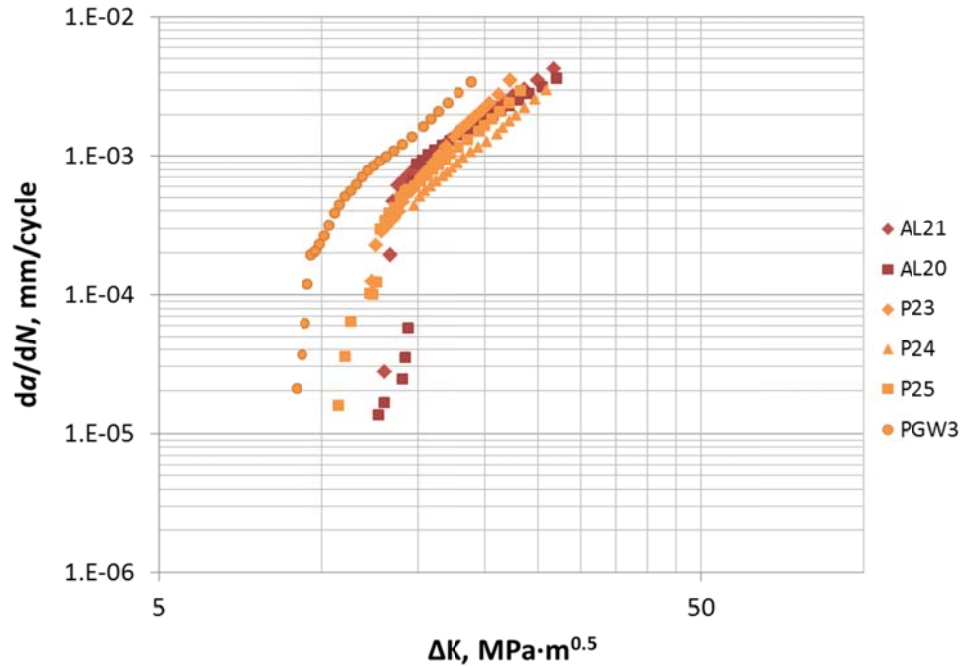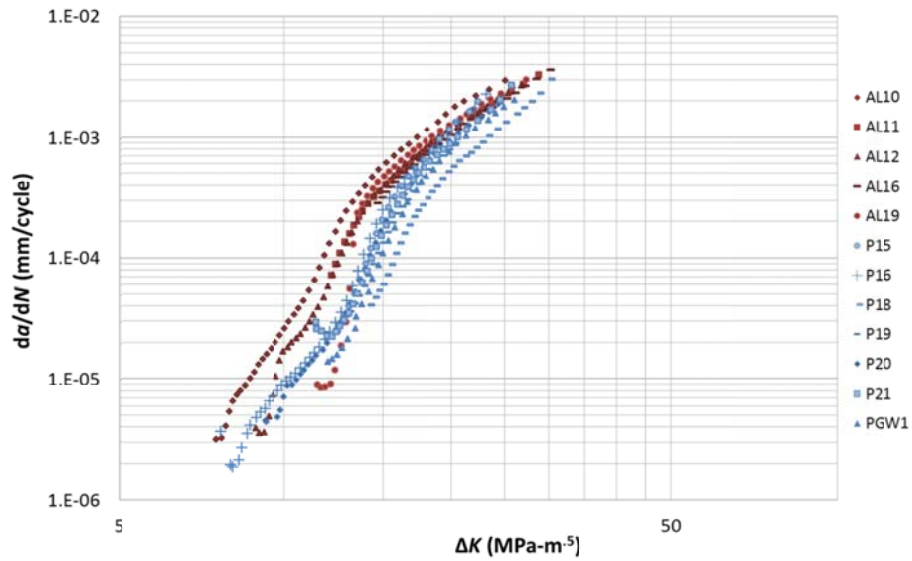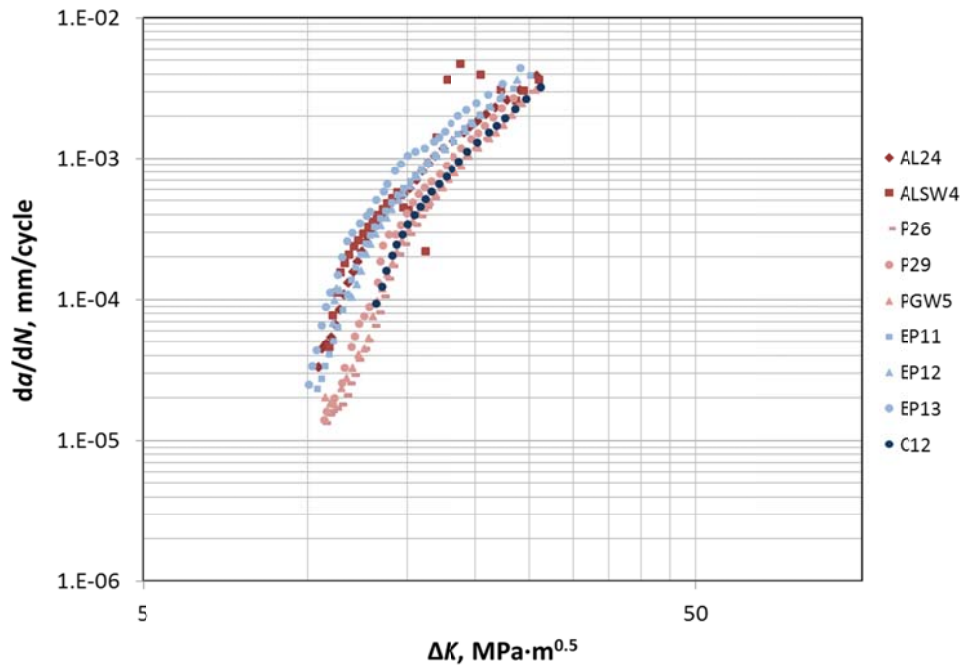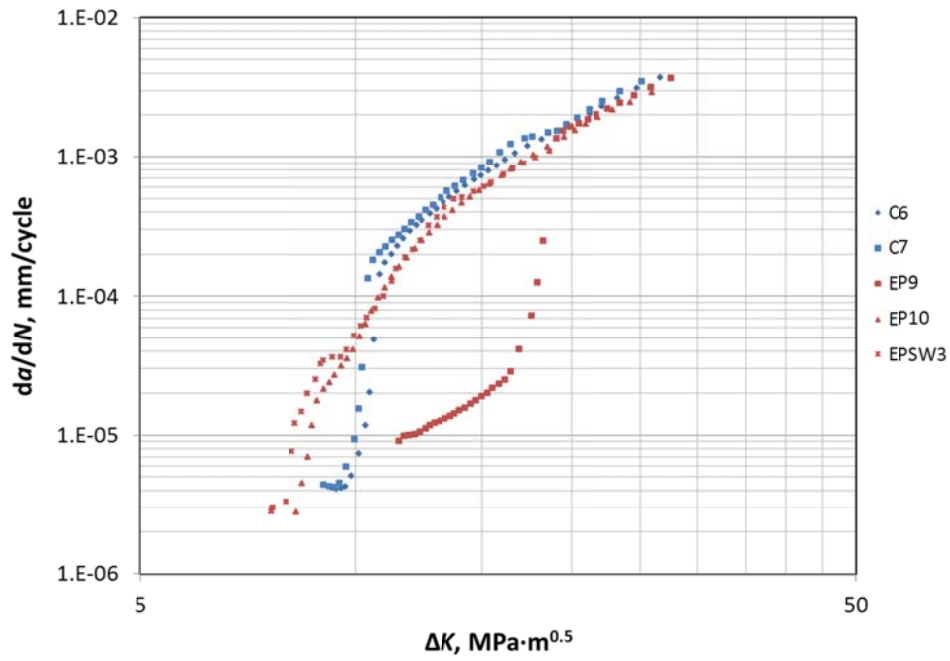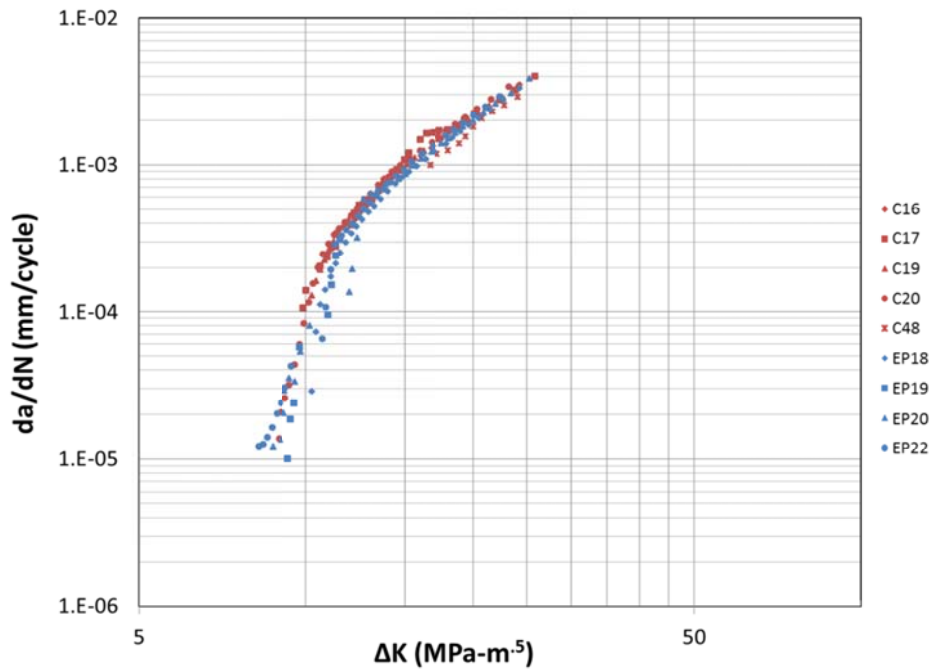Figure 5-16 FCGR results of X70 steels tested at hydrogen pressure of 34 MPa and a cyclic loading rate of 0.1 Hz
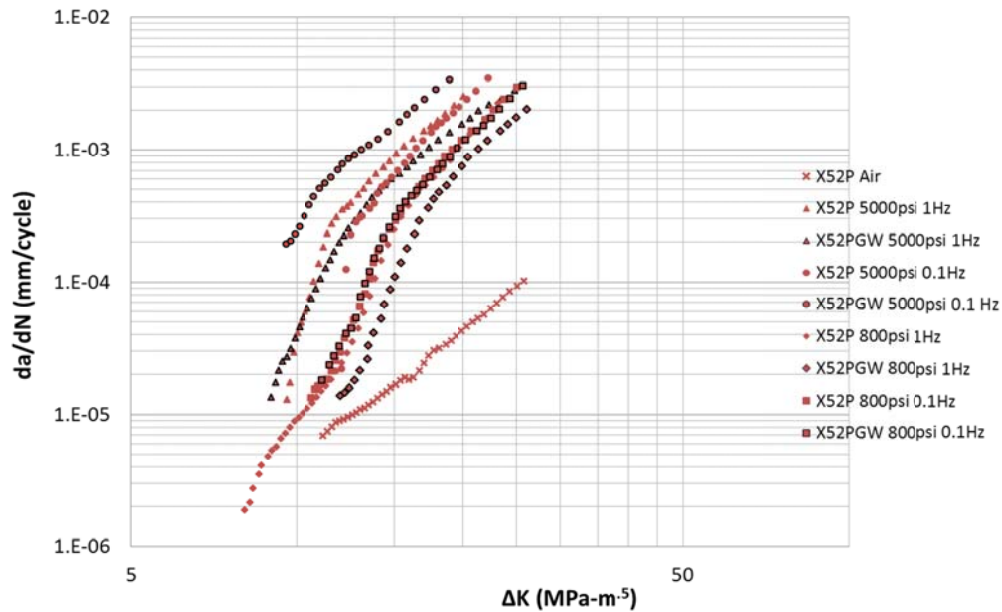
Figure 5-17 X52 Vintage material: comparison between base metal and girth weld for all conditions
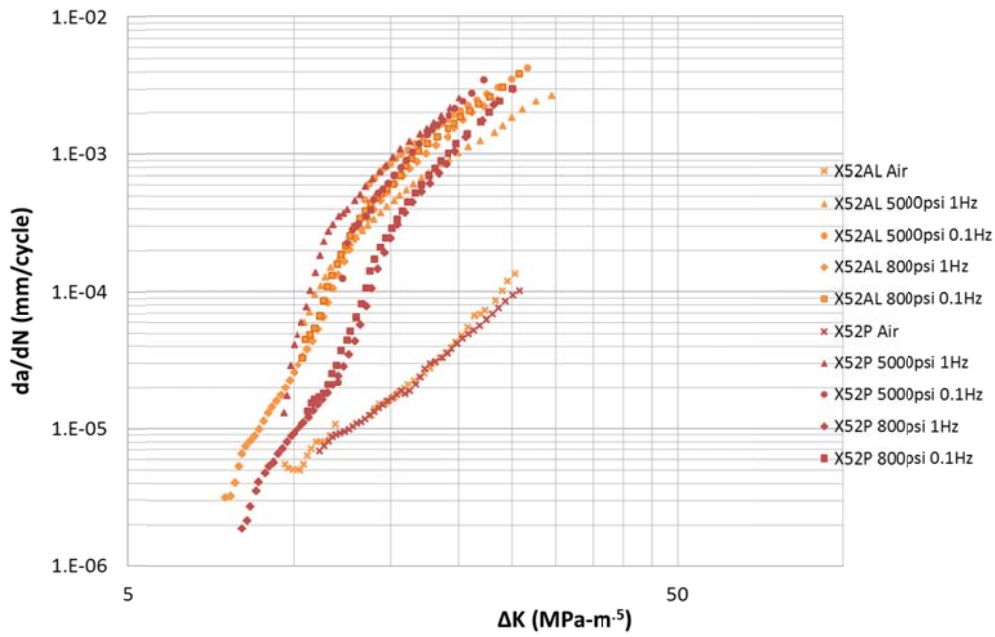
Figure 5-18 Comparison of representative data for both X52 steels for all test conditions
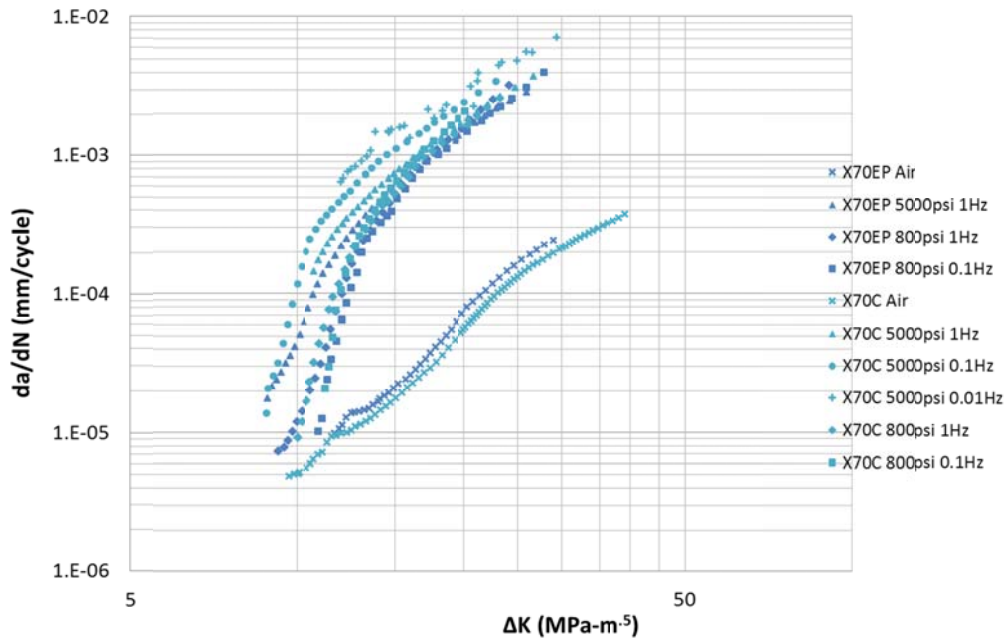
Figure 5-19 Comparison of representative data for both X70 steels for all test conditions
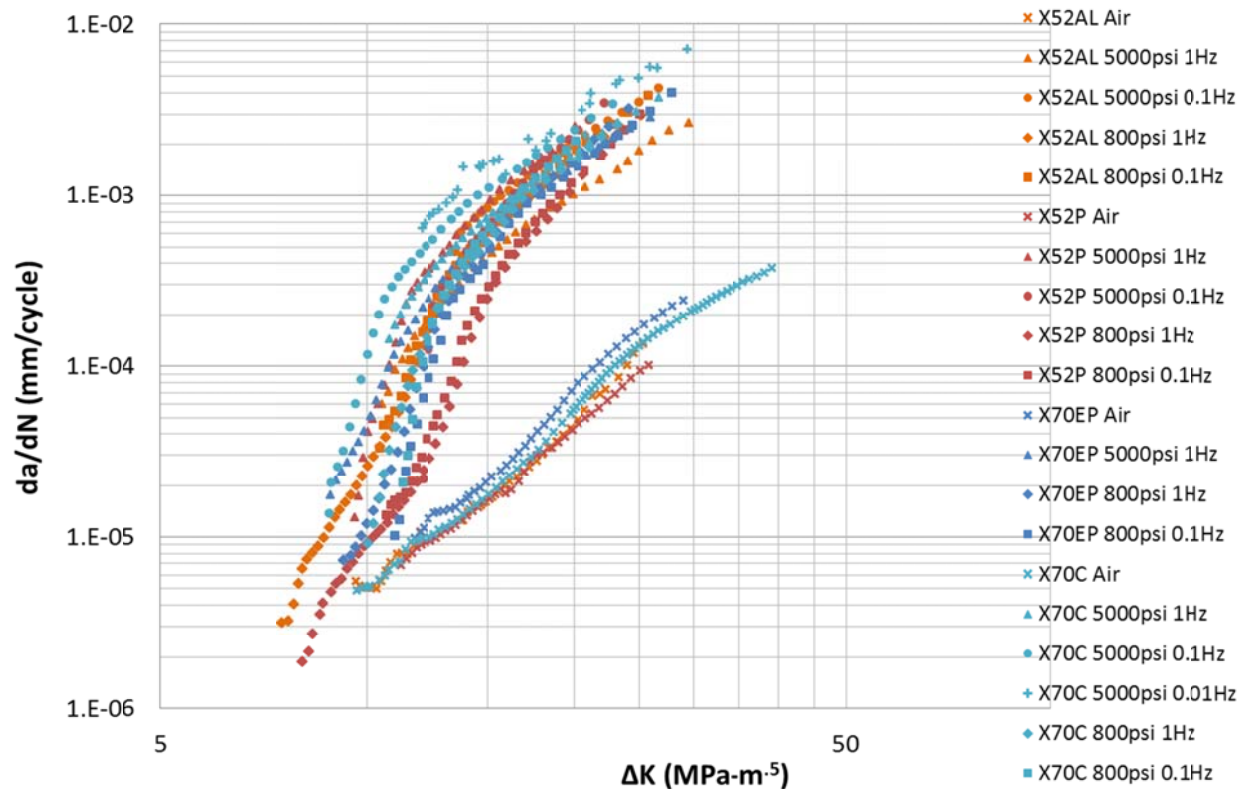
Figure 5-20 Comparison of representative data for all X52 and X70 steels for all test conditions

The last of the tests, including all materials, at a hydrogen pressure of 5.5 MPa and a frequency of 0.01 Hz are in the long chamber but have not yet finished. An additional test at a hydrogen pressure of 34 MPa and a frequency of 0.01 Hz is in the single chamber under cyclic loading. The material being tested is X52 from PG&E. It is also incomplete. The choice was made to keep the load range low to benefit the needs of ASME B31.12, rather than to apply a load range that will accelerate the crack growth, but will not provide necessary data at low ranges of stress intensity. This was decided following in-depth discussions with members of the B31.12 committee in February 2013. Update to the Final Report will be made with these data upon completion of the tests and analyses at no cost to DOT.

6 Modeling of Hydrogen Diffusion and its Correlation to Fatigue Crack Growth Rate

This section describes the stress-driven hydrogen diffusion model for fatigue crack growth in a gaseous high pressure hydrogen environment. The model's prediction and its correlation with fatigue test data are also presented in this section.

6.1 Overview of Modeling Approach

For a hydrogen-assisted fatigue cracking process in gaseous hydrogen environment, the hydrogen damaging sequence is depicted in Figure 6-1. Atomic hydrogen is produced by dissociative chemical adsorption for H_2 by chemical reactions for gaseous hydrogen. Once produced, the hydrogen atoms enter the metal at the highly stressed, occluded crack tip surface and diffuse ahead of the crack tip into the fracture process zone.
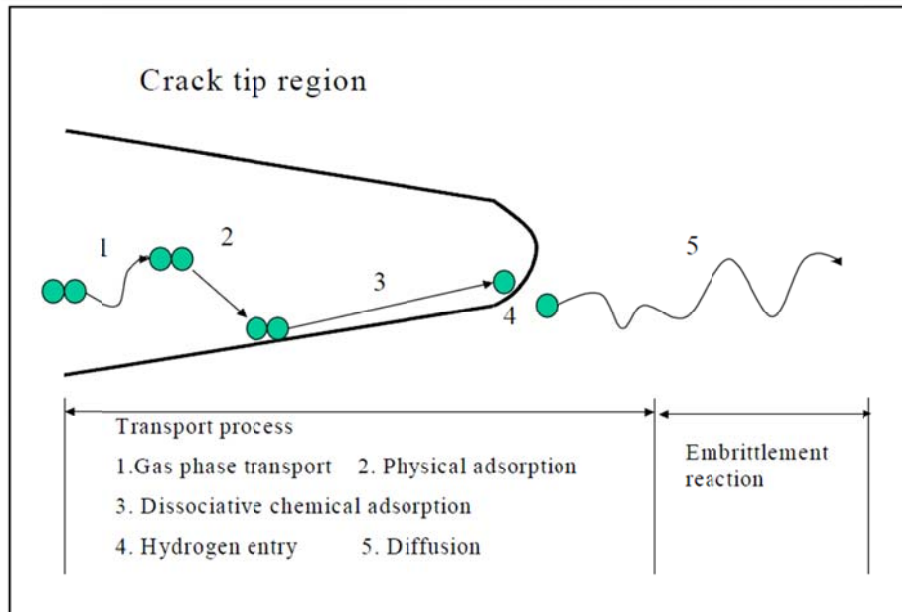
Figure 6-1 Hydrogen absorption and diffusion process during fatigue crack growth in alloys exposed to hydrogen gas [60]

By the idea of DEHE mechanism, a basic assumption is that the transient HA-FCG results from crack extension per cycle within the region of high hydrostatic stress in front of the crack tip. This region is characterized by a critical distance from the crack tip, χ_{CRIT}, at which the hydrogen concentration reaches a critical value C_{CRIT}.

In order to evaluate the critical distance, χ_{CRIT}, the hydrogen concentration profile in front of the crack tip needs to be determined. Since hydrogen diffusion around the crack tip is driven

mainly by the high hydrostatic stress produced by the cyclic load, the crack tip stress field must be solved for first. For this reason, our solution procedure for the hydrogen concentration profile includes the following components:

1. The crack tip stress field;

2. The evaluation of accumulation of hydrogen concentration at the crack tip surface;

3. The transient and quasi-steady state profiles of hydrogen concentration around the crack tip for a continuously moving fatigue crack; and finally

4. The evaluation of χ_{CRIT} and determination of hydrogen enhanced fatigue crack growth rate.

Realizing the complexity of the problem, several basic assumptions need to be made for the solution procedure:

1. The crack tip stress and hydrogen concentration profile are considered to be one dimensional;

2. The fatigue crack growth is considered to be a continuous process, within a load cycle, at a speed of the fatigue crack growth rate, as shown in Figure 6-2;

3. The stress field around the crack tip, as a compact tension specimen, is under the plane strain state;

4. Atomic hydrogen only enters into the steels at the crack tip surface where the hydrostatic stress is highly localized, cracking surface is fresh and occluded; and

5. The HA-FCG process is under constant room temperature; therefore, temperature dependency is not considered for the current modeling work.
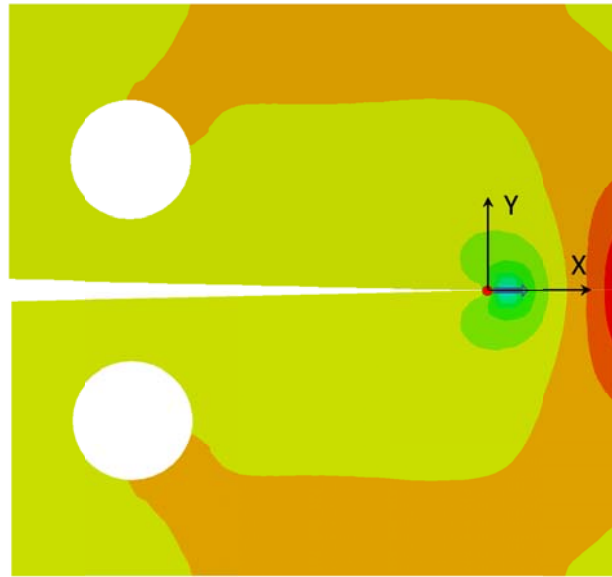
Figure 6-2 Hydrostatic stress field around a fatigue crack for a compact tension specimen. The crack tip is assumed to be continuously advancing.

6.2   Solution Components and Procedure

The entire kinetics model presented here includes the following parts:

1.   Crack tip mechanics to determine the hydrostatic stress field;

2.   The hydrogen concentration evaluation at the crack tip surface where enrichment of atomic hydrogen takes place due to high hydrostatic stress and plasticity;

3.   Solution of the hydrogen diffusion within the fracture process zone; and

4.   The evaluation of the critical hydrogen damaging distance χ_{CRIT}, given the hydrogen concentration distribution from step 3.

In the next several subsections, each of the solution components will be described.

6.2.1   Crack Tip Stress

The hydrostatic stress is determined using the crack-tip stress solution for plane strain state:

$$\sigma_h = \frac{2}{3}(1 + \nu)\frac{K}{\sqrt{2\pi x}} \qquad\qquad \text{Eq. 6.1}$$

where K is the stress intensity factor and ν is the Poisson ratio.

The plasticity zone size R_p is estimated using the following equation:

$$R_p = \frac{K^2}{6\pi\sigma_{YS}^2} \qquad\qquad \text{Eq. 6.2}$$

where σ_{YS} is the yield strength of the material. The plasticity zone size R_p will be used later in the evaluation of hydrogen concentration at the crack tip surface.

6.2.2 Sievert's Law and Hydrogen Concentration at Crack Tip Surface

For steels exposed to a gaseous hydrogen environment, the equilibrium lattice hydrogen concentration C_L in the stress-free steels is governed by Sievert's law:

$$C_L = kP^{\frac{1}{2}} \qquad \text{Eq. 6.3}$$

where P is the pressure of the gaseous hydrogen environment, and k is a constant. Note that the temperature dependency of C_L is not included since we only consider the constant temperature situation.

The hydrogen concentration at the crack tip can be enriched by the hydrostatic stress produced by the cyclic load. The hydrogen enrichment at the crack tip is related to the hydrostatic stress σ_h as follows:

$$C_H = kP^{\frac{1}{2}}e^{\frac{V_H\sigma_h}{RT}} \qquad \text{Eq. 6.4}$$

where V_H is the mole volume of the atomic hydrogen, R the ideal gas constant, and T the absolute temperature. Eq. 6.4 constitutes the hydrogen concentration at the crack tip surface, i.e., at $x = 0$ according the coordinate system shown in Figure 6-2.

Note that the hydrogen trapping effect is not considered directly as in Eq. 6.4, although the effective hydrogen diffusivity, which includes the contribution of hydrogen trapping, will be used in the solving of the hydrogen diffusion equation.

The constant k for Sievert's law, given by Eq. 6.3, varies in a large range depending on the material. Its absolute value is only for reference purposes in the solution. In the formulation, it is the dependence of C_H on hydrogen pressure and the local hydrostatic stress that matters.

For a cyclically loaded crack, the stress intensity factor range ΔK, the maximum and minimum stress intensity factors K_{max}, K_{min}, and load ratio R are related by the following:

$$K_{max} = (1 - R)\Delta K, \qquad K_{min} = RK_{max}$$

When a sinuous waveform is used for the cyclic load, the stress intensity factor is a function of time t within each load cycle:

$$K(t) = \frac{K_{max}+K_{min}}{2} + \Delta K cos(2\pi ft) \qquad \text{Eq. 6.5}$$

where f is the load frequency.

From Eq. 6.1, it is obvious that the hydrostatic stress σ_h at the crack tip surface $x = 0$ approaches infinity. To avoid this singularity, we characterize the hydrostatic stress σ_h at $x = 0$ by setting $\sigma_h = \sigma_{YS}$ at $x = R_P$ in Eq. 6.2. Then the time-dependent hydrostatic stress at crack tip surface follows in a similar fashion to Eq. 6.5:

$$\sigma_h(t) = \frac{\sigma_{max}+\sigma_{min}}{2} + \Delta\sigma_h cos(2\pi ft) \qquad \text{Eq. 6.6}$$

with $\sigma_{max} = \frac{2}{3}(1+\nu)\frac{K_{max}}{\sqrt{2\pi R_P}}$, $\sigma_{min} = \frac{2}{3}(1+\nu)\frac{K_{min}}{\sqrt{2\pi R_P}}$, and $\Delta\sigma_h = \sigma_{max} - \sigma_{min}$.

If local equilibrium of hydrogen concentration at the crack tip surface with the gaseous hydrogen environment can be reached instantaneously, substituting Eq. 6.6 into Eq. 6.4 leads to the following:

$$C_H(t) = kP^{\frac{1}{2}}e^{\frac{V_H\sigma_h(t)}{RT}}.$$

This expression, although not exactly similar to the sinuous form of Eq. 6.6, can be approximated with a sinuous format:

$$C_H(t) = C_{Havg} + \Delta C_H cos(2\pi ft) \qquad\qquad \text{Eq. 6.7}$$

with

$$C_{Havg} = \frac{C_{Hmax} + C_{Hmin}}{2},$$

$$\Delta C_H = C_{Hmax} - C_{Hmin},$$

$$C_{Hmax} = kP^{\frac{1}{2}}e^{\frac{V_H\sigma_{max}}{RT}}, \text{ and}$$

$$C_{Hmin} = kP^{\frac{1}{2}}e^{\frac{V_H\sigma_{min}}{RT}}$$

Eq. 6.7 will serve as the boundary condition for the hydrogen diffusion problem. As seen from its derivation, the loading parameters such as peak stress intensity factor K_{max}, load ratio R, load frequency f, material's yield strength, and hydrogen gas pressure are captured in the formulation.

6.2.3   Solution of Hydrogen Diffusion Equation by Moving Source Method

This subsection presents the analytical solution of the hydrogen diffusion equation in the frame work of moving coordinate. Detailed analytical derivation can be found in the Appendix.

For a typical stress-driven hydrogen diffusion problem, the governing equation can be written as

$$\frac{\partial C}{\partial t} = \nabla(D\nabla C) + \nabla(\sigma_h C) \qquad\qquad \text{Eq. 6.8}$$

where D is the effective hydrogen diffusivity and C is the diffusible hydrogen concentration. For first order approximation, we drop the stress term and let the hydrostatic stress play its driving-force role as in the boundary condition Eq. 6.7.

By assuming that the crack tip is continuously moving at a speed of u ($u = \frac{da}{dt}$), in the moving coordinate that is attached to the crack tip (as shown in Figure 6-2), after dropping the stress term, Eq. 6.7 becomes:

$$\frac{\partial C}{\partial t} - u\frac{\partial C}{\partial x} = \nabla(D\nabla C) \qquad\qquad \text{Eq. 6.9}$$

Using the analytical solution technique similar to the moving line-source solution in heat conduction [61], the general form of the solution of Eq. 6.9 with a boundary condition Eq. 6.7 can be derived as:

$$C(x,t) = \beta \, e^{-\frac{ux}{2D}} [C_{avg}(t) + C_{osc}(t)]$$

Eq. 6.10

where β is a constant. The transient solution consists of two parts, each responds to the constant averaged hydrogen concentration boundary condition C_{Havg}, and the oscillating hydrogen concentration boundary condition ΔC_H as follows:

$$C_{avg}(x,t) = C_{Havg}\left[K_o\left(\frac{ux}{2D}\right) - \int_0^{\frac{x^2}{4Dt}} \frac{d\xi}{2\xi}\left(\exp\left(-\xi - \frac{1}{4\xi}\left(\frac{ux}{2D}\right)^2\right)\right)\right]$$

Eq. 6.11

$$C_{osc}(x,t) = \Delta C_H\left[\int_{\frac{x^2}{4Dt}}^{\infty} \cos\left(2\pi f\left(t - \frac{x^2}{4D\xi}\right)\right)\frac{d\xi}{2\xi}\left(\exp\left(-\omega - \frac{1}{4\xi}\left(\frac{ux}{2D}\right)^2\right)\right)\right]$$

Eq. 6.12

where K_o is the modified Bessel function of second kind and zero order.

After a long enough time, as $t \to \infty$, the transient parts approach zero for both responses. For the response to the averaged hydrogen boundary condition, Eq. 6.11 becomes

$$C_{avg}(x) = C_{Havg}K_o\left(\frac{ux}{2D}\right).$$

And for the response to the oscillating hydrogen boundary condition, Eq. 6.12 becomes

$$C_{osc}(x,t) = \Delta C_H K_o\left(x\sqrt{\frac{\pi f}{D}}\right)\cos\left(2\pi ft - x\sqrt{\frac{\pi f}{D}}\right).$$

If we combine the two asymptotic parts together, the final solution for the "quasi-steady" state of the hydrogen concentration in front of the crack tip is:

$$C(x,t) = \beta \, e^{-\frac{ux}{2D}}\left[C_{Havg}K_o\left(\frac{ux}{2D}\right) + \Delta C_H K_o\left(x\sqrt{\frac{\pi f}{D}}\right)\cos\left(2\pi ft - x\sqrt{\frac{\pi f}{D}}\right)\right]$$

Eq. 6.13

6.2.4 Characteristics of the Hydrogen Concentration Solution

There are several interesting trends associated with the solution presented in the previous subsection worth discussing.

First, the governing equation and formulation for the hydrogen concentration at the crack tip are based on the assumption that the crack tip moves forward with a constant speed u. For a real fatigue crack, its growth rate (u) keeps accelerating as the stress intensity factor range increases. The solution procedure ignores the effect of crack growth acceleration in the real situation. Therefore, the solution is a first-order approximation.

Secondly, the crack growth speed u itself is an unknown in the formulation. With certain hypothesis for hydrogen-enhanced fatigue cracking in a load cycle, u can be determined through an iterative procedure when the quasi-steady state is reached, as to be seen later in this section.

Two important characteristics of the transient hydrogen concentration solution are examined in the next two subsections.

6.2.4.1 Attenuation of Hydrogen Concentration Oscillation

After reaching the "quasi-steady" state, the hydrogen concentration profile includes two parts. The first part is the response to the averaged boundary condition at the crack tip, C_{Havg}. It remains a fixed shape as the crack front moves forward; the second part, in response to the concentration oscillation at the crack tip, ΔC_H, oscillates with the same frequency as the cyclic load, but its oscillation amplitude attenuates from the crack tip surface according to a function of $K_o\left(x\sqrt{\dfrac{\pi f}{D}}\right)$. Since K_o is a rapid decreasing function of distance, it is obvious that higher load frequency or lower hydrogen diffusivity will make the attenuation steeper as the location moves away from the crack tip. Figure 6-3 plots the attenuation function of $K_o\left(x\sqrt{\dfrac{\pi f}{D}}\right)$ for $D = 2.68x10^{-11}$ m^2/s under different load frequencies. As frequency increases, the attenuation effect becomes more severe. For a load frequency of 1 Hz, for instance, the oscillation part of the hydrogen concentration at the crack tip is hardly felt beyond a distance of 6 μm.
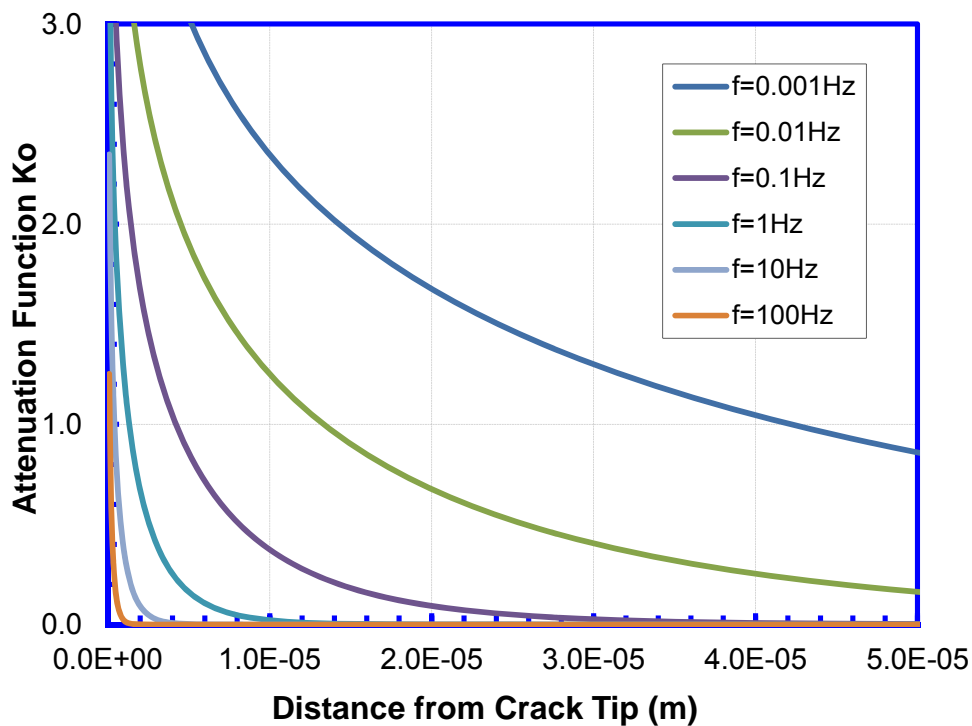

Figure 6-3 Attenuation of oscillating hydrogen concentration as function of distance from crack tip

From the derivation in the previous subsection, ΔC_H increases as peak stress intensity factor increases or load ratio decreases. For C_{Havg}, it increases as peak stress intensity factor increases or load ratio increases. These relations between C_{Havg}, ΔC_H and hydrogen pressure and loading conditions define the dependency of hydrogen-enhanced FCGR on process parameters.

6.2.4.2 Transition to "Quasi-steady" State Concentration Profile

The complete transient solution defined by Eqs. 6.10, 6.11, and 6.12 can be used to examine the transient behavior of the hydrogen concentration during a fatigue crack growth test. If load ratio is high or the oscillation part attenuates rather quickly because of high load frequency or low diffusivity, the oscillation part will be much smaller than the averaged part and can be dropped from the solution. In this case, the transient solution becomes:

$$C(x,t) = C_{Havg}\beta e^{-\frac{ux}{2D}}\left[K_o\left(\frac{ux}{2D}\right) - \int_0^{\frac{x^2}{4Dt}}\frac{d\omega}{2\omega}\left(\exp\left(-\omega - \frac{1}{4\omega}\left(\frac{ux}{2D}\right)^2\right)\right)\right] \qquad \text{Eq. 6.14}$$

The integral part inside the bracket in Eq. 6.14 represents the transient part. It approach zero as $t \to \infty$.

Suppose the material is initially at the lattice hydrogen concentration, a very low value for iron (10^{-4} wppm). Given the values of u and D, the transient period of Eq. 6.14 can be evaluated. When crack growth rate u is low, the time to reach the quasi-steady state is very long. For X52 pipeline steels, a typical value of hydrogen diffusivity is $D = 2.7 \times 10^{-11}$ m^2/s. Using this value, and $u = 1 \times 10^{-7}$ m/s, the hydrogen concentration profiles at different times are plotted in comparison against the quasi-steady state profile in Figure 6-4. It takes thousands of seconds for the hydrogen profile reaches the quasi-steady state. For an even slower crack growth rate $u = 1 \times 10^{-8}$ m/s, the time to reach quasi-steady is approximately 555 hours. If $u = 5 \times 10^{-6}$ m/s, however, the time to reach quasi-steady state is about 5 seconds, as shown in Figure 6-5. For an f = 1 Hz fatigue test, it only needs 5 cycles to reach quasi-steady state.
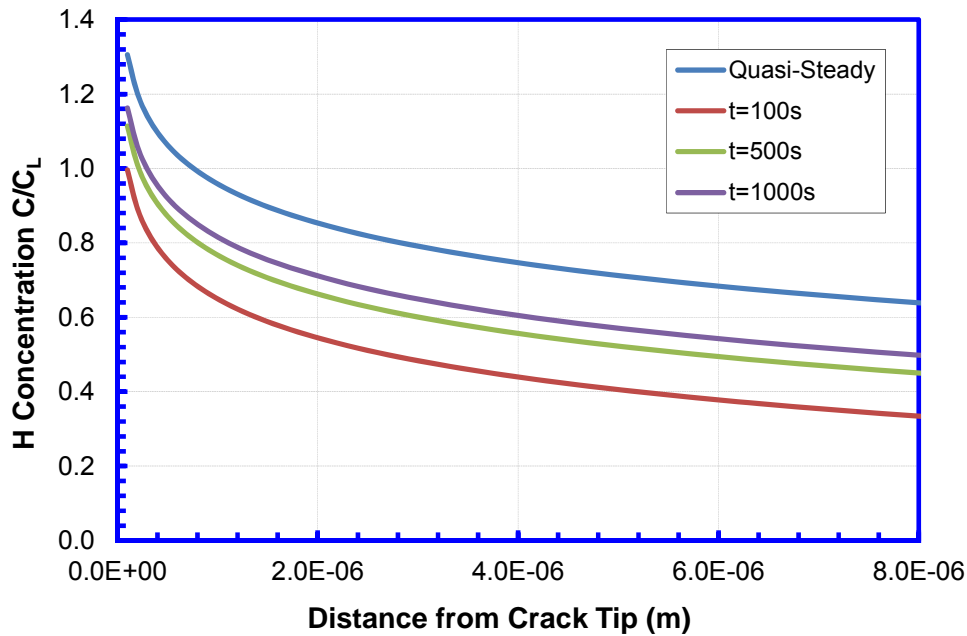
Figure 6-4 Slow transition of hydrogen concentration profile to "quasi-steady" state for low crack growth rate u=1x10^{-8} m/s
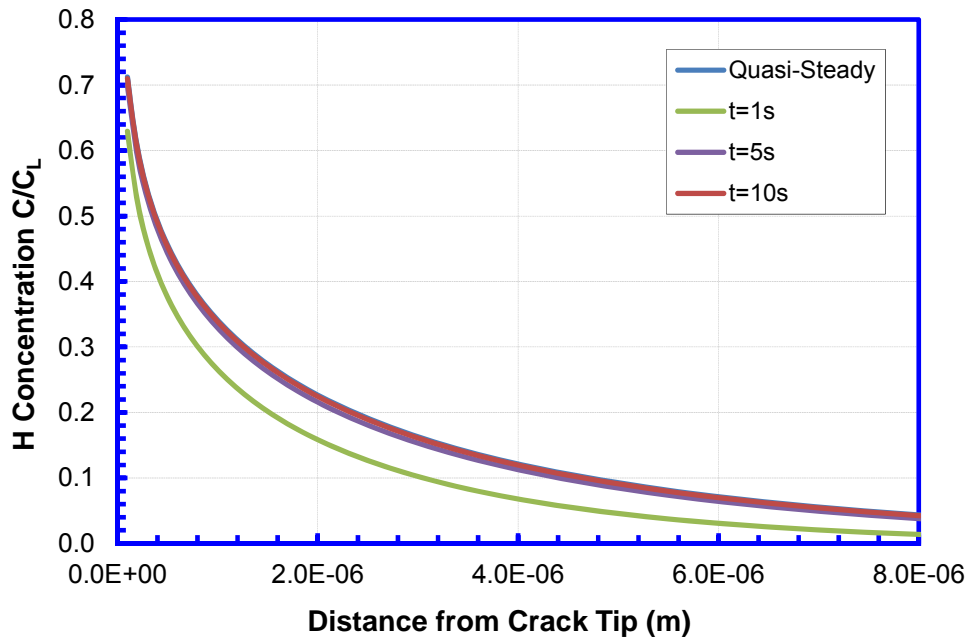
Figure 6-5 Fast transition of hydrogen concentration profile to "quasi-steady" state for low crack growth rate u=5x10^{-6} m/s

The above observations on two extreme situations have important implications to the hydrogen-enhanced fatigue crack growth. Figure 6-6 plots the HA-FCGR test results for the

CRC X70 pipeline steel. In-air FCGR data are also plotted for comparison reason. As expected, the in-air results follow the Paris law. For the HA-FCGR results, all curves appear to be consisted of two parts which are divided by a "threshold" point $\Delta K = 12$ MPam$^{0.5}$. In the first half, FCGR starts from low values and goes through a rapid climb. In the second half, the increase rate of FCGR becomes moderate before following a trend line parallel to the Paris-law line of the in-air data.

This phenomenon can be explained through the hydrogen diffusion solution presented above. As the crack starts from a low growth rate, according to the transient solution, it would take a very long time for the hydrogen concentration profile reaches its quasi-steady state. Because of the low growth rate (u), the hydrogen concentration "front" is able to overgrow the moving crack tip. The consequence is that the elevated level of hydrogen concentration in front of the crack tip enhances the crack growth. This increase of FCGR driven by hydrogen continues until that the hydrogen-enhanced crack growth is able to "catch up" the hydrogen concentration "front". This is when the HA-FCGR reaches its quasi-steady state. In real testing situations where a constant cyclic load level is applied, the HA-FCGR still grows in the quasi-steady state due to the increase of hydrogen concentration at the crack tip surface. This enrichment of hydrogen at the crack tip surface is caused by the increasing stress intensity factor.

Figure 6-6 Comparison in-air FCGR and HA-FCGR for X70 in 800psi hydrogen. For HA-FCGR, transient part and quasi-steady part are marked.

6.2.5 Determination of the Hydrogen-Enhanced Fatigue Crack Growth Rate

In the previous subsection, the quasi-steady state part of a HA-FCGR curve has been identified. And the hydrogen concentration profile in that part is governed by Eq. 6.13. To determine the HA-FCGR, we followed the approach by Gangloff and Wei [39,49] with the ass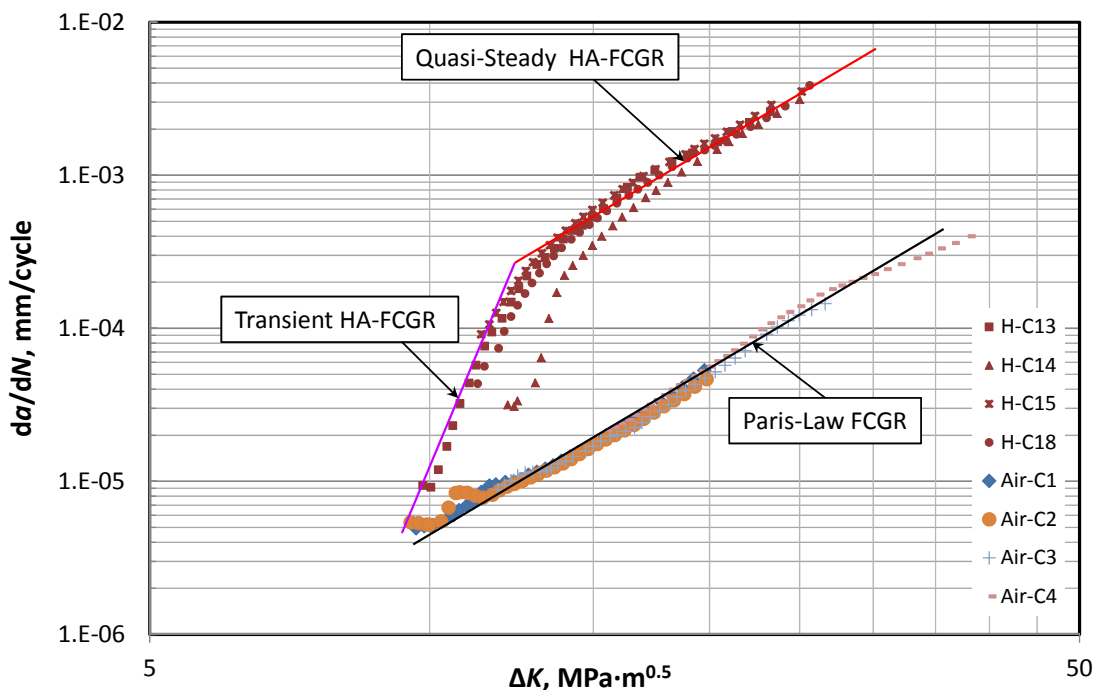umption that within each load cycle, hydrogen enhanced increment of crack growth occurs when the load reaches K_{max}, and the size of the increment is determined by a critical distance (from the current crack tip) at which a critical hydrogen concentration C_{CRIT}, is reached. In other words, the critical distance χ_{CRIT}, and the critical concentration C_{CRIT}, satisfy the following condition through Eq. 6.13:

$$C_{CRIT} = \beta \, e^{-\frac{u\chi_{CRIT}}{2D}} [C_{Havg} K_o \left(\frac{u\chi_{CRIT}}{2D}\right) + \Delta C_H K_o (\chi_{CRIT}\sqrt{\frac{\pi f}{D}})\cos(2\pi ft - \chi_{CRIT}\sqrt{\frac{\pi f}{D}})] \quad \text{Eq. 6.15}$$

In determining χ_{CRIT}, note that based on the assumption just described, $\frac{da}{dN} = \chi_{CRIT}$, and by definition, we have

$$u = \frac{da}{dt} = \frac{1}{T}\frac{da}{dN} \qquad\qquad \text{Eq. 6.16}$$

where T is the load period for each cycle.

The choice of C_{CRIT} was made in a ratio of C_{CRIT} to the equilibrium lattice hydrogen concentration C_L, which is pressure dependent. Similar to Gangloff's approach, a value of $\frac{C_{CRIT}}{C_L} = 20$ was used for the calculation.

Since the oscillation term is included in Eq. 6.15, its peak value during a whole cycle was used in the calculation of χ_{CRIT}

To summarize, the following pseudo iterative procedure was used to determine χ_{CRIT}:

1. Given hydrogen gas pressure, load information K_{max}, R, and the critical hydrogen concentration C_{CRIT}, is evaluated;

2. The hydrogen concentration at the crack tip surface enriched by hydrostatic stress is evaluated, this includes the average part C_{Havg}, and the oscillating part ΔC_H;

3. Given the load frequency f, assume an initial value of u and solve Eq. 6.15 for χ_{CRIT};

4. Check if the newly evaluated χ_{CRIT} and assumed u satisfying the relation defined by Eq. 6.16 and, if not, update the u value using Eq. 6.16 and return to step 2;

5. Repeat the iterative process until Eq. 6.16 is satisfied.

The calculation procedure described above was implemented in a C++ computer program with a Windows® interface for the ease of calculation. Figure 6-7 shows the dialog-based Windows® program's interface. The interface allows the inputs of steel's diffusivity, yield strength, stress intensity factor, hydrogen pressure, load frequency and load ratio. Upon

clicking the "Calculate" button, the program goes through the iterative algorithm described in this subsection and displays the HA-FCGR results predicted by the model.

Figure 6-7 Windows® interface for the calculation of HA-FCGR

6.3   Correlation of Loading Parameters to Hydrogen Enhancement of Fatigue Crack Growth Rate

This section presents the predicted results by the diffusion model and its correlation with the measured HA-FCG data.

6.3.1   Material Properties in the Model

From Eq. 6.15 and the solution procedure described in Section 6.2.5, there are several key material properties in the determination of HA-FCGR.

The first and most important parameter is the steel's hydrogen diffusivity, D. Unfortunately, for typical C-Mn ferritic pipeline steels, large range of variations in their hydrogen diffusivity have been reported [62]. For similar steels, experimentally measured hydrogen diffusivities through hydrogen permeation can differ by one order or even higher. This is not a surprise since hydrogen diffusivity is highly sensitive to alloys' grain structure, grain boundary impurity, and dislocations where large amount of hydrogen can be trapped. By inference, the two X52 pipeline materials could possibly have very different diffusivity values because of the difference in their alloying compositions and microstructure as presented in Section 4.1.1.

Other material properties include the yield strength, σ_{YS}, mole volume of hydrogen in steels, V_H , and the lattice hydrogen concentration, C_L. Table 6-1 lists the values employed in the model and the relevant references.

Table 6-1 Material Properties in HA-FCGR Calculation

Material Properties	Value and Units	Reference
D for X52	$2.68 \times 10^{-7} \mathrm{cm}^2/\mathrm{s}$	[62]
D for X70	$7.5 \times 10^{-7} \mathrm{cm}^2/\mathrm{s}$	[63]
Yield Strength σ_{YS}	Per Table 4-1 (MPa)	This report
Mole Volume of H	2.0×10^{-6} m^3/mol	[74]
Lattice Hydrogen Concentration C$_L$	$C_L = 42.7 P_H^{0.5} e^{-\frac{3280}{T}}$, ppm	[64]

6.3.2   Prediction and Correlation of Hydrogen Enhanced Fatigue Crack Growth Rate

The dependency of HA-FACG on steels' hydrogen diffusivity has been recognized by Gangloff and others (See Figure 3-1). The calculated diffusivity dependency of HA-FCGR is plotted in Figure 6-8. The calculated results were based on an X52 yield strength of 52 ksi, load frequency of 1Hz, load ratio of 0.5 and hydrogen pressure of 5.5 MPa(800 psi). The trend is in agreement with the measured results summarized in Figure 3-1.

To show the influence of yield strength on HA-FCGR, Figure 6-9 plots the measured HA-FCGR for the new and old X52 against the predicted values. From Table 4-1, the old X52 steel has a yield strength of 325 MPa (47.6 ksi) and the new X52 steel has a yield strength of 487 MPa (70.6 ksi). These actual strengths of the two steels were used in the HA-FCGR prediction calculations. As can be seen from the plot, the model was able to predict the trend that the HA-FCGR increases as the yield strength increases. But the model significantly over-predicted the HA-FCGR of the new X52. The likely reason was the value of diffusivity used in the calculations. For both steels, the same value of D, $2.68 \times 10^{-7} \mathrm{cm}^2/\mathrm{s}$, were used. Considering that the new X52's microstructure has a refined grain structure, its hydrogen diffusivity is likely lower than the old X52.
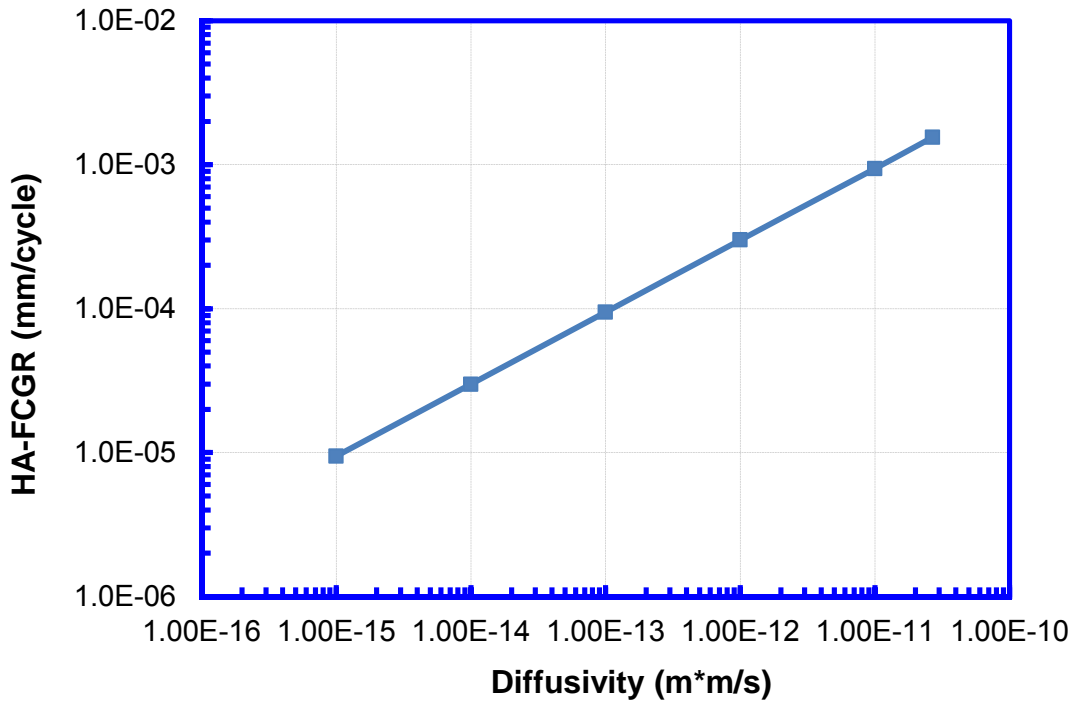
Figure 6-8 HA-FCGR dependency on hydrogen diffusivity
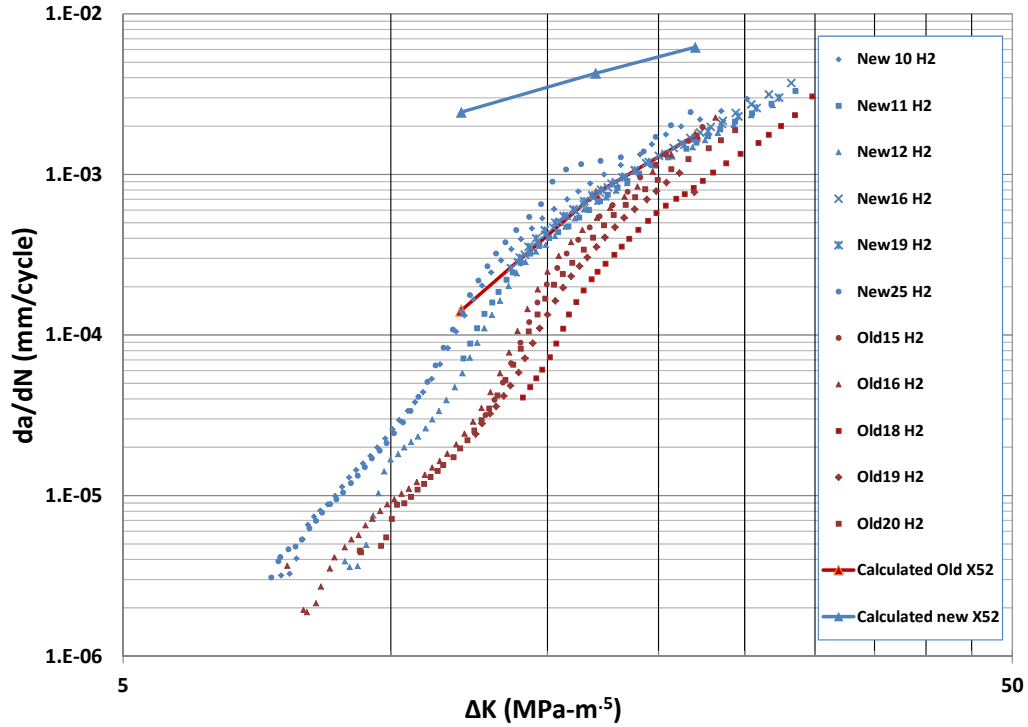
Figure 6-9 comparison of measured HA-FCGR for two X52 steels and the model predictions

Figure 6-10 plots the HA-FCGR test results for the old X52 steel under two different pressures of the hydrogen gas, and the calculated HA-FCGR. The model was able to correctly capture the dependency of HA-FCGR on hydrogen pressure with reasonable accuracy. The same hydrogen diffusivity value as the results in Figure 6-9 was used in the calculation.
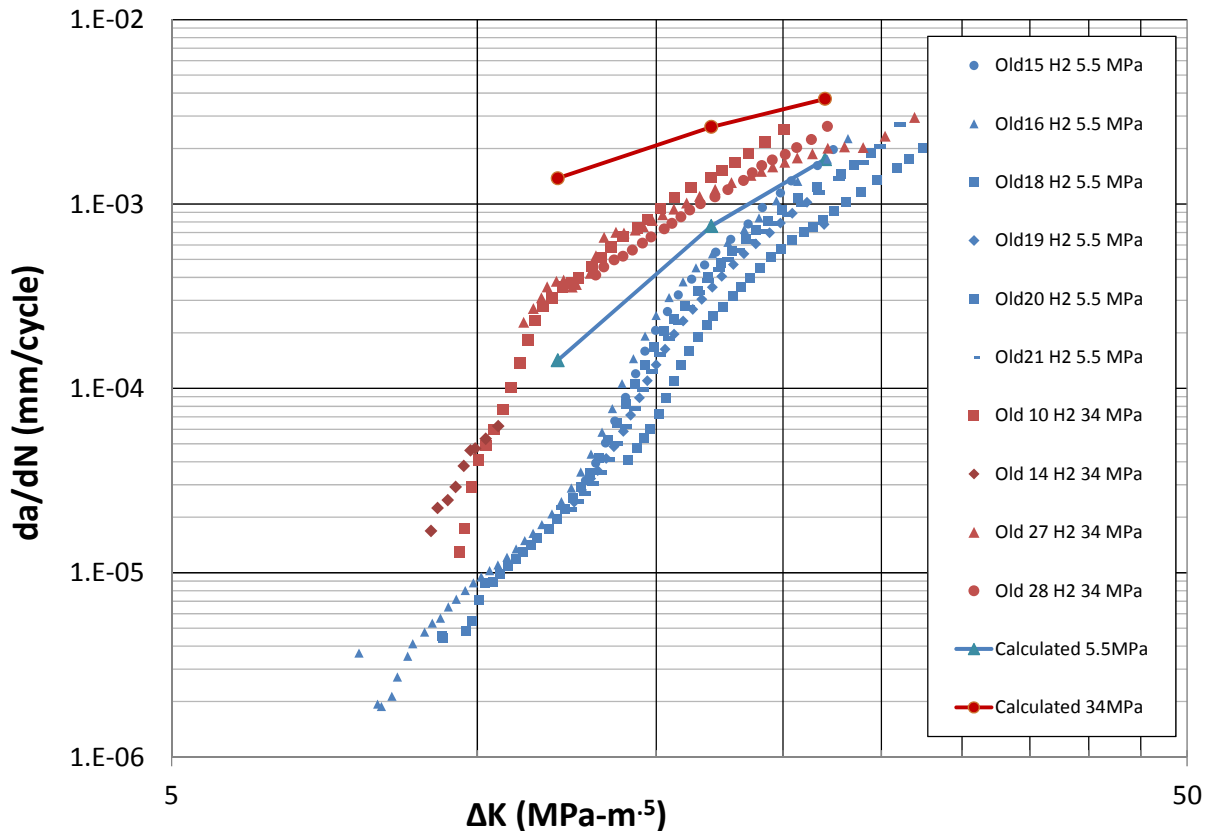
Figure 6-10 HA-FCGR dependency on pressure of hydrogen gas for the old X52 steel

Figure 6-11 demonstrates the effect of load frequency on HA-FCGR for the X70 steels. The calculated HA-FCGR under three load frequencies, 1 Hz, 0.1 Hz, and 0.01 Hz, are also plotted in comparison to the tested results. The same value of hydrogen diffusivity as that for the X52 steels It correctly captures the trend of increasing HA-FCGR as the load frequency decreases. As seen from the comparison, however, the calculation significantly over-predicted the HA-FCGR. Furthermore, for all the three load frequencies, the predicted HA-FCGR increases not as quickly as the tested values as the stress intensity factor range is increased. This poor performance by the model could be attributed to the strain-hardening behavior of the materials at the crack tip in the model, since the hardening behavior was formulated in the model in such a way that it strongly affects the hydrostatic stress at the crack tip, and consequently the hydrogen concentration there. Other likely causes include the choice of hydrogen diffusivity value. As

Gangloff and others have shown that the strain-stress behavior at the crack tip is critical for any mechanistic model of hydrogen embrittlement, improvement to the current diffusion model can be made if better knowledge on this matter becomes available. It is worth repeating that like any other mechanistic model of hydrogen embrittlement, an accurate knowledge of hydrogen diffusivity is critical to the current model. Unfortunately, reliable and consistent data on hydrogen diffusivity for the materials considered here is still lacking.
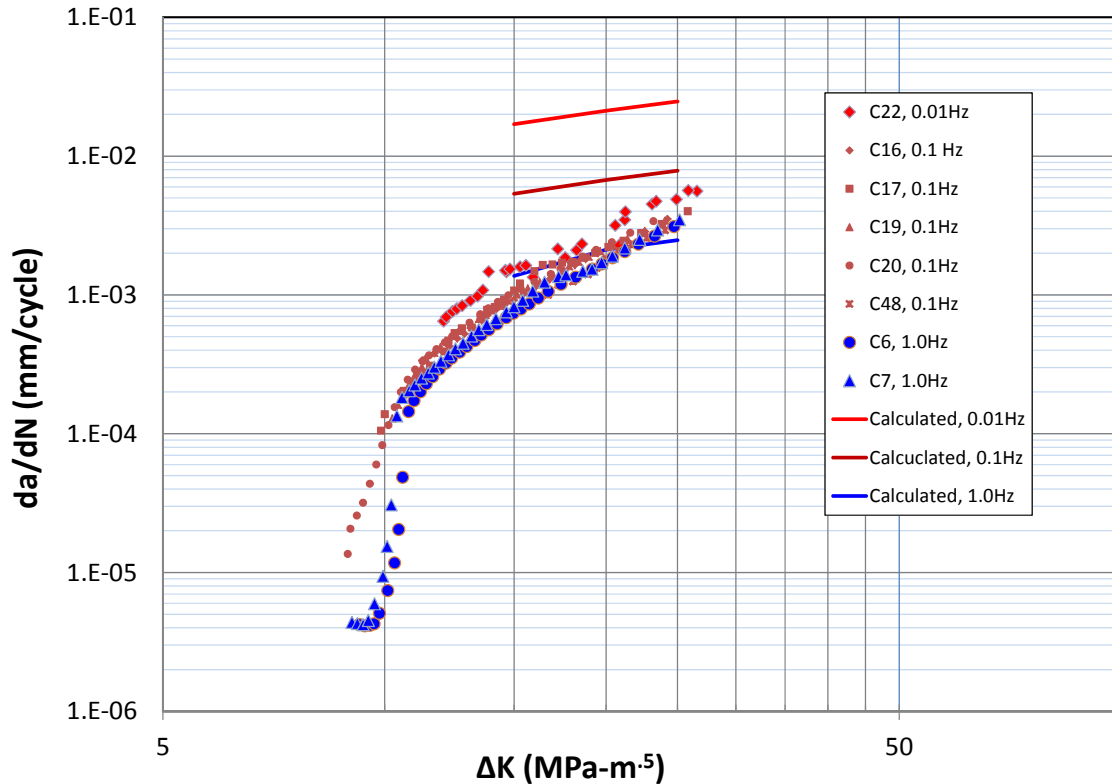
Figure 6-11 HA-FCGR dependency on load frequency for the new X70 steel

In summary, the hydrogen diffusion model developed in the current project presents a new point of view on the HA-FCGR phenomenon and is able to explain the transient nature of the measured HA-FCGR curves. It can also predict the trend of HA-FCGR as a function of hydrogen pressure, load frequency, and material strength. Its accuracy in predicting the HA-FCGR can be improved if more accurate and consistent hydrogen diffusivity data are available. Additionally, other mechanisms, such as an improved strain-hardening sub-model at the crack tip and hydrogen-trapping, could improve the current model.

7 Modeling of Fatigue Crack Growth Rate in Hydrogen

7.1   Introduction

Experimental results indicate that fatigue crack growth rates (FCGR) of metals in high-pressure hydrogen increase with increasing hydrogen pressure [2,11,14,54,56,65,66,67]. The equilibrium, non-stressed, hydrogen concentration in metal is given by

$$[H]_0 = \frac{\emptyset}{D}(P_H)^m = A(P_H)^m \exp\left(-Q/RT\right),$$ Eq. 7.1

where $[H]_0$ is the stress-free, equilibrium hydrogen concentration in the metal; $\emptyset$ is the coefficient of hydrogen permeation; D is the coefficient of hydrogen diffusion; A is a constant; P_H is the hydrogen pressure; Q is activation energy; R the universal gas constant and T is the absolute temperature [68,69]. Sievert's law, which relates the steady-state, non-stressed, subsurface, atomic gas concentration in a solid to the pressure of the diatomic gas near the surface, predicts a pressure exponent value of $m = 1/2$. However, the value of m may vary as a function of temperature [70] and the rate-limiting step for hydrogen transport [71]. Pressure dependence has been shown to vary from sub-parabolic ($m < 1/2$) [4] to an exponential dependence with $m > 1$ [70], depending upon material and conditions. At higher hydrogen pressures the pressure term in Eq. 7.1 is replaced with the fugacity, fu, as determined by

$$fu = P\exp\left(Pb/RT\right),$$ Eq. 7.2

where P is the pressure, b=15.84 cm^3/mol. The stress-assisted hydrogen concentration has been shown to follow [72]

$$[H]_\sigma = [H]_0 \exp\left(\sigma_h v/RT\right),$$ Eq. 7.3

where $[H]_\sigma$ is the stress-assisted hydrogen concentration, σ_h is the hydrostatic stress, $V = 2.0 \times 10^{-6}$ m^3/mol [73,74,75,76] is the partial molar volume of hydrogen in the metal and all other constants are as defined above. The stress tensor as a function of distance from the crack tip is required in order to determine σ_h. Given that the value of the stress tensor is location-specific with respect to the crack tip, the stress-assisted hydrogen concentration will also be location-specific as well. Previous work on API-5L X80 pipeline steel [73] used the Hutchinson, Rice, Rosengren (HRR) model [77,78] to determine the stress field in the FPZ. The HRR model predicts the stress distribution in front of a sharp crack of a strain-hardening material in polar coordinates (r and θ). It is given by

$$\sigma_{ij} = \sigma_0 \left[\frac{EJ}{\alpha \sigma_0^2 I_n r}\right]^{1/n+1} \tilde{\sigma}_{ij}(n, \theta),$$ Eq. 7.4

where σ_0 is the material yield strength, E the modulus of elasticity, J the value of the J-contour integral, α a dimensionless constant, r the distance in front of the crack tip, n the work hardening

exponent from the Ramberg-Osgood equation for fitting stress-strain data in uniaxial tests, $\tilde{\sigma}_{ij}$ a dimensionless function of n and θ, and I_n an integration constant that depends upon n and $\tilde{\sigma}_{ij}$. The J-integral may be replaced by K_I^2/E for a globally linear elastic material [79], where K is the stress intensity factor. The hydrostatic stress can then be determined via

$$\sigma_h = \frac{1}{3}\sigma_{ii}.$$ Eq. 7.5

The use of Eq. 7.3, in conjunction with Eqs. 7.4 and 7.5, effectively provides an estimate of the hydrogen concentration in the FPZ as a function of distance r, and angle θ. The key, therefore, is to solve for the stress-assisted hydrogen concentration at some critical distance of interest. If one assumes blunting of the crack tip, the location at which the maximum crack-opening stress occurs may be solved as [80]

$$X_{\sigma\_max} = \frac{K^2}{\sigma_0 E},$$ Eq. 7.6

where all constants are defined above. Eq. 6 was determined via finite element large-scale plasticity analysis in the absence of gaseous hydrogen, which will likely affect dislocation dynamics in the FPZ. Values for X_{σ_max} vary between 4 μm and 48 μm, depending upon the material [71]. Using an estimate for the plastic zone size,

$$r = \frac{1}{\pi}\left(\frac{K_I}{\sigma_0}\right)^2,$$ Eq. 7.7

may also be appropriate estimate for the critical distance in Eq. 7.4 as this value defines the extent of the stress-assisted hydrogen accumulation in front of the crack tip.

It has been shown empirically that FCGRs follow a multiplicative relationship between FCG driving force ΔK and a deleterious diffusion process (potentially stress-assisted) in oxidizing environments [81,82,83,84,85,86,87,88,89], temperature-assisted viscoplastic deformation [90], as well as materials tested in hydrogen [25, 28,91], such that

$$\frac{da}{dN} = A \cdot \Delta K^n \cdot F(env)$$ Eq. 7.8

where A and n are material specific constants, and $F(env)$ is a term relating the diffusion kinetics of the deleterious environmental interaction. Models of similar functional form have been proposed for FCGR in hydrogen gas assuming hydrogen environment assisted cracking, some of which are compiled in [22].

Typically there are two primary approaches to phenomenological modeling of multiple, concurrently occurring, damage mechanisms. The first approach is the linear summation model [92,93], which presumes that each increment of crack growth is a summation of the crack growth from independently occurring, non-interacting mechanisms. The model is as follows for FCG applications:

$$\frac{da}{dN}_{\text{Total}} = \sum \frac{da}{dN_i},$$

<div align="right">Eq. 7.9</div>

where the subscript i refers to any number of independent mechanisms. The second approach is the cumulative damage model, which presumes that multiple concurrent damage mechanisms "compete" with one another, such that any single mechanism may dominate total deformation, or the total deformation may result from an interaction of multiple mechanisms. The general framework for the cumulative damage model,

$$D_{\text{Total}} = \sum D_i,$$

<div align="right">Eq. 7.10</div>

states that the total damage from all competing mechanisms D_{TOTAL} is equal to the summation of each damage mechanism D_i as if they were occurring independently. When applied to life prediction, the cumulative damage model becomes

$$N_f = [D_{\text{Total}}]^{-1} = \left[(N_{f1})^{-1} + (N_{f2})^{-1} \right]^{-1},$$

<div align="right">Eq. 7.11</div>

where N_f is the predicted number of cycles to failure and N_{f1} and N_{f2} are the number of cycles to failure for two isolated damage mechanisms [94]. Underlying this model is the notion that material separation (failure) occurs at a total damage equal to one [94]. Whereas the linear summation model treats the deformation mechanisms as if they occur in parallel, the cumulative damage model presumes that the independent deformation mechanisms occur in series, in which case the cumulative effect may incorporate damage mechanism interactions.

Competing damage mechanisms can lead to fatigue crack propagation behavior that deviates from Paris Law behavior. Fatigue crack growth of pipeline steels in gaseous hydrogen generally exhibits a bilinear trend in the Paris region. Two classic examples of *da/dN vs. ΔK* results yielding bilinear trends are the transition from microstructurally small crack growth (in most alloys) and FCG of Ti-6Al-4V in air [95]. The former is due to the interplay of the fatigue crack extension per cycle and the material grain size, while the latter was found to be correlated to the interaction between fatigue crack extension per cycle and the Widmanstatten packet size, which refers to a substructure of a grain where precipitates or a second phase form along certain crystallographic planes and can be thought of as an effective grain size in Ti alloys [95,96]. However, the bilinear trend observed in FCG in the presence of hydrogen is clearly in the long crack regime and beyond the region where crack propagation is affected by the microstructural features of the particular materials tested here. Research has shown that the fatigue crack surface exhibits different morphologies depending on the region of FCG [50,65,75,96]. It has been shown that FCG may take the form of mixed-mode fracture, intergranular fracture with branching, intergranular fracture leading to dimple rupture, or intergranular stress corrosion fatigue [50].

7.2   Model Development

Based upon the experimental results, microscopy, and the literature regarding FCG in hydrogen, it is presumed that the transient hydrogen-assisted fatigue crack growth (HA-FCG) occurs as a result of per-cycle crack extension, which occurs within the FPZ most affected by the stress-assisted hydrogen concentration (Eq. 7.3). A predominantly intergranular crack path results. Furthermore, it is presumed that the steady-state HA-FCG occurs due to the per-cycle crack extension that exceeds the stress-assisted hydrogen concentration region by some amount. This reduces the hydrogen interaction to the order of Eq. 7.1, resulting in a primarily trans-granular fracture surface. The size interactions of the crack extension and the FPZ are shown schematically in Figure 7-1.

(a)   (b)
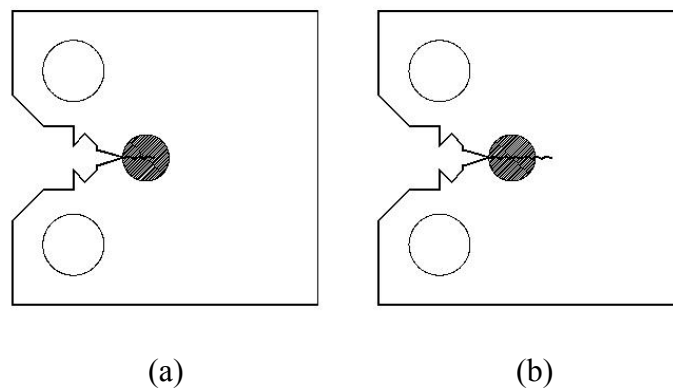
Figure 7-1 Sketch depicting conditions in which (a) transient HA crack growth would occur, and (b) steady-state HA crack growth would occur. Transient HA-FCG occurs when the crack extension *per cycle* remains within the FPZ created by the previous cycle, whereas transient FCG occurs then the crack extension *per cycle* extends beyond the FPZ. The FPZ is shown as a shaded region. Sizes are exaggerated for clarity.

The transition between the two regimes is defined by a "knee point" on the da/dN versus ΔK plot, occurring at da/dN_{tr} of X_{tr}/cycle. The experimental results collected to date suggest that da/dN_{tr} occurs at

$$da/dN_{tr} = 2 \cdot 10^{-6} \Delta K^2.$$
<div align="right">Eq. 7.12</div>

The results of Eq. 7.12 are identical to the second-order estimate of the Irwin plastic zone size (Eq. 7.7) for X100 and are proportional to the plastic zone size for X70 and X52.

The preceding discussion lays out a framework for understanding the segregation of dominant damage mechanisms occurring in HA-FCG. Specifically, at $da/dN < da/dN_{tr}$, the FCGR is dominated by the stress-assisted hydrogen concentration or dependent predominantly on P_H; for $da/dN > da/dN_{tr}$, the FCGR is affected by the far-field hydrogen concentration and is therefore presumed to be dominated primarily by ΔK.

If one assumes that an incremental extension of the crack tip due to HA-FCG comprises a pure fatigue component and an environmental-fatigue (HA) component, the FCGR relationship would then have the following functional form:

$$\frac{da}{dN_{total}} = \frac{da}{dN_{fatigue}} + \frac{da}{dN_H},$$ Eq. 7.13

where the subscripts *fatigue* and *H* designate contributions to the total crack advance due to fatigue only and HA fatigue, respectively. The general framework of FCG superposition has been successfully employed to correlate data on environmental-fatigue crack growth in oxidizing environments [83,89], corrosive environments [97], high-temperature environments inducing viscoplastic deformation [89,98], thermo-mechanical fatigue [82], and crack advance segregated by microstructural considerations [83], to name just a few. One should note that Eq. 13 is proposed to correlate region II crack growth only, as it is believed that the data presented here falls within this regime. The first term of Eq. 7.13 is given by the traditional Paris relationship

$$\frac{da}{dN_{fatigue}} = A\Delta K^b,$$ Eq. 7.14

where *ΔK* is the driving force for crack extension defined in ASTM E647 [6] and *A* and *b* are constants fitted to the experimental data. Eq. 7.14 accounts for the fatigue-only contribution of crack extension, regardless of test environment. As such, Eq. 7.13 must collapse to Eq. 7.14 for tests performed in air.

Based upon the presumed underlying deformation mechanisms and the previous work performed on the kinetics of environmental fatigue [81,83,84,87,88,89,90, 99,100], one might expect that the functional form for a HA-FCGR relationship would follow

$$\frac{da}{dN_H} = F[a\Delta K^B[H]] = F\left[a\Delta K^B P_H^m \exp\left(-Q + \sigma_h v \Big/ RT\right)\right],$$ Eq. 7.15

where *F* indicates "a function of" and all parameters are defined above. Inherent to the functional form of Eq. 7.15 is the presumption that an increased hydrogen concentration within the material would enhance FCG. Though one may readily accept this notion due to the experimental results presented in the literature, the multiplicative nature of this interaction as proposed in Eq. 7.15 is purely empirical, as a thorough understanding of the deformation mechanisms and their interactions occurring during HA-FCG is still lacking. The term P_H^m incorporates the ambient hydrogen pressure and accounts for the steady-state concentration [*H*] of hydrogen within the steel. The exponential term $\exp\left(-Q + \sigma_h v \Big/ RT\right)$ accounts for the kinetics of hydrogen transport via an Arrhenius relationship, as well as the contribution of lattice dilatation due to the hydrostatic stress.

Due to the presumption of the segregation of the dominant damage mechanisms occurring in HA-FCG, a relationship similar to that of linear damage summation is proposed. Specifically, it is assumed that the FCG driven by the hydrogen pressure occurs in series with the *ΔK*-assisted FCG, thereby setting up a competition between the two mechanisms. Following the derivation of Eq. 7.11, the HA-FCGR is given by

$$\frac{da}{dN_H} = \left[\left(\frac{da}{dN_{P_H}}\right)^{-1} + \left(\frac{da}{dN_{\Delta K}}\right)^{-1}\right]^{-1},$$ Eq. 7.16

where $\frac{da}{dN_H}$ is the total HA-FCGR comprising FCG dominated by the stress field at the crack tip $\frac{da}{dN_{P_H}}$, and far-field HA-FCGR $\frac{da}{dN_{\Delta K}}$.

7.3   Proposed FCG Model

Given that there will be a pressure dependence in the denominator(s) of Eq. 7.16, and that the FCGR relationship is intended to be valid for hydrogen pressures between zero (laboratory air) and 20.7 MPa, the following modification must be made to Eq. 13:

$$\frac{da}{dN_{total}} = \frac{da}{dN_{fatigue}} + \delta(P_H - P_{H_{th}})\frac{da}{dN_H},$$ Eq. 7.17

where δ is the Dirac delta operator and $P_{H_{th}}$ is a threshold hydrogen pressure below which HA-FCG does not occur, taken to be $P_{H_{th}} = 0.02$ MPa [16]. Combining Eqs. 7.16 and 7.17 yields

$$\frac{da}{dN_{total}} = \frac{da}{dN_{fatigue}} + \delta(P_H - 0.02)\left[\left(\frac{da}{dN_{P_H}}\right)^{-1} + \left(\frac{da}{dN_{\Delta K}}\right)^{-1}\right]^{-1}.$$ Eq. 7.18

The transient HA-FCG is given by

$$\frac{da}{dN_{P_H}} = a1\Delta K^{B1}\left(P_H^{m1}exp^{\left(\frac{-Q+V\sigma_h}{RT}\right)}\right)^{d1},$$ Eq. 7.19

and the steady-state HA-FCG is given by

$$\frac{da}{dN_{\Delta K}} = a2\Delta K^{B2}\left(P_H^{m2}exp^{\left(\frac{-Q+V\sigma_h}{RT}\right)}\right)^{d2}.$$ Eq. 7.20

The hydrostatic stress σ_h is determined using Eqs. 7.4 and 7.5. The crack propagation plane is assumed to occur at an angle of $\theta = 0°$ and the distance *r* is taken as a piece-wise function defined by

$$r = \begin{cases} Eq.\ 12, & da/dN_{N-1} \le Eq.\ 1 \\ da/dN_{N-1}, & da/dN_{N-1} > Eq.\ 1 \end{cases}$$ Eq. 7.21

where da/dN_{N-1} is the crack extension of the previous cycle. This formulation for the distance *r* assumes a critical distance damage approach to the HA crack extension, similar to that presented by [101]. Material-specific parameters in Eq. 7.4 (*n* and *α*) must be determined from

tensile test results. Furthermore, the yield strength as a function of gaseous hydrogen pressure must be determined. The *J*-integral in Eq. 7.4 was replaced with $J = \Delta K_I^2/E$, with $I_n = 3.2$ [79], $\tilde{\sigma}_{11} = 0.6$ [79], $\tilde{\sigma}_{22} = 1.2$ [79], and $\tilde{\sigma}_{33} = 0$. The activation energy is taken as $Q = 27.1$ kJ/mol-K [68] for both relationships (Eqs. 19 and 20). All other parameters (*a1*, *a2*, *B1*, *B2*, *d1* and *d2*) are fit to experimental hydrogen assisted fatigue crack growth data.

7.4   Model Calibration

To date the above model has been fully calibrated to API-5L X100 steel [102] and partially calibrated to X70 [103] and X52 [104]. The calibrated values for the HRR stress solution (Eq. 4) are provided in Table 7-1.

Table 7-1 Ramberg-Osgood hardening parameters for selected API steels tested in air [104]

Material	Orientation	Average α	Average n
		(-)	(-)
X52	Longitudinal	3.63	3.63
X52	Transverse	2.49	12.18
X70	Longitudinal	3.96	8.88
X100	Longitudinal	0.97	12.99
X100	Transverse	3.04	16.63

The hydrogen-pressure specific yield strength of X100 is defined by

$$\sigma_0 = 0.34 P_{H_2} + 693.7, \qquad\qquad\qquad \text{Eq. 7.22}$$

where σ_0 is the 2 % offset yield stress in MPa and P_{H_2} is the hydrogen test pressure in MPa. Ahn et al. [105] reported a yield stress softening (as a function of material hydrogen concentration) in A533B steel, while Capelle [101] reported a hardening response in API-5L X52 steel. As such, a hydrogen test pressure (or material hydrogen concentration) specific yield strength is supported in the literature and is suggested for the modeling here. Calibration of the hydrogen assisted fatigue crack growth model must be performed using four separate data sets; one data set in air and three data sets in hydrogen, with each hydrogen data set having been tested at different hydrogen pressures. Calibration of the model has been performed using two methods. The "full" calibration may be performed as follows:

1. The Paris relationship (Eq. 7.14) was fit to data created in air to determine constants *A* and *b*.

2. The parameter *B1* is set equal to the average value of the Paris exponent for the hydrogen-assisted transient FCG of all data sets conducted in gaseous hydrogen.

3.   The parameter *B2* is set equal to the average value of the Paris exponent for the hydrogen-assisted steady state FCG of all data sets conducted in gaseous hydrogen.

4.   The values for the parameters *m1* and *d1* are determined by fitting to ensure that the effect of increasing hydrogen pressure within the transient HA-FCG regime is captured. , i.e., an increase in hydrogen pressure yields the correct shift in the HA-FCG prediction.

5.   The values for the parameters *m2* and *d2* are determined by fitting to ensure that the effect of increasing hydrogen pressure within the steady state HA-FCG regime is captured. , i.e. , an increase in hydrogen pressure yields the correct shift in the HA-FCG prediction.

6.   The parameters *a1* and *a2* are final fitting parameters.

The full model calibration for X100 resulted in the parameter values provided in Table 7-2 [102].

Table 7-2 Parameters of model calibration for X100

a1	1.5×10^{-4}	*a2*	1.3×10^{4}
B1	7.96	*B2*	3.17
m1	0.75/*d1*	*m2*	0.22/*d2*
d1	3	*d2*	1

It was found, however, that a simplified version of the model provides sufficient accuracy for HA-FCG prediction of the API steels tested [104]. The simplified form sets $d2 = 0$ and $B2 = b$. As a result, the steady-state HA material response is assumed to be unaffected by changes in hydrogen pressure. This assumption is supported by the experimental results indicating that the FCG response of a material tested in hydrogen converges to a single line in the steady-state regime (higher values of *da/dN*), regardless of hydrogen pressure. A physical interpretation of this model formulation is that the mechanism governing the steady-state regime is dominated primarily by fatigue. In such a case, when gaseous hydrogen is present, the FCG response results from a competition between a hydrogen-enhanced mechanism (transient regime) and a fatigue-dominated mechanism (steady-state regime). At low *da/dN*, crack extension per cycle occurs within the region of material having the highest hydrogen concentration, resulting from a peak in hydrostatic stress at some distance in front of the crack tip. As such, the FCG response is dominated by hydrogen-assisted fatigue mechanisms. At higher values of *da/dN*, crack extension per cycle extends beyond the location of stress-enhanced hydrogen concentration. In this case, the first portion of the steady-state crack extension (per cycle) is dominated by the increased hydrogen concentration in the fatigue process zone, while the subsequent portion of the crack extension (per cycle) occurs as a result of the underlying fatigue mechanism overpowering the effect of the far-field hydrogen concentration within the material. The simplified model was calibrated for each material as follows:

1. The Paris relationship (Eq. 14) is fit to data acquired in air to determine constants A and b.

2. The Paris relationship is then fit to the linear section of the transient HA-FCG response for all hydrogen pressures tested. The parameter $B1$ is set equal to the average of the exponents within this regime.

3. The exponent $m1$ is then adjusted to account for the effect that the hydrogen pressure has upon the transient FCG response.

4. The parameter $B2$ is then set equal to b.

5. Lastly, the parameters $a1$ and $a2$ are adjusted for the final fit.

Calibration constants for the simplified version of the model calibrated to X100 and X52 are provided in Table 3.

Table 7-3 Calibrated parameter values for the simplified model [103,104]

API-5L X52				API-5L X70				API-5L X100			
A	7.1×10^{-9}	b	2.9	A	4.0×10^{-9}	b	3.21	A	9.9×10^{-9}	b	2.83
Transient		Steady State		Transient		Steady State		Transient		Steady State	
a1	1.2×10^{-15}	a2	3.4×10^{-7}	a1	1.2×10^{-15}	a2	1×10^{-7}	a1	3×10^{-13}	a2	4×10^{-7}
B1	10.24	B2	2.9	B1	10.24	B2	3.21	B1	7.96	B2	2.83
m1	0.7	m2	N/A	m1	0.7	m2	N/A	m1	0.7	m2	N/A
d1	1	d2	0	d1	1	d2	0	d1	1	d2	0

Figure 7-2 provides a visual understanding of how the model predicts the interactions between the dominant damage mechanisms (Eqs. 19 and 20) for full model calibration to X100.

(a)   (b)
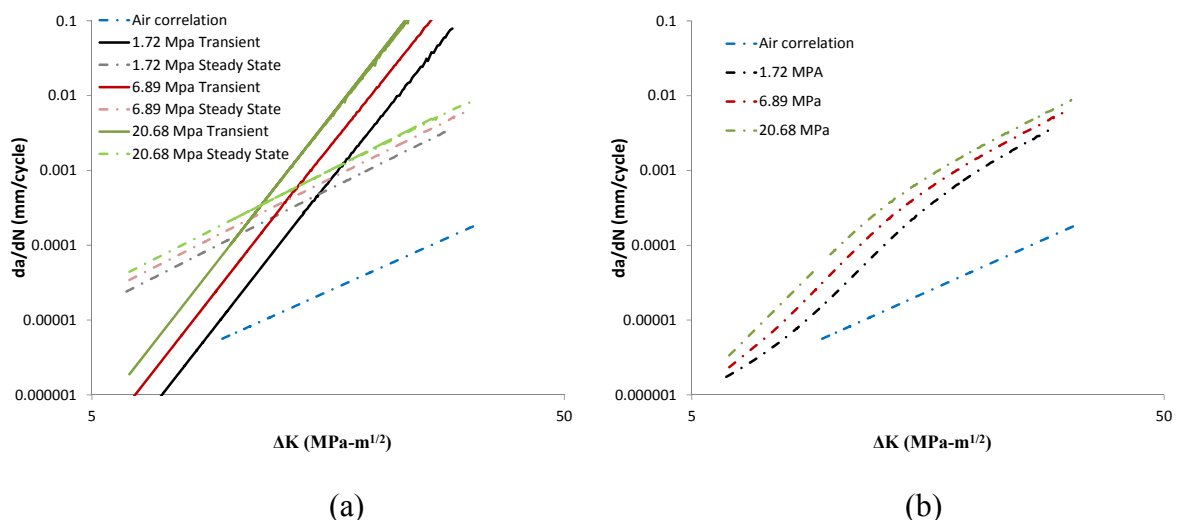
Figure 7-2 Model predictions: (a) independent damage mechanisms from Eqs. 19 and 20, and (b) damage mechanisms combined in final predictive form (Eq. 18).

Figure 7-2 indicates that Eq. 19 dominates at smaller values of ΔK and Eq. 20 dominates at larger ΔK values, as would be expected by the argument on the segregation of the dominant damage mechanisms. Curves of experimental and correlated FCGR versus ΔK are provided on the same axis in Figure 7-3, for the three materials calibrated to date.

In general, model predictions indicate that as hydrogen pressure increases, so does da/dN for a given ΔK. The model also indicates that the converse is true, i.e., there is an inverse relationship between hydrogen pressure and driving force for a given da/dN. The model performs well at correlating the HA-FCG of the three API pipeline steels that it has been calibrated for.
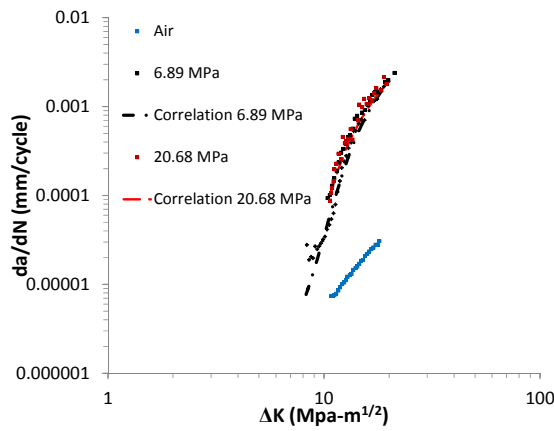
(a)
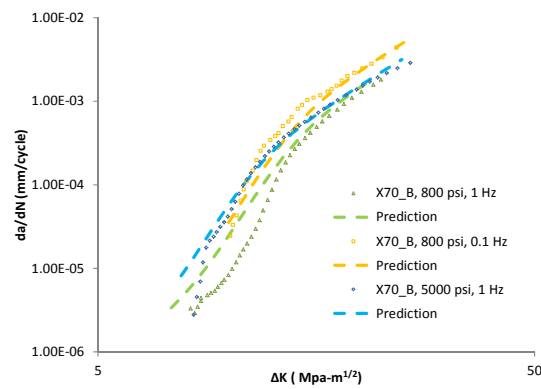
(b)
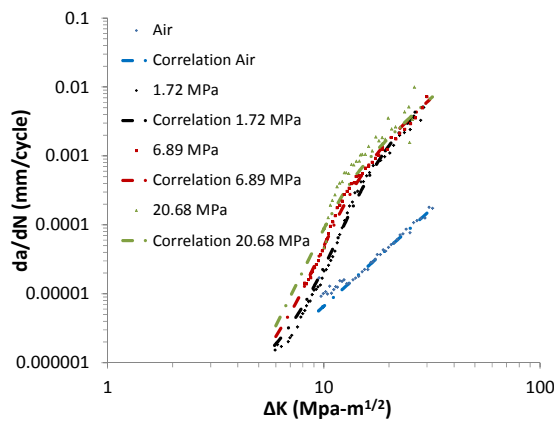
(c)

Figure 7-3 Experimental and correlated FCG results for a) X52, b) X70 and c) X100

8   Codes Recommendation

8.1   Relevant Finding of Project Work

8.1.1   Experimental

Fatigue crack growth experiments were performed on X52 and X70 steels in both air and high-pressure, gaseous hydrogen (Table 4-3 in section 4.3). Experimental results indicate that the presence of gaseous hydrogen increases the FCGR of all materials tested. At lower values of ΔK (ΔK values between 7 MPa·m$^{1/2}$ and 9 MPa·m$^{1/2}$), the increase in FCGR may be modest over that of air; whereas the FCGR is vastly increased over that of air for higher values of ΔK. The rate of FCGR approaches that of air for ΔK values below about 7 MPa·m$^{1/2}$ and above about 15 MPa·m$^{1/2}$. That is, the Paris exponent is very close to that of air. Between approximately 7 MPa·m$^{1/2}$ and 15 MPa·m$^{1/2}$ the rate of FCGR increases dramatically, with the Paris exponent doubling or even tripling over that of air for certain materials. Hydrogen-assisted FCGR appears to increase with increasing hydrogen pressures at ΔK values below approximately 15 MPa·m$^{1/2}$. However, the FCGR response for all materials in all hydrogen pressures tested appears to fall within a relatively narrow band. Furthermore, decreasing the test frequency has an effect similar to increasing the hydrogen test pressure. FCGR does not appear to be affected by the strength of the steel, as it is in monotonic tensile testing. FCGRs of X70 were not significantly different, meaning that results did not fall outside of the experimental uncertainty, than those for X52. Additionally, FCGR testing of an X100 pipeline steel, as part of a previous U.S. DOT project, gave results that were not significantly different from the X70 and X52 results produced as part of this work.

8.1.2   Modeling

The hydrogen-assisted FCG response of the API steels tested can be divided into three regimes, each controlled by separate dominant damage mechanisms. At low ΔK values, the FCG response in air (termed pure fatigue) dominates the HA-FCGR response.   At intermediate ΔK values, a damage mechanism controlled by the hydrogen accumulation in front of the crack tip dominates the overall FCG response. While at higher ΔK values, where the HA FCGR exhibits a Paris exponent similar to FCG in air, the FCGR is controlled more by addition of "pure fatigue" plus a hydrogen-assisted component that is from hydrogen that is effectively saturated in front of the crack tip. Microscopy of the FCG surfaces indicate similar crack mechanisms between the pre-crack performed in air and the HA-FCG at ΔK values above approximately 15 MPa·m$^{1/2}$.

A phenomenological model is proposed which separates the overall FCG into 3 dominant mechanisms. First, the model assumes that the FCGR is comprised of a superposition of "pure fatigue" and a hydrogen-assisted component. Second, the hydrogen-assisted component is further separated into a hydrogen accumulation-dominated component and a ΔK-dominated component. The HA-FCGR then results from the interaction of these two mechanisms. The

model does a good job of predicting FCGR of the materials tested as a function of ΔK and hydrogen pressure.

A stress-driven hydrogen diffusion model was developed under a moving-source framework. It provided a new view point toward the hydrogen-enhanced fatigue crack growth, and its solution was able to explain the rate-limited, transient process in HA-FCGR. Given the fundamental material properties such hydrogen diffusivity, yield strength, the model's simplified solution was able to predict the upper bound of the HA-FCGR and the influences of major process variables such as hydrogen pressure, load ratio, and load frequency.

8.3.   Recommendations to Industrial Practice and Standards

8.3.1. Experimental

The experimental results show that a single conservative dataset can be produced from the mean of all four materials at high pressures of hydrogen gas (34 MPa, in this case), and from three of the four materials at low pressures of hydrogen gas (5.5 MPa, in this case). The fourth dataset at low pressure, 5.5 MPa, is from a vintage X52 pipeline material that gives lower FCGRs. These conservative datasets will be proposed as additions to the ASME B31.12 code on hydrogen piping and pipelines. The ASME B31.12 committee will discuss the specification of a desired microstructure for applications involving hydrogen gas to be added to the code.

8.3.2. Modeling

The proposed phenomenological model provides a framework for understanding the damage mechanisms occurring during HA-FCG. However, the framework may be cumbersome for first run engineering calculations. As such, a simplified form utilizing three Paris relationships (one for each of the three dominant damage mechanisms) is proposed

$$\frac{da}{dN_{total}} = \frac{da}{dN_{fatigue}} + \delta(P_H - 0.02)\left[\left(\frac{da}{dN_{P_H}}\right)^{-1} + \left(\frac{da}{dN_{\Delta K}}\right)^{-1}\right]^{-1}, \text{where}$$

$\frac{da}{dN_{fatigue}} = c_1\Delta K^{m_1}, \frac{da}{dN_{P_H}} = c_2\Delta K^{m_2}$ and $\frac{da}{dN_{\Delta K}} = c_3\Delta K^{m_3}$. This mathematical form is easily implemented in readily available mathematical and spreadsheet programs to predict da/dN for a range of ΔK values. It is this form of the predictive model that NIST is working with ASME B31.12 to implement into future codes.

For the hydrogen diffusion model, it can be further developed to provide a tool for industries and codes committees. Given the basic conditions such hydrogen pressure, material grades, loading ratio, and loading frequency, this tool would be able to predict the upper bound of HA-FCGR.

9 Conclusions and Future Works

In summary, the following conclusions can be drawn from the completed project research work:

1. An innovative multi-specimen link system was successfully designed and used in fatigue crack growth tests of high-strength pipeline steels in high-pressure gaseous hydrogen environments;

2. Using the multi-specimen system, FCGR tests on four types of pipeline steels, two of API-5L X52, two of API-5L X70, were tested under different hydrogen pressures (air, 800psi, and 5000psi), three loading levels, and three load frequencies (1Hz, 0.1Hz, and 0.01Hz);

3. The test results were able to establish the dependencies of FCGR on major process variables such as pipeline steel grade, hydrogen pressure, and load frequency;

4. A stress-driven hydrogen diffusion model was successfully developed to determine the hydrogen concentration profile in the region around the advancing crack tip. The model was able to explain the transient nature of the hydrogen-enhanced FCGR during the test. Good correlation between the model and the test data was achieved;

5. A phenomenological model for fatigue crack propagation was also developed by NIST. The model correlates well with test results and elucidates how the deformation mechanisms contribute to fatigue crack propagation in pipeline steel in environments similar to those found in service; and

6. The test data and the some of the model analyses have been published or will be published. Recommendation to code update or modification has been discussed and will be communicated to relevant industrial codes committees.

While the test data produced by the project work provided a basic data set for industrial codes update and modifications, there are technical gaps that need to be filled. These include, but not limited to:

1. Making use of the innovative, efficient multi-specimen system for further FCGR tests to investigate the effects of other process variables such as load ratio, hydrogen gas temperature;

2. Perform similar FCGR test in gaseous hydrogen environment on welds of pipeline steels; and

3. Both the hydrogen diffusion model and the phenomenological model for fatigue crack propagation can be improved with expanded database of FCGR in gaseous hydrogen.

10 Appendix: Analytical Model of Hydrogen Diffusion around Fatigue Crack Tip

From Figure 6-2, if we assume the crack tip is uniform in the thickness direction of the specimen, then the hydrogen uptake at the crack tip can be treated as a moving line source. We further assume that the line source's uptake rate of hydrogen is $\dot{q}$ (per unit time and per unit length) is linearly related to the hydrogen concentration at the crack tip. For a cyclically loaded crack tip, the hydrogen uptake rate $\dot{q}$ is a function of time.

Consider such a time-dependent, moving hydrogen line source at x=0, the concentration solution to Eq. 6.9, according to Carslaw and Jaeger [61], is the following integral:

$$C_H = \int_0^t \frac{\dot{q}}{4\pi Dt'} e^{-\frac{[(x+ut')^2+z^2]}{4Dt'}} dt' \qquad \text{A-1}$$

If $\dot{q}$, like hydrogen concentration at the crack tip, can be divided into an averaged component and a sinuous component:

$$\dot{q} = \dot{q}_{avg} + \Delta\dot{q}\cos(\omega t)$$

Then equation A-1 becomes:

$$C_H = \int_0^t \frac{(\dot{q}_{avg} + \Delta\dot{q}\cos(\omega t))}{4\pi Dt'} e^{-\frac{[(x+ut')^2+z^2]}{4Dt'}} dt' \qquad \text{A-2}$$

Introduce variable $\xi = \frac{R^2}{\sqrt{4Dt'}}$ and $R^2 = x^2 + z^2$, then equation A-2 can be further transformed as

$$C_H = \frac{e^{-\frac{ux}{D}}}{2\pi D}\left\{\dot{q}_{avg}\left[K_o\left(\frac{Ru}{2D}\right) - \frac{1}{2}\int_0^{\frac{R^2}{4Dt}} \frac{d\xi}{\xi} e^{-\left(\xi+\frac{1}{4\xi}\left(\frac{Ru}{2D}\right)^2\right)} d\xi\right] + \right.$$

$$\left. \Delta\dot{q}\int_0^\infty \cos\omega(t - \frac{R^2}{4D\xi})\frac{1}{\xi} e^{-\left(\xi+\frac{1}{4\xi}\left(\frac{Ru}{2D}\right)^2\right)} d\xi\right\} \qquad \text{A-3}$$

The second term in the curved bracket of the above equation is related to the cyclic hydrogen uptake rate, and can be simplified through the following equation[61, page 65]:

$$\frac{2}{\sqrt{\pi}}\int_0^\infty \cos\omega\left(t - \frac{R^2}{4D\xi}\right)\frac{1}{2\xi} e^{-\left(\xi+\frac{1}{4\xi}\left(\frac{Ru}{2D}\right)^2\right)} d\xi = K_o\left(R\left(\frac{\omega}{2D}\right)^{\frac{1}{2}}\right)\cos\left[\omega t - R\left(\frac{\omega}{2D}\right)^{\frac{1}{2}}\right].$$

If we neglect the dependency of the solution on z, i.e., let $R=x$, and substitute the above equation into equation A-3,

$$C_H = \frac{e^{-\frac{ux}{D}}}{2\pi D}\left\{\dot{q}_{avg}\left[K_o\left(\frac{xu}{2D}\right) - \frac{1}{2}\int_0^{\frac{x^2}{4Dt}} \frac{d\xi}{\xi} e^{-\left(\xi+\frac{1}{4\xi}\left(\frac{xu}{2D}\right)^2\right)} d\xi\right] + \Delta\dot{q}K_o\left(x\left(\frac{\omega}{2D}\right)^{\frac{1}{2}}\right)\cos\left[\omega t - x\left(\frac{\omega}{2D}\right)^{\frac{1}{2}}\right]\right\}$$

Recall that we assume the linear relationship between the hydrogen uptake rate ($\dot{q}_{avg}$ and $\Delta\dot{q}$) and the local hydrogen concentration at the crack tip, the above equation will lead to Eqs. 6-10, 6-11 and 6-12.

11 References

1   Jewett, R. P., 1973, Hydrogen Environment Embrittlement of Metals, NASA-CR-2163.

2   Walter, R.J., Hayes, H. G., Chandler, W. T., Influence of gaseous hydrogen on metals. Technical Report. 1971, Rocketdyne, Canoga Park, California (USA).

3   Jewett, R. P., 2001, Proceedings, DOE Pipeline Working Group Meeting, August 2001.

4   Cialone, H. J. and Holbrook, J. H., 1985, Effects of Hydrogen on Fatigue Crack Growth in Pipeline Steels", Metallurgical Transactions A, Vol. 16A, pp115-122.

5   Somerday, B. P., 2007, Technical Reference on Hydrogen Compatibility of Materials, Report No. SAND2008-1163, at http://www.ca.sandia.gov/matlsTechRef/.

6   *ASTM Standard E 647-11 "Test Method for Measurement of Fatigue Crack Growth Rates."* 2011, ASTM International. p. 46.

7   Hoover, W.R., Robinson, S. L., Stoltz, R. E., Spingarn, J. R., Hydrogen Compatibility of Structural Materials for Energy Storage and Transmission. Final report. 1981, Sandia National Labs., Livermore, CA, USA. p. pp. 64.

8   Cialone, H.J., Holbrook, J. H. Microstructural and Fractographic Features of Hydrogen-Accelerated Fatigue-Crack Growth in Steels. in Welding, Failure Analysis, and Metallography. 1987. Denver, CO, USA: ASM.

9   Cialone, H., J., Holbrook, J., H., Sensitivity of steels to degradation in gaseous hydrogen. 962 ed. ASTM STP 962. Vol. STP. 1988: ASTM STP 962. Hydrogen Embrittlement: Prevention and Control

10   Robinson, S.L., Stoltz, R. E. Toughness Losses and Fracture Behavior of Low Strength Carbon-Manganese Steels in Hydrogen. in Hydrogen Effects in Metals: Proceedings of the Third International Conference on Effect of Hydrogen on Behavior of Materials. 1981. Moran, WY, USA: Metall Soc of AIME.

11   Gutierrez-Solana, G., Elices, M. High-Pressure Hydrogen Behavior of a Pipeline Steel. in Current Solutions to Hydrogen Problems in Steels. 1982. Washington, DC, USA: ASM.

12   Nelson, H., G. On the Mechanism of Hydrogen-Enhanced crack Growth in Ferritic Steels. in Proceedings of the 2nd Conference on the Mechanical Behavior of Mateirals. 1976. Boston, Mass: ASM.

13   Walter, R.J., Chandler, W. T. Cyclic-Load Crack Growth in ASME SA-105 Grade II Steel in High-Pressure Hydrogen at Ambient Temperature. in Effect of Hydrogen Behavior of

Materials: Proceedings of the International Conference. 1976. Lake Moran, WY: Metall Soc of AIME, New York, NY.

14 Nelson, H., G. Hydrogen-Induced Slow Crack Growth of a Plain Carbon Pipeline Steel Under Conditions of Cyclic Loading. in Effect of Hydrogen Behavior of Materials: Proceedings of the International Conference. 1976. Lake Moran, WY: Metall Soc of AIME, New York, NY.

15 Nanninga, N., Slifka, A., Levy, Y., White, C., A review of fatigue crack growth for pipeline steels exposed to hydrogen. Journal of Research of the National Institute of Standards and Technology, 2010. 115(6): p. 437-452.

16 Somerday, B., P., Technical Reference on Hydrogen Compatibility of Materials- Plain Carbon Ferritic Steels: C-Mn Alloys (Code 1100). 2008, Sandia National Laboratories, Livermore, CA. p. 32.

17 Lam, P.S., Sindelar, R. L., Adams, T. M. Literature Survey of Gaseous Hydrogen Effects on the Mechanical Properties of carbon and Low carbon Steels. in ASME Pressure Vessels and Piping Division Conference. July 22-26, 2007. San Antonio, TX.

18 A. R. Troiano, The role of hydrogen and other interstitials in the mechanical behavior of metals. Transactions of ASM 1960; 52:54-80.

19 S.P. Lynch, Mechanisms of hydrogen assisted cracking-A review. in Hydrogen Effects in Materials, Eds., N.R. Moody and A.W. Thompson, The Minerals, Metals & Materials Society, Warrendale, PA, 2003

20 R. A. Oriani, Hydrogen embrittlement of steels. Annual Reviews Materials Science 1978; 327-357.

21 H. K. Birnbaum, I. M. Robertson, P. Sofronis,and D. Teter, Mechanisms of hydrogen related fracture—A review. In: 2nd International Conference on Corrosion-Deformation Interactions in conjunction with EUROCORR '96 Nice,France, 1997, pp. 172-195.

22 R. P. Gangloff, Hydrogen assisted cracking of high strength alloys. In: Comprehensive Structrual Integrity, Vol. 6., I. Milne, R. O. Ritchie, and B. Karihaloo, eds., New York, NY: Elsevier Science, 2003, pp. 31-101.

23 Novak, P., Yuan, R., Somerday, B. P., Sofronis, P., Ritchie, R. O., A statistical, physical-based, micro-mechanical model of hydrogen-induced intergranular fracture in steel. Journal of the Mechanics and Physics of Solids, 2010. 58(2): p. 206-226.

24 H. K. Birnbaum, I. M. Robertson, P. Sofronis,and D. Teter, Mechanisms of hydrogen related fracture—A review. In: 2nd International Conference on Corrosion-Deformation Interactions in conjunction with EUROCORR '96 Nice, France, 1997, pp. 172-195.

25 Gangloff, R., P. Science-based prognosis to manage structural alloy performance in hydrogen. in Effects of Hydrogen on Materials: Proceedings of the 2008 International Hydrogen Conference. 2009. Jackson, WY, USA: ASM International.

26 R. P. Wei, Hydrogen Effects in Metals, ed. I. M. Bernstein AND a. W. Thompson (Warrendale, PA: The Mineral, Metals and Materials Society, 1981), 677

27 W. W. Gerberich, Y. Y. Chen and C. John, Metall. Trans. A., 6A(1975), 1485.

28 J. P. Thomas and R. P. Wei, Corrosion fatigue crack growth of steels in aqueous solutions I: experimental results and modeling the effects of frequency and temperature. Materials Science and Engineering A 1992; A159 (2):205-221.

29 J. P. Thomas and R. P. Wei, Corrosion fatigue crack growth of steels in aqueous solutions II: modeling the effects of K. Materials Science and Engineering A 1992; A159(2):223-229.

30 R. M. N. Pelloux, Mechanisms of formaion of ductile fatiguestriations. Transactions of ASM 1969; 62:281-285.

31 H. Kotake, R. Matsumoto, S. Taketomi, and N. Miyazaki, Transient hydrogen diffusion analysis coupled with crack-tip plasticity under cyclic loading, International Journal of Pressure Vessel and Piping, 85(2008), 540-549

32 P. Sofronis, Y. Liang, N. Aravas, Hydrogen induced shear localization of the plastic flow in metals and alloys, European J. Mech. A: Solids 2001; 20:857-72.

33 Y. Liang, P. Sofronis, Toward a phenomenological description of hydrogen-induced decohesion at particle/matrix interface, J. Mech. Phys. Solids 2003; 51:1509-31.

34 W.W. Gerberich, P.G. Marsh and J.W. Hoehn, in: A.W. Thompson and N.R. Moody (Eds.) Hydrogen Effects in Materials, Minerals, Metals & Materials Society, Warrendale, PA, 1996, 539-553.

35 Y. Katz, N. Tymiak and W.W. Gerberich, Engr. Frac. Mech. 68 (2001) 619-646.

36 R.P. Gangloff, in: N.R. Moody et al. (Eds.) Hydrogen Effects on Material Behavior and Corrosion Deformation Interactions, Minerals, Metals & Materials Society, Warrendale, PA, 2003, 477-497.

37 Z. Gasem and R.P. Gangloff, in: R.H. Jones (Ed.) Chemistry and Electrochemistry of Corrosion and Stress Corrosion Cracking, Minerals, Metals & Materials Society, Warrendale, PA, 2001, 501-521.

38 R.P. Wei and R.P. Gangloff, in: R.P. Wei and R.P. Gangloff (Eds.) Fracture Mechanics: Perspectives and Directions, STP 1020, ASTM International, West Conshohocken, PA, 1989, 233-264.

39 R.P. Gangloff, "Critical Issues in Hydrogen Assisted Cracking of Structural Alloys", in Environment Induced Cracking of Materials (EICM-2), Sergei Shipilov, R.H. Jones, J.-M Olive, and R.B. Rebak, eds., Elsevier Science, Oxford, UK, pp. 141-166 (2007).

40 H.P. van Leeuwen, The kinetics of hydrogen embrittlement: A quantitative diffusion model. Engr. Frac. Mech., 6, 1974, 141-161.

41 H.H. Johnson, in: "Hydrogen in Metals," Eds., I.M. Bernstein and A.W. Thompson, ASM International, Materials Park, OH, 1974, pp. 35-49.

42 X. Chen and W.W. Gerberich, The kinetics and micromechanics of hydrogen assisted cracking in Fe-3 pct Si single crystals. Metall. Trans. A, 22A, 1991, 59-70.

43 W.W. Gerberich, Y.T. Chen and C. St. John, A short-time diffusion correlation for hydrogen induced crack growth kinetics. Metall. Trans. A, 6A, 1975, 1485-1498.

44 H.P. van Leeuwen, Quantitative models of hydrogen-induced cracking in high strength steels. Review on Coatings and Corrosion," 4, 1979, 5-93.

45 J. Toribio and V. Kharin, The effect of history on hydrogen assisted cracking. Intl. J. Frac., 88, 1997, 233-258.

46 Thomas, J., P., Wei, R., P., Corrosion fatigue crack growth of steels in aqueous solutions I: Experimental results and modeling the effects of frequency and temperature. Materials Science and Engineering: A, 1992. 159(2): p. 205-221.

47 Thomas, J.P., Wei, R., P., Corrosion fatigue crack growth of steels in aqueous solutions II: Modeling the effects of ΔK. Materials Science and Engineering: A, 1992. 159(2): p. 223-229.

48 R. P. Wei and G. W. Simmons, Environment enhanced fatigue crack growth in high-strength steels. Stress Corrosion Cracking and Hydrogen Embrittlement of Iron Base Alloys Unieux-Firminy, France, 1973, pp. 751-765.

49 R. P. Gangloff, Diffusion control of hydrogen environment embrittlement in high strength alloys. Hydrogen Effects on Material Behavior and Corrosion Deformation Interactions. N. R. Moody, R. E. Ricker, G. W. Was, and R. H. Jones, eds.,Moran, WY, 2003, pp. 477-497.

50 Austen, I.M., McIntyre, P., Corrosion fatigue of high-strength steel in low-pressure hydrogen gas. Metal Science, 1979. 13(7): p. 420-428.

51 R.P. Gangloff, in Environment Induced Cracking of Metals, R.P. Gangloff and M.B. Ives, eds., NACE, Houston, TX, pp. 55-109 (1990).

52 R.P. Gangloff, in Fatigue '02, Anders Blom, ed., Engineering Materials of Corrosion Advisory Services, West Midlands, UK, pp. 3401-3433 (2002).

53 Darcis, P., McColskey, J.D., Lasseigne, A., Siewert, T.A., Hydrogen Effects on Fatigue Crack Growth Rate in High Strength Pipeline Steel, Proc. International Hydrogen Conference 2008

54 Suresh, S., Ritchie, R. O., Mechanistic dissimilarities between environmentally influenced fatigue crack propagation at near-threshold and higher growth rates in lower strength steels. Metal Science, 1982. 16(11): p. 529-538

55 Yoshioka, S., Kumasawa, M., Demizu, M., Inoue, A., , Fatigue Crack Growth Behavior in Hydrogen Gas Environment, in Third International Conference on Fatigue and Fatigue Thresholds. June 28- July 3, 1987: Charlottesville, VA.

56 Wachob, H., F., The Influence of Microstructure on the Resistance of Low Strength Ferrous Alloys to Gas Phase Hydrogen Degradation, in NASA Contractor Report 166334. 1981, Failure Analysis Associates, Palo Alto, CA. p. 56.

57 San Marchi, C., Stalheim, D., G., Somerday, B., P., Boggess, T., Nibur, K., A., Jansto, S., Fracture and Fatigue of Commercial Grade API Pipeline Steels in Gaseous Hydrogen, in ASME Pressure Vessels & Piping Division/ K-PVP 2010 Conference. 2010, ASME: Bellevue, Washington, USA. p. 10

58 Capelle, J., Gilgert, J., Dmytrakh, I., Pluvinage, G., Sensitivity of pipelines with steel API X52 to hydrogen embrittlement. International Journal of Hydrogen Energy, 2008. 33(24): p. 7630-7641.

59 Tsay, L.W., Huang, W.B., Li, Y.M., and Chen, C., Hydrogen Embrittlement of a Ti-Strengthened 250 Grade Maraging Steel. Journal of Materials Engineering and Performance, 1997. 6(2): p. 177-181.

60 R. Gangloff and R. Wei, Gaseous hydrogen embrittlement of high strength steels. Metallurgical and Materials Transactions A, 1977. 8(7): p. 1043-1053.

61 H. S. Carslaw and J. C. Jaeger, conduction of Heat in Solids, 2nd edition, 1959

62 Feng, Z., Hydrogen Permeability and Integrity of Hydrogen Delivery Pipelines, 2005 DOE Hydrogen Program Peer Review.

63 M. Skjellerudsveen, O.M. Akselsen, V. Olden, R. Johnsen, A. Smirnova, The effect of microstructure and temperature on hydrogen diffusion in X70 grade pipeline steel and its weldments, EUROCORR 2010, Sept. 13-17, 2010, Moscow, Russia.

64 Armbruster, M.H., J. Am. Chem. Soc. 65 (1943) 1043-1054.

65 San Marchi, C., Stalheim, D., G., Somerday, B., P., Boggess, T., Nibur, K., A., Jansto, S., Fracture and Fatigue of Commercial Grade API Pipeline Steels in Gaseous Hydrogen, in ASME Pressure Vessels & Piping Division/ K-PVP 2010 Conference. 2010, ASME: Bellevue, Washington, USA. p. 10.

66 San Marchi, C., Stalheim, D., G., Somerday, B., P., Boggess, T., Nibur, K., A., Jansto, S., Fracture Resistance and Fatigue Crack Growth of X80 Pipeline Steel in Gaseous Hydrogen, in ASME Pressure Vessels & Piping Division/ K-PVP 2011 Conference. 2011, ASME: Baltimore, Maryland, USA. p. 9.

67 Stalheim, D., San Marchi, C., Somerday, B., Boggess, T., Jansto, S., Muralidharan, G., Sofronis, P. Microstructure and Mechanical Property performance of Commercial Grade API Pipeline Steels in High Pressure Gaseous Hydrogen. in 8th International Pipeline Conference. 2010. Calgary, Alberta, Canada: ASME.

68 Nelson, H., G., Stein, J., E., Gas-Phase Hydrogen Permeation Through Alpha Iron, 4130 Steel, and 304 Stainless Steel From Less Than 100C to Near 600C. 1973, NASA Technical Note D-7265.

69 Sieverts, A., Absorption of Gases by Metals. Zeitschrigt fur Metallkunde, 1929. 29: p. 37-46.

70 Gangloff, R., Wei, R., Gaseous hydrogen embrittlement of high strength steels. Metallurgical and Materials Transactions A, 1977. 8(7): p. 1043-1053.

71 Gangloff, R.P., Hydrogen Assisted Cracking in High Strength Alloys, in Comprehensive Structural Integrity. Comprehensive Structural Integrity, ed. I. Milne, Richie, R. O., Karihaloo, O., Petit, J., Scott, P.,. Vol. 6. 2003, New York, NY: Elsevier Science.

72 Dean, S., W., Review of recent studies on the mechanism of stress-corrosion cracking in austenitic stainless steels. ASTM STP 1976. 1976: ASTM STP 1976. Stress Corrosion- New Approaches. 30.

73 Mao, S.X., Li, M., Mechanics and thermodynamics on the stress and hydrogen interaction in crack tip stress corrosion: experiment and theory. Journal of the Mechanics and Physics of Solids, 1998. 46(6): p. 1125-1137.

74 Hirth, J., Effects of hydrogen on the properties of iron and steel. Metallurgical and Materials Transactions A, 1980. 11(6): p. 861-890.

75 Zhang, T., Chu, W. Y., Gao, K. W., Qiao, L. J., Study of correlation between hydrogen-induced stress and hydrogen embrittlement. Materials Science and Engineering: A, 2003. 347(1-2): p. 291-299

76 Lu, B.T., Luo, J. L., Norton, P. R., Ma, H. Y., Effects of dissolved hydrogen and elastic and plastic deformation on active dissolution of pipeline steel in anaerobic groundwater of near-neutral pH. Acta Materialia, 2009. 57(1): p. 41-49.

77 Hutchinson, J.W., Singular behaviour at the end of a tensile crack in a hardening material. Journal of the Mechanics and Physics of Solids, 1968. 16(1): p. 13-31.

78 Rice, J.R., Rosengren, G. F., Plane strain deformation near a crack tip in a power-law hardening material. Journal of the Mechanics and Physics of Solids, 1968. 16(1): p. 1-12.

79 Anderson, T., L., Fracture Mechanics, Fundamentals and Applications. Third ed. 2005, Boca Raton, FL: CRC Press. 621.

80 McMeeking, R.M., Parks, D. M., On Criteria for J-Dominance of Crack Tip Fields in Large-Scale Yielding. ASTM STP 668. Vol. American Society for Testing and Materials. 1979: ASTM STP 668. Elastic Plastic Fracture. 175-194.

81 Tang, N.Y., Plumtree, A., Fatigue-creep-environmental interaction: a kinetic approach. Materials Science and Engineering: A, 1991. 141(1): p. 55-61.

82 Maier, H., Teteruk, R., Christ, H., Modeling thermomechanical fatigue life of high-temperature titanium alloy IMI 834. Metallurgical and Materials Transactions A, 2000. 31(2): p. 431-444.

83 Martínez-Esnaola, J.M., Martín-Meizoso, A., Affeldt, E. E., Bennett, A., Fuentes, M., Hight Temperature Fatigue in Single Crystal Superalloys. Fatigue & Fracture of Engineering Materials & Structures, 1997. 20(5): p. 771-788.

84 Christ, H.-J., Teteruk, R., Jung, A.,, Maier, H., J,, Using fracture mechanics concepts for a mechanism-based prediction of thermomechanical fatigue life. 1428 ed. ASTM STP 1428. 2003: ASTM STP 1428. Thermomechanical Fatigue Behavior of Materials: 4th Volume 145-163.

85 Reuchet, J., Remy, L., Fatigue Oxidation Interaction in a Superalloy - Application to Life Prediction in Hight Temperature Low Cycle Fatigue. Metallurgical transactions. A, Physical metallurgy and materials science, 1983. 14 A(1): p. 141-149.

86 MacLachlan, D.W., Knowles, D. M., Fatigue behaviour and lifing of two single crystal superalloys. Fatigue & Fracture of Engineering Materials & Structures, 2001. 24(8): p. 503-521.

87 Liu, H.W. and Y. Oshida, Grain boundary oxidation and fatigue crack growth at elevated temperatures. Theoretical and Applied Fracture Mechanics, 1986. 6(2): p. 85-94.

88 Valerio, P., Gao, M., Wei, R.P., Environmental enhancement of creep crack growth in Inconel 718 by oxygen and water vapor. Scripta Metallurgica et Materialia, 1994. 30(10): p. 1269-1274.

89 Miller, M.P., McDowell, D. L., Oehmke, R. L. T., A Creep-Fatigue-Oxidation Microcrack Propagation Model for Thermomechanical Fatigue. Journal of Engineering Materials and Technology, 1992. 114(3): p. 282-288.

90 Yoon, K., B., Park, T., G., Saxena, A., Elevated Temperature Fatigue Crack Growth Model for DS-GTD-111, in 11th International Conference on Fracture. 2005.

91 Gangloff, R., P. Science-based prognosis to manage structural alloy performance in hydrogen. in Effects of Hydrogen on Materials: Proceedings of the 2008 International Hydrogen Conference. 2009. Jackson, WY, USA: ASM International.

92 Wei, R., P., Landes, J., Correlation Between Sustained Load and fatigue Crack Growth in High Strength Steels. Materials Research and Standards, 1970. 9: p. 25-27, 44-46.

93 Bucci, R.J., Environment enhanced fatigue and stress corrosion cracking of a titanium alloy plus a simple model for the assessment of environmental influence on fatigue behavior. 1970, Lehigh University, PhD: Bethlehem.

94 Neu, R.W., Sehitoglu, H., Thermomechanical fatigue, oxidation, and creep. Part II. Life prediction. Metallurgical transactions. A, Physical metallurgy and materials science, 1989. 20 A(9): p. 1769-1783.

95 Sen, I., Tamirisakandala, S., Miracle, D. B., Ramamurty, U., Microstructural effects on the mechanical behavior of B-modified Ti–6Al–4V alloys. Acta Materialia, 2007. 55(15): p. 4983-4993.

96 Novak, P., Yuan, R., Somerday, B. P., Sofronis, P., Ritchie, R. O., A statistical, physical-based, micro-mechanical model of hydrogen-induced intergranular fracture in steel. Journal of the Mechanics and Physics of Solids, 2010. 58(2): p. 206-226.

97 Wei, R.P., Gao, Ming, Reconsideration of the superposition model for environmentally assisted fatigue crack growth. Scripta Metallurgica, 1983. 17(7): p. 959-962.

98 Saxena, A., Williams, R., S., Shih, T., T., A Model for Representing the Influence of Hold Time on Fatigue Crack Growth Behavior at Elevated Temperatures. ASTM STP 743, ed. R. Roberts. 1981: ASTM STP 743. Fracture Mechanics: Thirteenth Conference.

99 Fournier, L., Delafosse, D., Magnin, T., Cathodic hydrogen embrittlement in alloy 718. Materials Science and Engineering: A, 1999. 269(1-2): p. 111-119.

100 Rezai-Aria, F., Remy, L., Oxidation fatigue interaction damage model for thermal fatigue crack growth. Engineering Fracture Mechanics, 1989. 34(2): p. 283-294.

101 Capelle, J., Gilgert, J., Pluvinage, G., A fatigue initiation parameter for gas pipe steel submitted to hydrogen absorption. International Journal of Hydrogen Energy, 2010. 35(2): p. 833-843.

102 Amaro, R.L., Findley, K. O., Rustagi, N., Drexler, E. S., Slifka, A. J., Fatigue Crack growth of X100 Pipeline Steels in Gaseous Hydrogen. International Journal of Fatigue, in Review, 2013.

103 Drexler, E.S., Slifka, A. J., Amaro, R. L., Barbaosa, N., Lauria, D. S., Hayden, L. E., Stalheim, D. G. Fatigue Crack Growth Rates of API X70 Pipeline Steel in a Pressurized Hydrogen Gas Environment. in International Ocean (Offshore) and Polar Engineering Conference. 2013. Anchorage, Alsaska.

104 Amaro, R.L., Drexler, E. S., Slifka, A. J., Fatigue Crack Growth Modeling of Pipeline Steels in High Pressure Gaseous Hydrogen. International Journal of Fatigue, in Review, 2013.

105 Ahn, D.C., Sofronis, P., Dodds Jr, R. H., On hydrogen-induced plastic flow localization during void growth and coalescence. International Journal of Hydrogen Energy, 2007. 32(16): p. 3734-3742.

CRES provides multidisciplinary and cost effective solutions to high-impact and complex problems facing the energy industry. CRES specializes in the reliability and structural integrity of energy systems that encompass a wide range of physical facilities for energy exploration, production, transportation, and delivery.

The highly dedicated staff of CRES solves practical problems through the understanding of their fundamental underpinnings and mechanisms. CRES strives to positively influence the industry practice through its leadership and active participation in the revision and update of industry codes and standards.

CRES conducts applied research, provides consultation to private industries and government agencies, and disseminates knowledge and best practice through technical conferences and topical seminars.